UNIVERSITÀ DI PARMA

UNIVERSITA’ DEGLI STUDI DI PARMA

DOTTORATO DI RICERCA IN FISICA

CICLO XXXII

Films of ε-Ga_2O_3: thermal stability, physical properties and defects

Coordinatore:
Chiar.mo Prof. Carretta Stefano

Tutore:
Chiar.mo Prof. Fornari Roberto

Dottorando:
Montedoro Vincenzo

Anni 2016/2019

Table of contents

List of abbreviations

a.u.	Arbitrary Units
AFM	Atomic Force Microscopy
ALD	Atomic Layer Deposition
ALE	Atomic Layer Epitaxy
APB	Anti-Phase Boundary
BF	Bright-Field
BFOM	Baliga Figure Of Merit
BL	Boundary Layer
CB	Conduction Band
CBM	Conduction Band Minimum
CL	Cathodoluminescence
CVD	Chemical Vapour Deposition
DFT	Density Functional Theory
DHM	Dynamic Hysteresis Measurement
DSC	Differential Scanning Calorimetry
EDC	Energy Distribution Curve
EPR	Electron Paramagnetic Resonance
FET	Field-Effect Transistor
FFT	Fast Fourier Transform
FL	Fermi Level
FWHM	Full-Width at Half-Maximum
GGA	Generalized Gradient Approximation
HRTEM	High-Resolution Transmission Electron Microscopy
HVPE	Halide Vapour Phase Epitaxy
MESFET	Metal-Semiconductor Field-Effect Transistor
MFC	Mass Flow Controller
MOCVD	Metalorganic Chemical Vapour Deposition
MOSFET	Metal-Oxide-Semiconductor Field-Effect Transistor

List of abbreviations

PCS	Photocurrent Spectroscopy
PDF	Pair Distribution Function
PID	Proportional-Integral-Derivative (power control system)
PLD	Pulsed Laser Deposition
RBS	Rutherford Back-Scattering
SAED	Selected Area Electron Diffraction
sccm	Standard Cubic Centimetres per Minute
SEM	Scanning Electron Microscopy
STEM	Scanning Transmission Electron Microscopy
TB	Twin Boundary
TEM	Transmission Electron Microscopy
TMA	Trimethylaluminium
TMG	Trimethylgallium
ToF-SIMS	Time of Flight-Secondary Ion Mass Spectroscopy
UV	Ultraviolet
VB	Valence Band
VBM	Valence Band Maximum
VPE	Vapour Phase Epitaxy
XRD	X-Ray Diffraction

Introduction

Oxide semiconductors are generally characterized by good thermal and chemical stability, they can be grown by various growth techniques and be doped to obtain the necessary conductivity for optoelectronic devices, power electronics and gas sensors, which makes them very popular and intensively studied. Gallium oxide, which belongs to this group of semiconductors, was first observed when the gallium element and its principal compounds were discovered at the end of 19th century[1]. Rapidly, the study and the interest about this material moved from a basic research to first simple applications, i.e. catalyst for chemical reaction[2–4], gas sensor in different environments[5–7], transparent conductive electrodes[8,9]. Over time the crystal growth technology improved significatively allowing to achieve both bulk[10,11] and epitaxial thin films[12–15] of high quality Ga_2O_3. Further technological developments, together with a controlled n-type doping[16–18] led to a wider range of applications[19–21]. The wide bandgap (4.6-4.9 eV[8,9,11,21–23]), makes it one of the most interesting materials for UV optoelectronics[20,21]. It simultaneously attracts the global attention for power electronics[24] due to its high critical breakdown field, estimated of about 8 MV/cm[19], which leads to a BFOM (Baliga Figure of Merit)[25] four times larger than the value observed in SiC and GaN compounds. Among the six known Ga_2O_3 polymorphs[26], the research was particularly focused on the β-phase that is the thermodynamically stable phase. Nevertheless, in the last years an increasing attention was turned to other polymorphs as well, especially towards the ε-Ga_2O_3, which results the second most stable phase[27]. It can be epitaxially grown at lower temperature with respect to β-polymorph[23] and exhibits a good matching with the most diffused commercial substrates. Although the ε-polymorph showed multiple interesting properties, it still remains rather unexplored compared with the most investigated β-phase.

These assumptions provided the principal motivations for the present Ph.D. work, that is focused on the epitaxial growth of high quality undoped and n-type doped films of ε-Ga_2O_3, carried out at IMEM-CNR institute, and on relevant characterization performed at the Department of Mathematical, Physical and Information Sciences (Physics Unit) of Parma University, and completed by national and international collaborations during the thesis period, in order to obtain new information on still unknown fundamental properties.

The first introductive chapter describes the state-of-the-art of the ε-polymorph, starting from the crystal and electronic structures, summarizing then the main physical properties and the epitaxial growth techniques, and concluding with a brief comparison with the stable β-phase.

Chapter 2 introduces the basic theory behind the epitaxial growth, focusing on the MOCVD method employed to obtain the samples analyzed in this thesis. Thus, chemical, physical and thermodynamic mechanisms are discussed. Finally, the experimental setup and the representative growth parameters are presented, along with the most significant results related to undoped and silicon doped films.

In chapter 3, the study about the thermal stability of ε-Ga_2O_3 layers, which resulted confirmed up to a temperature of ~700°, is reported. The phase transition was determined by using X-Ray diffraction on different specimens of the same sample, thermally treated at temperatures between 700°C-900°C. Additionally, TEM analysis and DSC characterization, performed by external collaborators, further confirmed the crystal phase conversion mechanism.

The purpose of the fourth chapter is to describe the electrical and optical properties of the ε-polymorph measured by different methods. Initially, after an introductive overview of the β-Ga_2O_3 electrical characteristics, the contact deposition techniques with the related parameters and the best electrode structures are reported. The contact development represents an important parallel field of study considering that electrical and photo-electrical measurements strongly depends on the contact performance. Then, the central part of the chapter is focused on the electrical investigation on Si and Sn doped samples, reporting the conditions and the configurations involved and presenting the obtained results. These data are discussed also taking into account the supplementary information provided by EPR, ToF-SIMS and RBS characterization, from external cooperating groups. The chapter ends with optical and photo-electrical analysis of undoped films which highlight a significant response to UV illumination, making the ε-Ga_2O_3 a promising candidate for UV solar-blind photodetector fabrication.

Chapter 5 deals with defect-related deep energy states within the energy gap. Initially, the presence of these deep levels was argued looking at the absorption tail as well as to photocurrent for illumination with photons below the energy bandgap. However, a specific investigation, later performed at Valladolid University by cathodoluminescence, provided more detailed information, which led to a schematic model of the deep level-related optical transitions. Finally, a conclusive chapter summarizes the whole topics and the results presented in this work.

Chapter 1 – Gallium Oxide (Ga_2O_3)

Sesquioxides are ionic compounds, belonging to semiconductor oxides, formed by three oxygen anions for each two cations of another element. Group-III sesquioxides (Al_2O_3, In_2O_3, Ga_2O_3, Ti_2O_3), in particular, significantly attract the attention of semiconductor research for their wide application in different fields. Among these materials, Ga_2O_3 is characterized by a wide-bandgap and a good optical transparency, that make it ideal for high-power electronics, solar-blind photodetectors and optoelectronics devices. Gallium oxide polymorphs and their crystal structure, were reported, for the first time, about seventy years ago[26] and from the fifties till now they were intensively studied. Fig. 1.1 reports the number of publications per year on Ga_2O_3 from the beginning and the exponential increase of last 20 years is clearly visible.

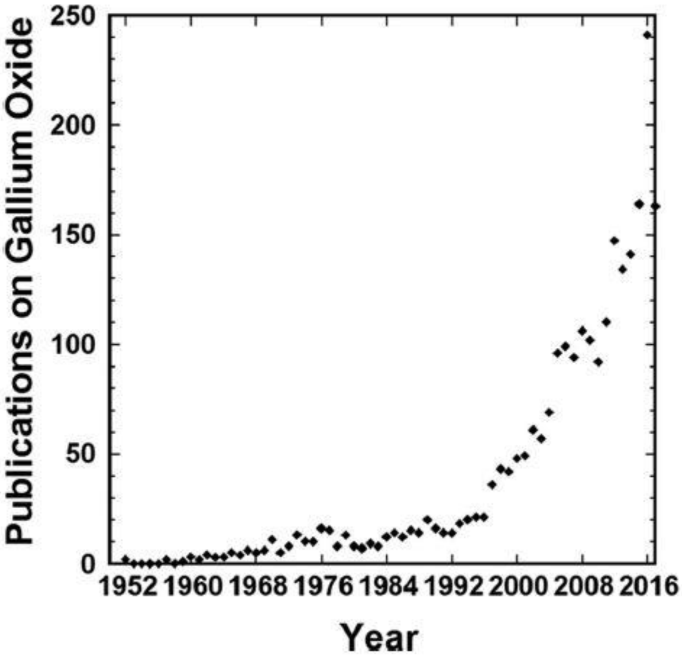

Fig. 1 Gallium oxide publication (~2500) since 1952. (Reproduced from Ref.28)

Nowadays, six confirmed gallium oxides polymorphs are known: corundum (α)[29], monoclinic (β) [30,31], defective spinel (γ)[32], orthorhombic (κ-ε)[33], bixbyite (δ)[34], probably a nanocrystalline form of orthorhombic phase (see Fig. 1.2). Their crystal structure consisting in close-packed stacking of oxygen atoms among which Ga atoms are disposed in octahedral and tetrahedral sites. Tab. 1.1 provides lattice parameters, space groups and some physical properties of each polytype.

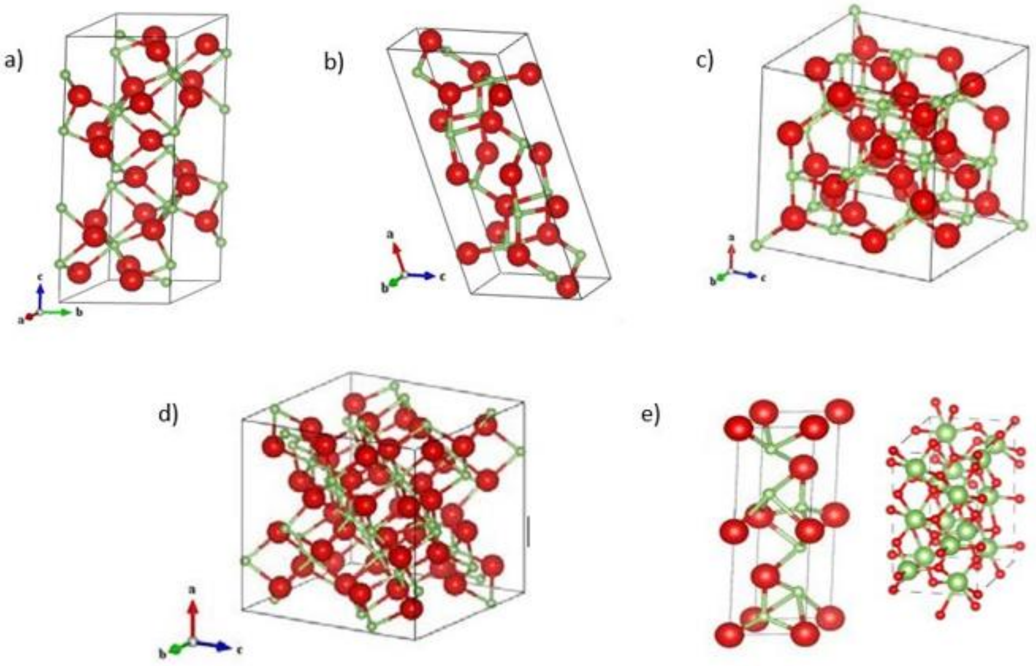

Fig. 1.2 Gallium oxide polymorphs crystal structure: a) α-phase rhombohedral/corundum structure [29], b) β-phase monoclinic/β-gallia structure [30,31], c) γ-phase cubic/defective spinel structure [32], d) δ-phase cubic/bixbyite structure [34], e) ε-phase hexagonal-orthorhombic structure [23,33]. Ga cations are represented by red bigger spheres and O anions by green smaller spheres (in orthorhombic structure, bottom-right figure, colors are inverted).

Polymorph	**Lattice parameters (Å)**	**Refractive index, n**	**Optical dielectric constant**	**Volume expansion at 1200K**	**Bulk modulus (300K, GPa)**	**Comment**	**References**
α	a, b=4.98–5.04, c=13.4–13.6	1.74–1.95	3.03–3.80	0.035	~185	Corundum, rhombohedral structure, space group $R\bar{3}c$, bandgap larger than the other polymorphs (~5.2eV)	(He *et al.*[35]; Stepanov *et al.*[31]; Yoshioka *et al.*[36])
β	a=12.12–12.34, b=3.03–3.04, c=5.80–5.87	1.68–1.89	2.82–3.57	0.024	~150	Monoclinic structure, space group $C2/m$	(He *et al.*[35] Stepanov *et al.*[31])
γ	a=8.24–8.30					Defective spinel, cubic structure, space group $Fd\bar{3}m$	(Stepanov *et al.*[31])
δ	a=9.4–10.0			0.04	160	Possibly bixbyite. Suggestedto be a nanocrystalline form of ε-Ga_2O_3, space group $Ia\bar{3}$	(Playford *et al.*[34]; Roy *et al.*[26])
κ, ε	a=5.06–5.12, b=8.69–8.79, c=9.3–9.4 a=2.90, c=9.25	1.6-2.0		0.028	160	Orthorhombic structure, space group $Pna21$ Hexagonal ($P6_3/mmc$) /Orthorhombic structure	(Kroll *et al.*[37]; Yoshioka *et al.*[36]) (Playford *et al.*[34]; Mezzadri *et al.*[38]; Cora *et al.*[33])

Tab 1.1 Lattice parameters, space groups and properties of Ga_2O_3 polymorphs.

Among these phases, β-Ga_2O_3 is the most studied one for different reasons. First of all, it results the only thermodynamically stable phase up to 1800°C, instead, in the other metastable polymorphs, crystal structure tends to reorganize into β-phase structure in the range temperature between 700°-900°C. Yoshioka *et al.*[36] reported calculated temperature dependence of the differences between Helmholtz free energy of the metastable phases and stable β-polymorph. Formation energies, at relatively low temperature, follow the sequent order: $\beta < \varepsilon < \alpha < \delta < \gamma$. Free energy difference between the β-phase and the ε-phase becomes smaller for increasing temperature, and vanishes at around 1600 K (Fig. 1.3). Another important point that justifies the interest on β-Ga_2O_3, concerns the possibility to grow single crystals of this material by melt and thus get cost-effective wafers, compared to other wide bandgap materials like GaN and SiC. However, it also presents disadvantages such as a strong optical and thermal anisotropy and cleavage predisposition in certain growth direction. For this reason, in the last few years, metastable polymorphs have also been taken into consideration, in particular those with higher crystallographic symmetry.

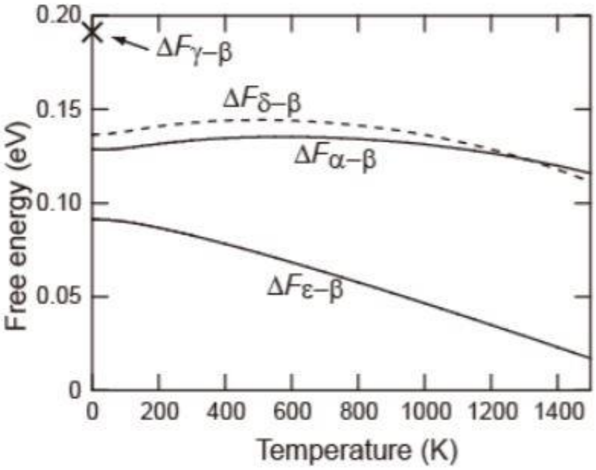

Fig. 1.3 Temperature dependence of Helmholtz free energy difference between metastable polymorphs and β-phase. (Reproduced from Ref.36).

Different growth methods have been developed for sesquioxides over the years and they can be summarized in three macro-families: melt growth, epitaxial growth and growth via synthesis or catalysis. Considering that crystallization from melt requires high-temperature, only β-Ga_2O_3 can be produced through Czochralski (CZ)[39], edge-defined film fed (EFG)[40,41] and floating-zone (FZ)[42] melt growth techniques. On the other hand, it is possible to obtain all polymorphs by epitaxy, under different conditions and on several substrates[43,44], or by synthesis[34] (see Fig. 1.4a,b,c). For example, Akazawa *et al.*[43] reported epitaxial growth of Ga_2O_3 phases, on Si(001) and on sapphire c- and a-planes, which are also strictly influenced by the temperature and by the precursors, while Sun *et al.*[44] reached multiple polymorphs by using HCl-enhanced deposition approach, with HCl as catalyst involved in different flow rates. Playford *et al.*[34], instead, presented results of gallium oxide polytypes obtained from synthesis and interconversion, starting from the thermal decomposition of $Ga(NO_3)_3 \cdot 9H_2O$. In both cases, epitaxial and by synthesis growth, phase formation depends strongly on the atmosphere, pressure and temperature.

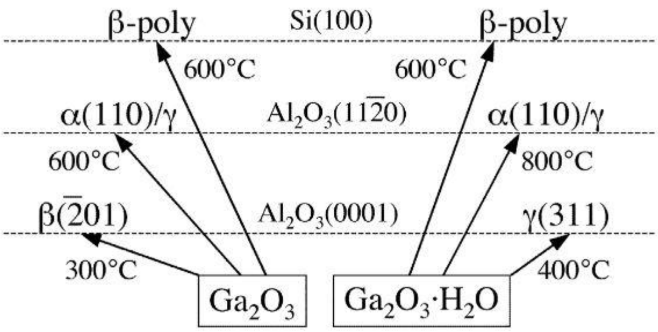

Fig. 1.4a Gallium oxide epitaxial growth on Si(100), Al_2O_3(0001) and Al_2O_3(11-20) substrates with H_2O ($Ga_2O_3 \cdot H_2O$) or O_2 (Ga_2O_3) as precursor. (Reproduced from Ref.43).

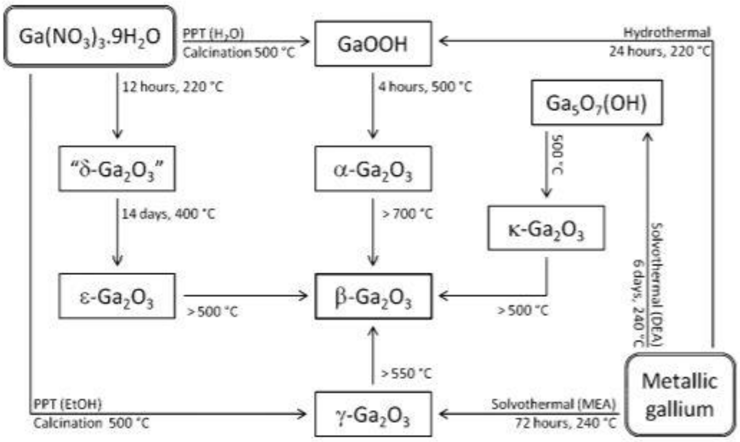

Fig. 1.4b Schematic representation of synthesis and interconversion of different Ga_2O_3 polymorphs. PPT=precipitate, DEA=diethanolamine, MEA=monoethanolamine. (Reproduced from Ref.34).

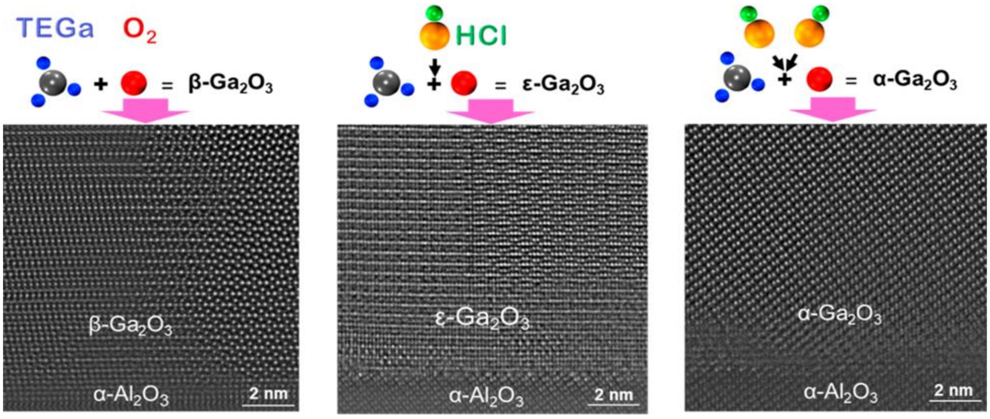

Fig. 1.4c Schematic representation of different Ga_2O_3-phases deposition in a HCl-enhanced mode. (Reproduced from Ref.44).

1.1 ε-Ga_2O_3 Polymorph – Crystal structure

In recent times, there was an increasing interest on ε-polymorph, among other phases, mostly thanks to its higher symmetry and favorable epitaxial growth conditions compared to the more popular β-phase. During these years ε-Ga_2O_3 crystal structure has been object of discussion by the researchers. The principal point to be clarified has been the real ε-phase space group, i.e. if it belongs to hexagonal or orthorhombic group. Mezzadri et *al.*[38] and Playford et *al.*[34], by using X-ray diffraction, experimentally pointed out a hexagonal structure with a close-packed array of oxygen ions, among which partially filled layers of octahedral and tetrahedral Ga sites are placed, compatible with $P6_3mc$ space group.

Playford et *al.*[34] achieved ε-phase samples, with β-contamination, by thermal decomposition of gallium nitrate and then annealing the product. A comparison of powder XRD pattern of obtained material with simulated orthorhombic[36] and "disordered" hexagonal ε-Fe_2O_3[45] was carried out in order to check the peak intensity and positions (see Fig. 1.5). Although the peak positions of both hexagonal and orthorhombic epsilon phase resulted similar and could be misinterpreted, the peak intensities of the hexagonal disordered variant seem to match sufficiently well the measured XRD pattern of ε-Ga_2O_3. After that, refined crystal parameters of hexagonal ε-polymorphs structure were found performing Rietveld and PDF analysis, also incorporating β-Ga_2O_3 as a secondary phase (Fig. 1.6a,b)

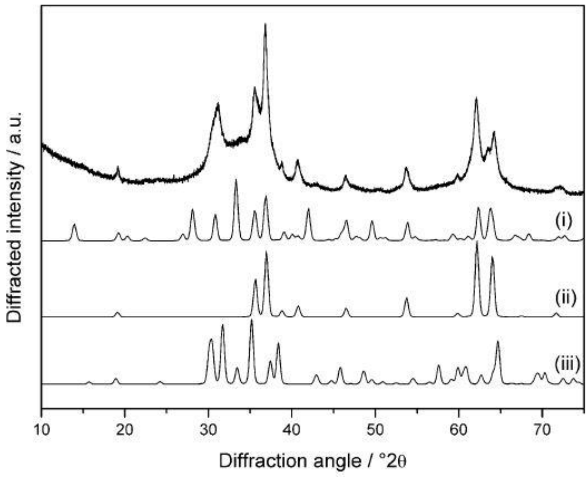

Fig. 1.5 ε-Ga_2O_3 measured XRD pattern (upper curve) compared with simulated i) orthorhombic ε-Fe_2O_3, ii) disordered" hexagonal ε-Fe_2O_3, iii) β-Ga_2O_3. (Reproduced from Ref. 34)

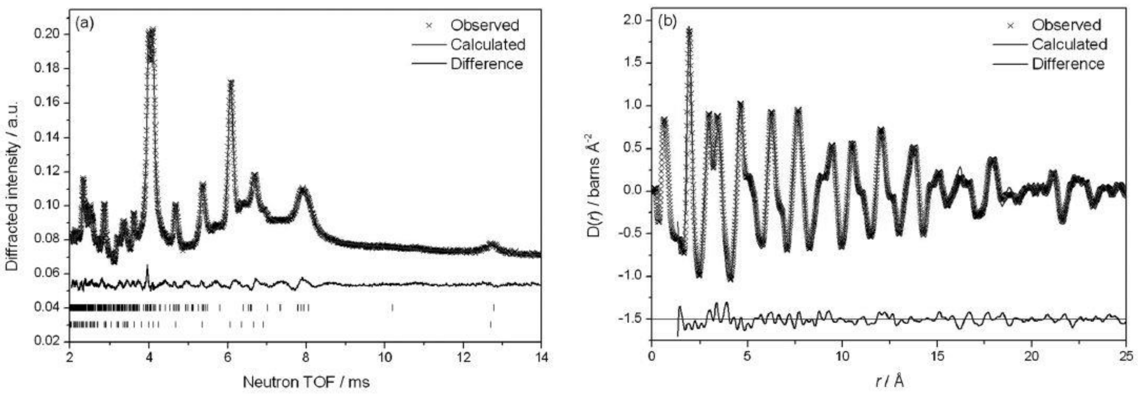

Fig. 1.6 a) Reitveld and b) PDF fit of ε-Ga_2O_3 . Two-phase fits were used in both cases with the hexagonal ε -Ga2O3 model (upper tick marks) and β -Ga2O3 (lower tick marks). (Reproduced from Ref.34)

Mezzadri et *al.*[38] investigated the structure the of ε-Ga_2O_3 films of different thickness, grown by MOCVD at relatively low temperature (600°C). From X-ray diffraction, well-defined and relatively intense peaks confirmed a good crystal quality. Two almost exactly superimposed hexagonal lattices were shown in *hki*0 plane (Fig. 1.7a). As shown, the Ga_2O_3 [10−10] and Al_2O_3 [11−20] directions are coincident and thus hexagonal lattices are rotated by 30° between them in the *ab* plane. Refined analysis show reflection conditions compatible with $P6_3mc$ space group, and also that the GA1 occupation of octahedral sites between two close-packed oxygen layers and GA2 and GA3 reciprocal occupation of octahedral and tetrahedral sites between the subsequent oxygen layers has an occupancy probability of 2/3, consistently with the Ga_2O_3 stoichiometry (Fig. 1.7b). Thus, XRD measurements on the ‘averaged’ structure together with several SEM images, showing hexagonal shape of the nucleation island, provided by different studies[46,47], contributed to spread the misleading opinion of a hexagonal lattice for the ε-phase.

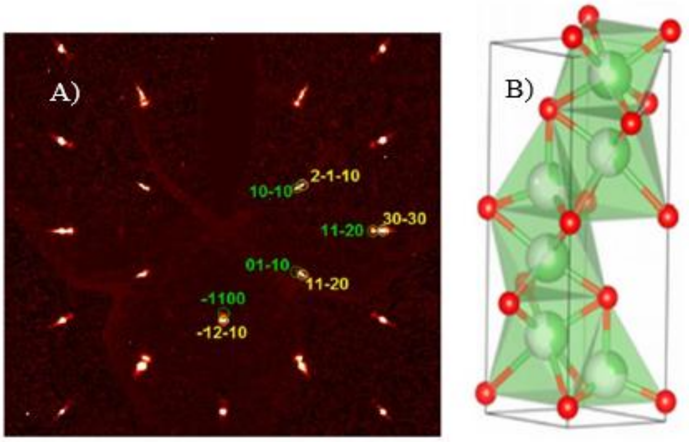

Fig. 1.7 A) Precession image of ε-Ga_2O_3 (green labels) on c-Al_2O_3 (yellow labels) obtained by single-crystal diffraction data, B) ε-Ga_2O_3 4H stacking sequence with red small spheres representing close-packed oxygen layers and green spheres in the octahedral and tetrahedral sites occupied by gallium ions. (Reproduced from Ref.38)

However, Yoshioka et *al.*[36] reported in 2007 the first results concerning the possibility that ε-gallium oxide belongs to the orthorhombic space group. They carried out first-principles calculations to find structural parameters of ε-phase, taking into account the experimental results of Matsuzaki et *al.*[48], that found a crystal structure similar to the κ-Al_2O_3 orthorhombic in their Sn-doped samples. Therefore, κ-Al_2O_3 structure was used as initial input and, with an error of 2% due to approximation, lattice parameters were obtained. Moreover theoretical results of interplanar spacings, powder XRD intensities and peak position of 28.1°, 30.7° and 33.4° agree with the experimental data of ε-Ga_2O_3 reported by Roy et *al.*[26] .

This set of literature data stimulated a more accurate investigation of ε-Ga_2O_3 crystallographic phase by Cora et *al.* [33], that finally could solve the ambiguity about the ε-Ga_2O_3 real structure. XRD and high-resolution Transmission Electron Microscopy (TEM) were carried out in order to investigate the averaged and microscopic structure. Initially single-crystal X-ray diffraction detected a hexagonal crystal structure. In fact, in *hk*0 projection, reconstructed precession image shows a pattern quite coincident with a hexagonal disordered *6mm* symmetry, also found with SAED investigation (Fig. 1.8a,b). However, it's interesting that in the same image other structures, formed by superimposition of three orthorhombic lattices related to nano-domains rotated by 120° around *hk*0 projection axis, are also visible.

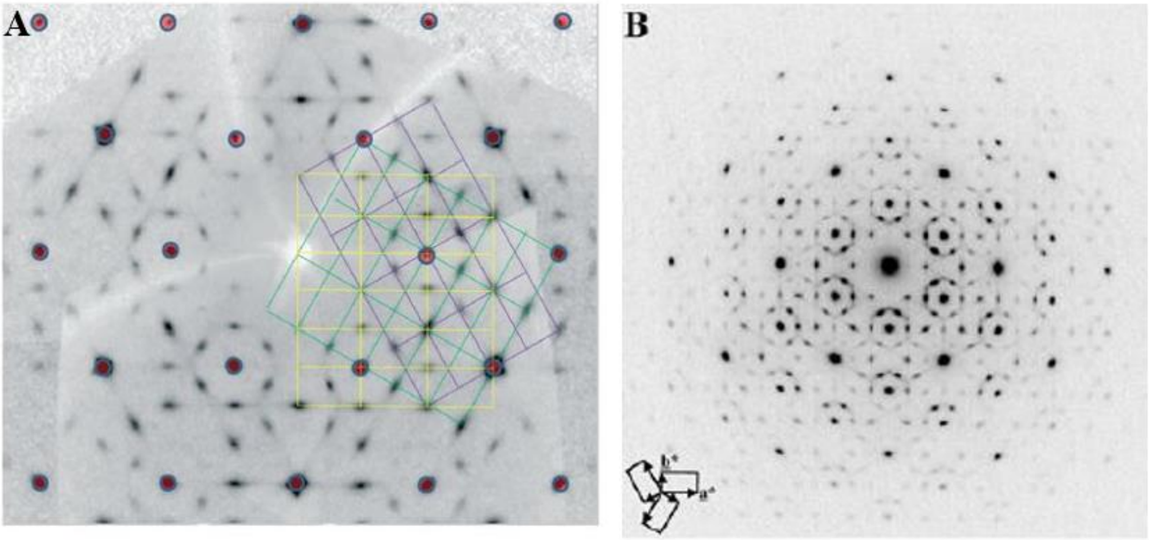

Fig. 1.8 a) κ-Ga_2O_3 reconstructed *hk*0 precession image. The three orthorhombic rotated lattices are shown. The red points are related to the hexagonal disordered lattice. b) Experimental SAED pattern showing hexagonal structure. (Reproduced from Ref.33)

These orthorhombic geometries were further studied by high-resolution TEM in order to obtain nanoscale information about local structure. TEM images showed a columnar growth of the films with column diameter of 2-10 nm, seen also in other studies[49], and an unexpected interface buffer layer between ε-phase film and α-Al_2O_3. Performing fast Fourier-transform (FFT) of 10–50 nm thin region, it was possible to identify this inter-region as epitaxial γ-Ga_2O_3 (see Fig. 1.9). The role of this interlayer is not yet clear, i.e. it could be possible that it acts as catalyst for the ε-polymorph growth, but more information is needed to confirm this hypothesis. Furthermore, confirming the XRD pattern previously shown, selected columnar-domains investigated by FFTs in HRTEM image exhibit an orthorhombic symmetry with these nano-domains, separated by (110)-orientated twin boundaries, which form a 120° angle between them (Fig. 1.10).

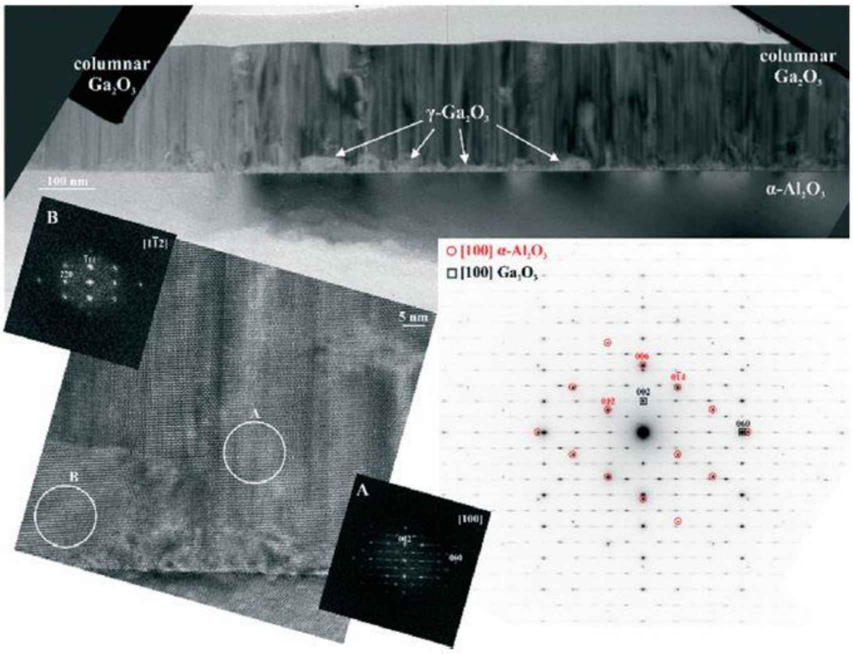

Fig. 1.9 Bright-Field (BF) image (top), selected-area electron diffraction (SAED) pattern (bottom right) and high-resolution transmission electron microscopy (HRTEM) (bottom left). BF is detected in vertical cross-section. HRTEM is presented with related indexed Fast Fourier Transforms (a e b). The b inset region with FFT shows the identified γ-phase and a inset exhibits the indexed orthorhombic unit cell. (Reproduced from Ref.33)

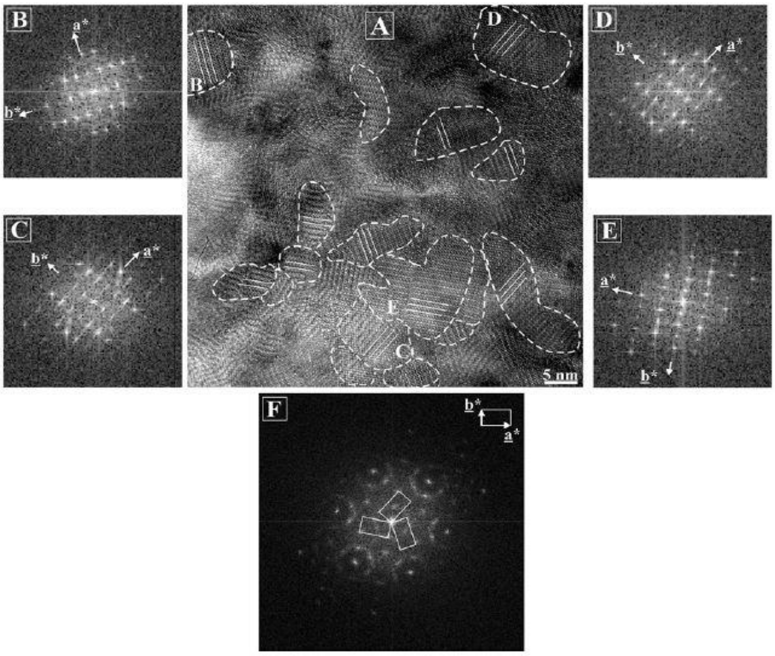

Fig. 1.10 a) High-resolution TEM image with (b-e) the corresponding Fast Fourier Transforms (FFTs). HRTEM is performed on the plan-view section of the film in [001] projection. In b-d images orthorhombic symmetry domains are shown, rotated to each other by 120°. In f bottom image, in the whole region a pseudo-hexagonal symmetry is shown. (Reproduced from Ref.33)

Considering XRD and TEM results it is possible to describe the orthorhombic crystal structure as formed by ordered Ga atoms disposed in repeated stacking of octahedral layers alternated with layers of octahedra and tetrahedra, parallel to (001), separated by a stacking of oxygen layers (4H ABAC, Fig. 1.11). Along [100] direction the edge-sharing octahedra forms zig-zag ribbons, as well as the corner-sharing tetrahedra. This ordered structure results very similar to κ-Al_2O_3. Unit cell parameters, extrapolated by SAED patterns, are reported in Table 1.2.

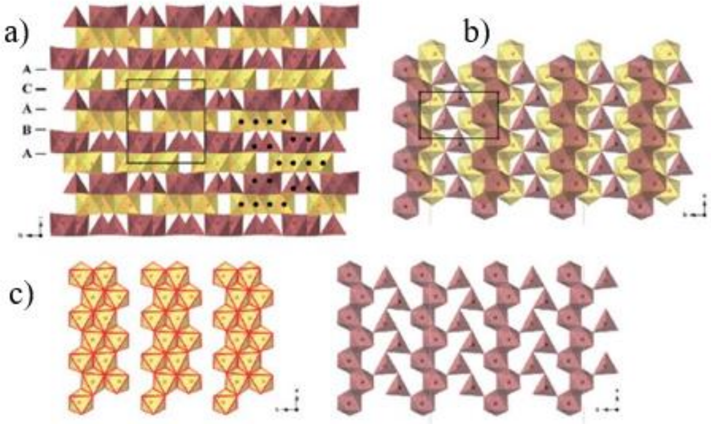

Fig. 1.11 a) [100] and b) [001] projections of κ-Ga_2O_3. c) The octahedra (in yellow) and tetrahedra and octahedra (in red) form ribbons parallel to [100] direction. (Reproduced from Ref.33)

Another interesting result is the presence of two different defect families, i.e. twin-boundaries and anti-phase boundaries which were both detected in [001] and [100] direction by projected high-resolution TEM images. The first are identified by the twinned positions of Ga atoms, while oxygen layers are preserved in ABAC close-packed arrangement, and the latter appear into the twinned domains and are justified by the shift of octahedral sites in the *b* direction (Fig. 1.12 a,b).

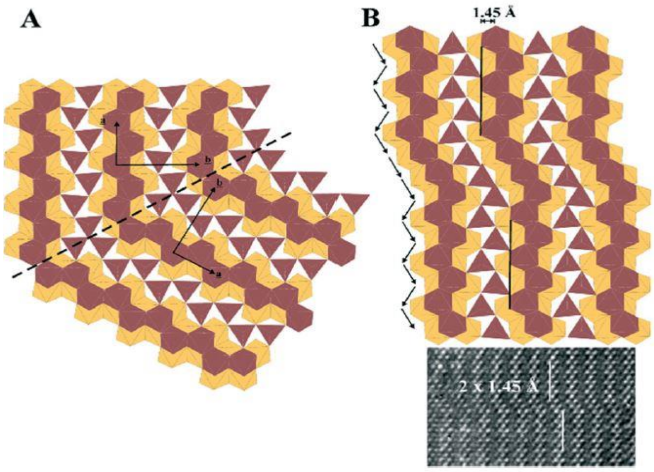

Fig. 1.12 Polyhedral structural model of a) rotated twin boundary on (110) plane and of b) anti-phase boundary into the domains. (Reproduced from Ref.33)

In conclusion, the real ε-Ga_2O_3 crystal structure is characterized by nanoscale ordered Ga atoms giving an orthorhombic symmetry. The ambiguity about the real structure was in fact generated by the resolution of the probing method, i.e. if the radiation coherence length applied to investigate samples results larger than domains size (typically x-ray), disordered hexagonal symmetry is found, while in case of smaller coherence length (electrons in a TEM), the orthorhombic ordered crystal structure is observed, proper of the κ-Ga_2O_3, which leads to $Pna2_1$ space group. In the next table (Tab. 1.2) lattice parameters and crystal data of the latest ε-phase crystal structure studies are reported.

Atom	**Wyckof Site**	**x**	**y**	**z**	**U_{iso} [Å^2]**	**S.O.F**
PLAYFORD[34]						
Rietveld		--	--	--	--	--
Ga1	2b	1/3	2/3	0.5598(6)	0.0044(2)	0.423(3)
Ga2	2b	2/3	1/3	0.6538(5)	0.0044(2)	0.399(2)
Ga3	2b	1/3	2/3	0.3705(4)	0.0044(2)	0.511(3)
O1	2a	0	0	0.0016(6)	0.0091(2)	1
O2	2b	1/3	2/3	0.7556(6)	0.0091(2)	1
Lattice Parameters	s.g. P63mc (n. 186); a=2.9036(2) Å, c=9.2554(9) Å, wRp=1.48%, measured density= 6.4299 g cm^{-3}, calculated density=6.0622 g cm^{-3}					
PDF		--	--	--	--	--
Ga1	2b	1/3	2/3	0.5622(2)	0.01382(3)	0.3701(7)
Ga2	2b	2/3	1/3	0.65568(9)	0.01382(3)	0.322(2)
Ga3	2b	1/3	2/3	0.36433(5)	0.01382(3)	0.641(2)
O1	2a	0	0	0.99915(7)	0.01433(3)	1
O2	2b	1/3	2/3	0.75599(8)	0.01433(3)	1
Lattice Parameters	s.g. $P6_3mc$ (n. 186): a=2.90726(5) Å, c=9.2559(3) Å, wRp=12.7%.					
MEZZADRI[38]						
GA1	2b	0.6667	0.333	0.4269(9)	0.0291(15)	0.6667
GA2	2b	0.6667	0.333	0.2167(11)	0.0291(15)	0.35(2)
GA3	2b	0.6667	0.333	0.6210(17)	0.0291(15)	0.318(18)
O1	2b	0.3333	0.667	0.323(4)	0.025(5)	1
O2	2a	0	0	0.558(3)	0.025(5)	1
Lattice Parameters	s.g. $P6_3mc$ (n. 186) a=2.9081(7) Å, c=9.262(3) Å Volume= 67.8(5) Å^3 calculated density= 6.106 g cm^{-3}					
YOSHIOKA[36]						
GA1	4a	0.1777	0.152	0.998		1
GA2	4a	0.8127	0.162	0.3087		1
GA3	4a	0.1911	0.150	0.5874		1
GA4	4a	0.6781	0.032	0.796		1
O1	4a	0.9705	0.325	0.4259		1
O2	4a	0.5228	0.488	0.4331		1
O3	4a	0.6514	0.002	0.2043		1
O4	4a	0.1535	0.159	0.1975		1
O5	4a	0.848	0.171	0.6705		1
O6	4a	0.5192	0.168	0.9383		1
Lattice Parameters	s.g. $Pna2_1$ (n. 33) a=5,120 Å, b=8,792 Å, c=9,410 Å, Volume= 423.6 Å^3, calculated density= 5.88 g cm-3					
CORA[33]						
GA1	4a	0.1838	0.340	0.0278(5)	1	0.002
GA2	4a	0.6754	0.530	0.0369(6)	1	0.0049(10)
GA3	4a	0.1891	0.653	0.2503(5)	1	0.0062(12)
GA4	4a	0.1742	0.653	-0.1607.6)	1	0.0103(14)
O1	4a	0.350	0.492	0.137(4)	1	0.005
O2	4a	-0.016	0.494	-0.093.4)	1	0.005
O3	4a	0.335	0.154	0.150(4)	1	0.005
O4	4a	0.847	0.670	0.169(4)	1	0.005
O5	4a	0.000	0.829	0.409(4)	1	0.005
O6	4a	0.508	0.666	-0.097.4)	1	0.005
Lattice Parameters	s.g. Pna21 (n. 33) ; a=5.0463(15) Å, b=8.7020(9) Å, c=9.2833(16) Å, V=407.66(15)Å^3 calculated density=6.108 g cm^{-3}					

Tab. 1.2 Lattice parameters and crystal data of the latest ε-phase crystal structure studies.

1.2 ε-Ga_2O_3 Polymorph – Electronic structure

Electronic structure of ε-Ga_2O_3 has been theoretically and experimentally investigated in the last years and the studies agree to identify this polymorph as a direct bandgap semiconductor. Kim et *al.*[50] proposed a theoretical approach that provides bandgap information and further electronic details using the conventional generalized gradient approximation (GGA) and hybrid functionals. In particular, first-principle calculations with the PBEsol GGA[51] and projector-augmented-wave method were carried out[52,53]. However, this method often underestimates the real bandgap values[35,54] and for this reason B3LYP hybrid functional were performed too[55]. Orthorhombic structure was used as initial calculation input. The reported bandgap values, obtained by these two different density functionals, resulted to be 2.32 eV for PBEsol and 4.62 for B3LYP model (Fig. 1.13 a,b). As anticipated and already seen in β-phase, the bandgap value obtained by PBEsol was much lower than the real one but using B3LYP functional bandgap value achieved can be compared to the experimental results. Despite an almost flat valence band, a maximum occurs at the Γ-point and, as shown in Fig. 1.13b also the conduction band minimum lies at the Γ-point, generating a direct bandgap.

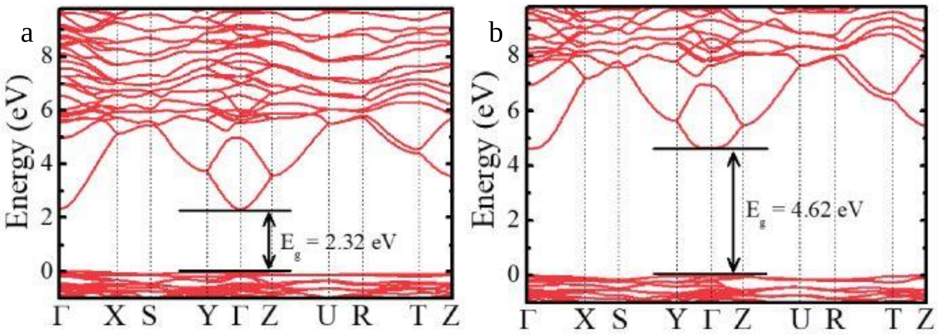

Fig. 1.13 Orthorhombic band structure of calculated by a) PBEsol functional and b) B3LYP hybrid functional. (Reproduced from Ref.50)

Experimental and theoretical studies were also carried out by Mulazzi et *al.*[56] performing ARPES and XPS measurements and GGA[51] and hybrid functional HSE simulation[57]. Calculated valence band top (Fig. 1.14a) is confirmed to be very flat and the whole band exhibits a width of 6.96 eV in GGA and 7.26 eV in HSE functional; moreover, as shown, it contains several theoretical bands located in the whole energy range. Calculation of plotted data near the top of the valence band shows a valence band maximum (VBM) at Γ-point (Fig. 1.15b), so that, considering a conduction band minimum (CBM) centered at the same point, a direct bandgap is observed and the extrapolated values result 2.32 and 4.26 by GGA and HSE, respectively. The HSE hybrid functional lower value compared to the value found by Kim et *al.*[50] is related to the fact that different DFT approaches can generate uncertainties of ± 0.5 eV as already seen in β-phase[58]. In Fig. 1. 14b, ARPES measurements exhibit a single broad band positioned 6 eV below the Fermi level, with a banding energy minimum at Γ-point. An increasing binding energy with wave vector indicates a negative high effective mass, which is achieved from energy distribution curve (EDC), fitting data at banding energy of the maximum, and results to be $m^* = -4.2\ m_0$. The linear extrapolation to zero of the EDC maximum peak allows to detect an apparent energy gap of $E_g = 4.41$ eV (see Fig. 1.15a), which is coherent with the value of 4.6 eV observed by photoconductivity measurements[21], considering a Fermi level pinned of 0.2 eV below CB.

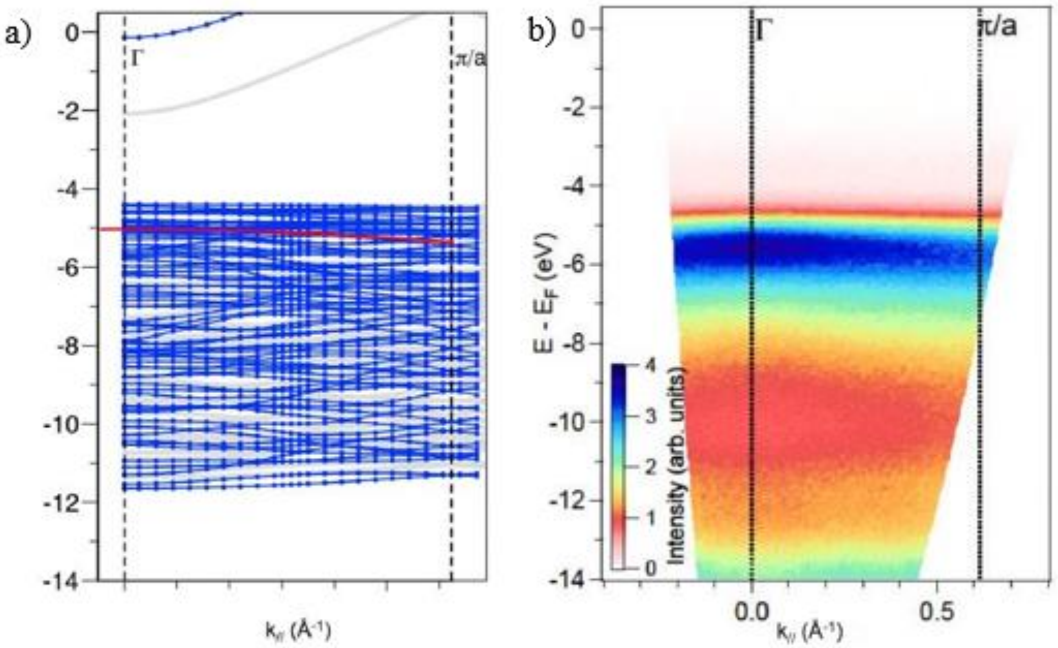

Fig. 1.14 a) Calculated electronic bands with GGA (gray lines) and HSE (blue dotted lines) functional and b) ARPES measurement. (Reproduced from Ref.56)

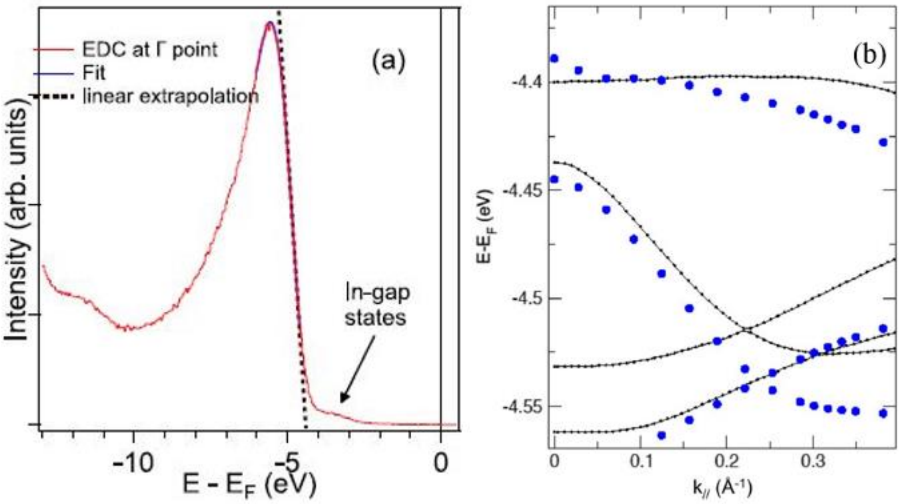

Fig. 1.15 a) EDC at Γ-point and b) calculation of the data near the top of the valence band. (Reproduced from Ref.56)

1.3 ε-Ga_2O_3 Polymorph – Polarization and Ferroelectricity

The orthorhombic *Pna*2_1 space group, as well as hexagonal *P*6_3*mc*, exhibits spontaneous polarization parallel to the *c*-axis, **P**=(0,0,P), because no inversion symmetry occurs in *c*-direction. Calculated and measured spontaneous polarization values were reported by different groups. Among them Maccioni & Fiorentini[27] obtained a value of 0.23 C/m^2, extrapolated by Berry-phase approach[59] with the difference between the calculated polarization in the ε-phase and in a centrosymmetric parent phase with a similar symmetry (e.g. *Pnma* supergroup, as parent phase, considering *Pna*2_1 space group) (see Fig. 1.16a). Furthermore, ε-Ga_2O_3 has a structure not switchable, thus polarization is expected to preserve its orientation following the polar axis within crystalline domain and this classify it as pyroelectric material. Calculated piezoelectric coefficient of e_{33}= 0.77 C/m^2 results coherent with typical polar semiconductor oxide coefficients. Kim et *al.*[50] investigated the polar structure also using Berry-phase method, splitting the found value into polarization quantum (Po), which depends only by the system structural data (Po= e**R**/V, where V and **R** are the unit cell volume and the lattice vector, respectively) and spontaneous polarization (Ps). By modular arithmetic analysis Ps results of 0.26 C/m^2 for κ-phase, and 0.24 C/m^2 for ε-phase were reported and compare well with the previous work. The polar behavior of non-centrosymmetric orthorhombic space group was also revealed by structural analysis, of Cora et *al.*[33], carried out on ‘out of plane’ distances between gallium atoms and oxygen layers, along the *c*-axis. A net dipole moment of 0.20×10^{-2} C/m^2 comes out, extracted from refined atomic coordinates and generated by a positive cationic resultant disposition along the positive *c*-axis direction (Fig. 1.17). These results appear coherent with the ferroelectric character of the ε-Ga$_2$O$_3$ recently reported by Mezzadri et *al.*[38], who used simple point-charge model to estimate an electrical polarization of 0.18×10^{-2} C/m^2. The difference between electrical polarization values reported in literature could be probably related to different calculation models and parameters applied. Dynamic hysteresis measurement (DHM) were performed to confirm the ferroelectric nature of this polymorph. Triangular pulses of 1KV amplitude were applied, under 1KHz frequency condition, and a relative dielectric constant of 7.17 and a resistivity of 1.74×10^{12} Ωcm were measured. Moreover, the electrical polarization loop was detected and reported after data elaboration. Fig. 1.16b shows the P vs E loop with a maximum value of 0.0092 µC/cm^2, from the depolarized state. The polarization characteristic shows that no saturation was reached, at least up to 50 kV/cm applied electric field. This limited loop could explain the impressive difference between calculated and measure electrical polarization. This unusual coexistence of semiconducting and ferroelectric properties is unexpected and requires further investigations in order to reach new technological applications.

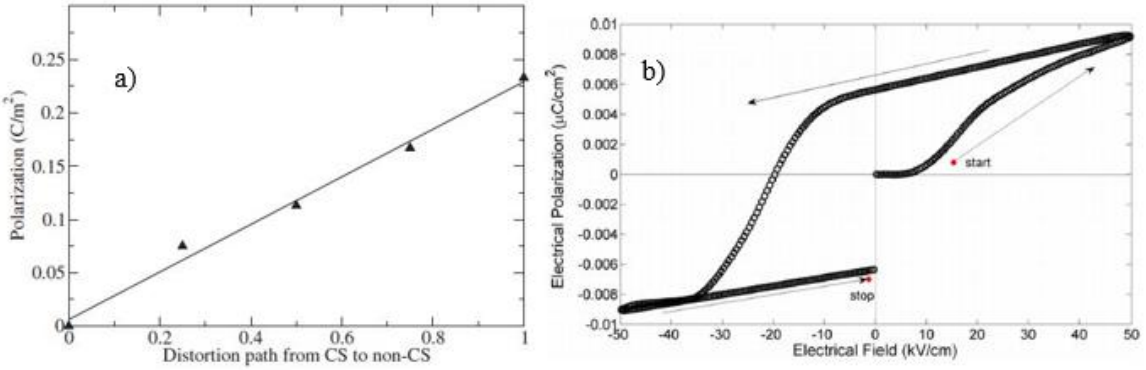

Fig. 1.16 a) Calculated polarization along a distortion path ranging from centrosymmetric similar phase to non-centrosymmetric ε-phase (Maccioni & Fiorentini[27]) and b) dynamic hysteresis measurements (DHM) of the electrical polarization (Reproduced from Ref.38).

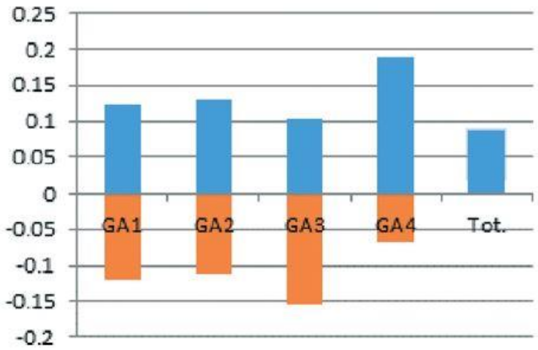

Fig. 1.17 Out-of-plane Gallium atoms distances (Å) from the adjacent oxygen layers along the *c* polar axis (Reproduced from Ref.33)

1.4 ε-Ga_2O_3 Polymorph – Optical properties

The optical bandgap of the ε-polymorph was reported for the first time by Oshima et *al.*[23]. The value was obtained carrying out transmittance measurements of a ε-film grown on AlN(0001)/SiC substrate by HVPE technique. After lapping and polishing proceedings of the SiC to avoid any possible absorption, an approximate bandgap of about 4.9 eV were extrapolated from the Tauc plot (see Fig. 1.18a). More recently Pavesi et *al.*[21] performed absorbance measurements on MOCVD films with different thicknesses, finding in all curves an onset of the band-band absorption that started at about 4.6 eV (Fig. 1.18b). The detected absorption coefficients compared well with the measured data from Oshima et *al.*[23]. These results demonstrate that the energy bandgap is similar to the β-phase bandgap, already intensively investigated[58,60]. Furthermore, photoconductivity spectroscopy (PCS) measurements were carried out on simple photo-resistors fabricated in planar metal-semiconductor geometry with bilayers electrodes of Au/Ti deposited by thermal evaporation.

In Fig. 1.18b, a comparison between optical absorption spectrum and photoconductivity spectrum of a thin film is shown and differences result evident between the two curves. The normalized PCS shows a slightly reduced onset at 4.2 eV with respect to estimated bandgap value of 4.6 eV and this could be related to the presence of energy levels into the gap due to different native defects, as already seen in β-polymorph[61,62]. In absorption spectra a longer tail is visible, up to 2 eV, which may be connected to additional light absorption due to defects at the interface between the substrate and the film.

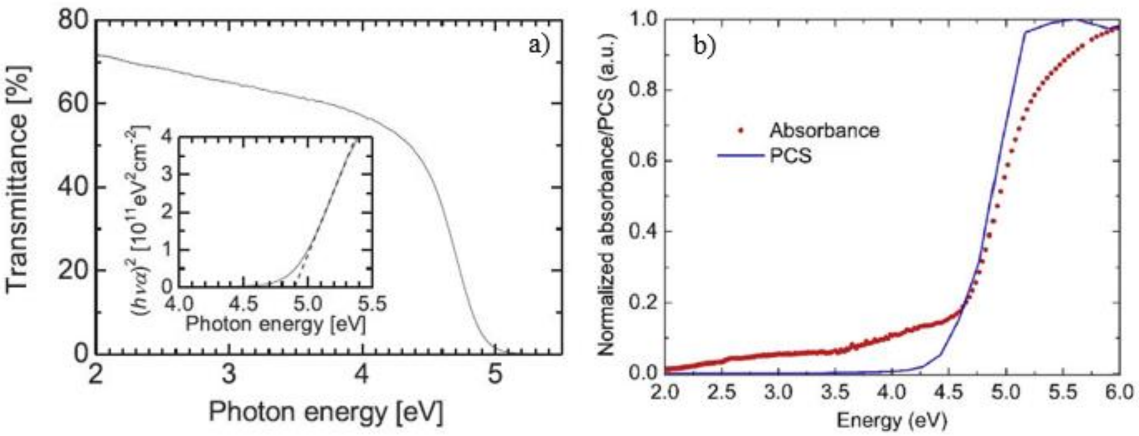

Fig. 1.18 a) ε-Ga_2O_3 transmittance spectrum. The inset shows the Tauc plot $(h\nu\alpha)^2$ vs $h\nu$ and b) PCS and absorbance spectra. (Reproduced from Ref.23)

The ε-Ga_2O_3 Raman spectrum were reported by Kracht et *al.*[49] in a comparison with other phases Raman spectra. As published in previous works[63–65] α-, β-, and γ-Ga_2O_3 Raman spectra differ in mode number as well as in respective mode frequencies and this is also expected for the ε-phase. Transparent thin films grown by plasma-assisted MBE on sapphire were measured. Although the substrate Raman features are very intense and dominate the signal, different additional weak peaks are observable and they are indicated with arrows in Fig. 1.19. Eight signals are detected, at 189, 211, 233, 481, 545, 616, 680, and 715 cm^{-1}, that have no match with other polymorph spectra and by exclusion are assigned to ε-Ga_2O_3. Theoretical analysis was carried out starting from orthorhombic $Pna2_1$ space group and 12 Raman-active modes related to phonons in the Brillouin zone center, with representations $3A_1+3A_2+3B_1+3B_2$, were achieved. Analyzing the hexagonal $P6_3mc$ crystal structure, 6 Raman-active modes were detected with representations $2A_1+2E_1+2E_2$. Considering that the number of observed signals result larger than six (i.e. the number of active modes of the hexagonal structure), thus it can be concluded that the observed modes derive from the predicted orthorhombic ε-phase structure.

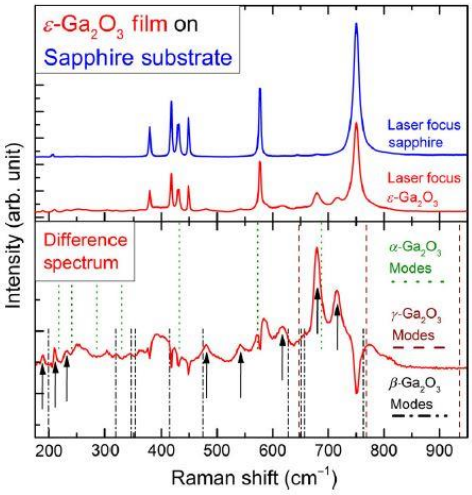

Fig. 1.19 Raman spectrum of ε-Ga_2O_3 compared to other phases (Reproduced from Ref.49).

1.5 ε-Ga_2O_3 Polymorph – Epitaxial growth techniques

As anticipated, ε-Ga_2O_3 is widely demonstrated, experimentally[33] and theoretically[36], to belong to the orthorhombic space group, despite several previous works that reported a hexagonal crystal structure for ε-Ga_2O_3. We already discussed how such misunderstanding originated from the pseudo-hexagonal arrangement of the orthorhombic domains that X-ray diffraction was not able to resolve. Among all gallium oxide polymorphs, the ε-phase, as well as the hexagonal α-phase, is characterized by different properties, such as higher crystallographic symmetry, better substrate matching to sapphire, isotropic physical properties and thermal stability at relative low temperature that makes it worth of attention. Nowadays this polymorph is successfully grown by several techniques on different substrates. Epitaxial ε-phase growth was firstly obtained by Oshima et *al.*[23] performing Halide Vapor Phase Epitaxy (HVPE) on different substrates, though this method has already been applied to achieve α- and β-phase by Oshima et *al.*[66] and Murakami et *al.*[67]. Three different substrate were tested, i.e. GaN(0001), AlN(0001) and β-Ga_2O_3(-201) and gallium chloride and pure O_2 were used as precursor gases in a horizontal reactor at 550°. SEM analysis shows that quite smooth surfaces were obtained, with an estimated 20µm/h growth rate, although some three-dimensional grains were visible with an increasing size with the growth time (Fig. 1.20-1). Furthermore, XRD investigations were carried out and spectra comparison shows only crystalline ε-phase (0001) diffraction peaks, in addition to substrate patterns (Fig. 1.20-2). The epitaxial relationship between ε-Ga_2O_3 and GaN, AlN and β-substrate were determined from the figures and it was revealed that the templates were similar for GaN and AlN, i.e. ε-Ga_2O_3(0001)||GaN(0001), ε-Ga_2O_3[10-10]||GaN[10-10] and ε-Ga_2O_3(0001)||AlN(0001), ε-Ga_2O_3[10-10]||AlN[10-10], instead a different epitaxial relationship were found with β-Ga_2O_3: ε-Ga_2O_3(0001)|| β-Ga_2O_3 (-201), ε-Ga_2O_3[10-10]|| β-Ga_2O_3 [102]. The related lattice mismatches resulted to be 8.8%, 6.6% and 1.1% with GaN(0001), AlN(0001) and β-Ga_2O_3(-201), respectively. The XRC profiles show the FWHMs of ε-Ga_2O_3 *0004* and *10-10* diffraction peaks, measured in different geometries, on the three substrates (see Fig. 1.20-3) and, while the peaks related to the growth on GaN and AlN have the same FWHM, those generated from the growth on β-polymorph result more crystalline. The authors conclude that, in HVPE, the space group relationship between film and substrate is essential to reach the best growth, thus *c*-plane GaN and AlN substrate result very suitable to deposit ε-Ga_2O_3, which can also be grown on β-phase at certain low temperatures.

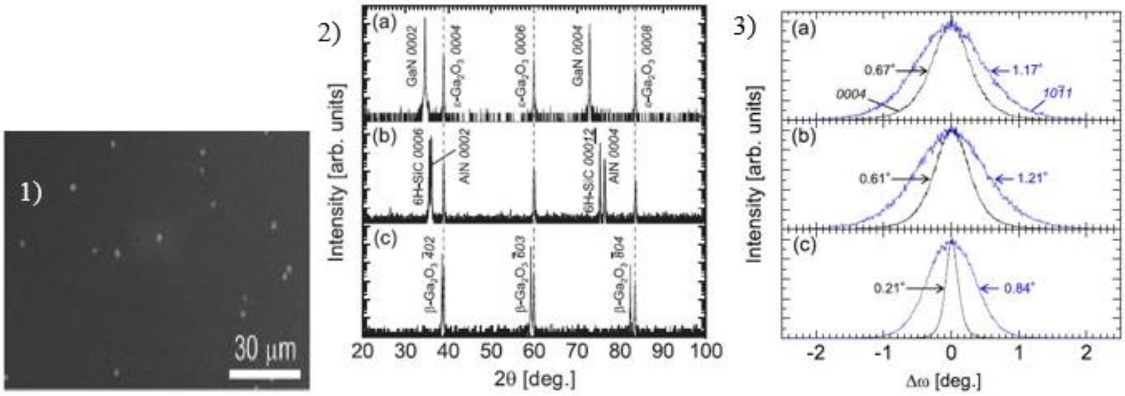

Fig. 1.20 1) SEM image in top view of ε-film, 2) XRD scan profile of epitaxial ε-phase on different substrates and 3) XRC data of ε-Ga_2O_3 *0004* (black) and *10-10* (blue) diffractions related to layers grown on three different substrates: (a) GaN(0001), (b) AlN(0001), (c) β-Ga_2O_3. (Reproduced from Ref.23)

Another very popular epitaxial growth technique for gallium oxide is the metal organic chemical vapor deposition (MOCVD). This method was utilized by different groups to obtain epitaxial ε-Ga_2O_3[44,46,47,68,69]. Among them, Boschi et *al*.[46] were the first to achieve ε-phase on different substrates from MOCVD. Ultrapure water and trimethylgallium (TMG) were used as precursor gases and were flown into the growth chamber, with H_2 as carrier gas, through two separate lines imposing a water-excess condition. Three deposition temperatures, i.e. 550°C, 650°C and 715°C were studied on the sapphire substrates (α-Al_2O_3) in order to understand the importance of the temperature in MOCVD growth. From X-ray polar map a lattice-mismatch of 4.8% were detected for the epitaxial ε-phase on (0001) sapphire[38]. At the lowest temperature (550°C) no crystalline film appeared and XRD profile exhibits only sapphire diffraction peaks, while the highest temperature (715°C) deposition shows very weak and broad reflections corresponding to β-phase (-201) of poor crystalline quality. However, the most interesting result were found at 650°C, whose XRD pattern has reflections corresponding ε-Ga_2O_3 (0001) diffraction planes (see Fig. 1.21a). Following this result, the same conditions were used also for other substrates in order to obtain more information on ε-polymorph deposition. XRD and SEM investigations confirmed a very good matching with GaN substrate, also (111) 3C-SiC shows acceptable compatibility. In the case of (001) 3C-SiC a mixture structure comes out, with β-Ga_2O_3 as secondary phase (see Fig. 1.21b). In conclusion, Boschi et *al*.[46] suggested that the phase obtained by MOCVD, mainly depends on the deposition temperature, but probably also precursors choice, growth rate and reactor pressure play an active role in the final result.

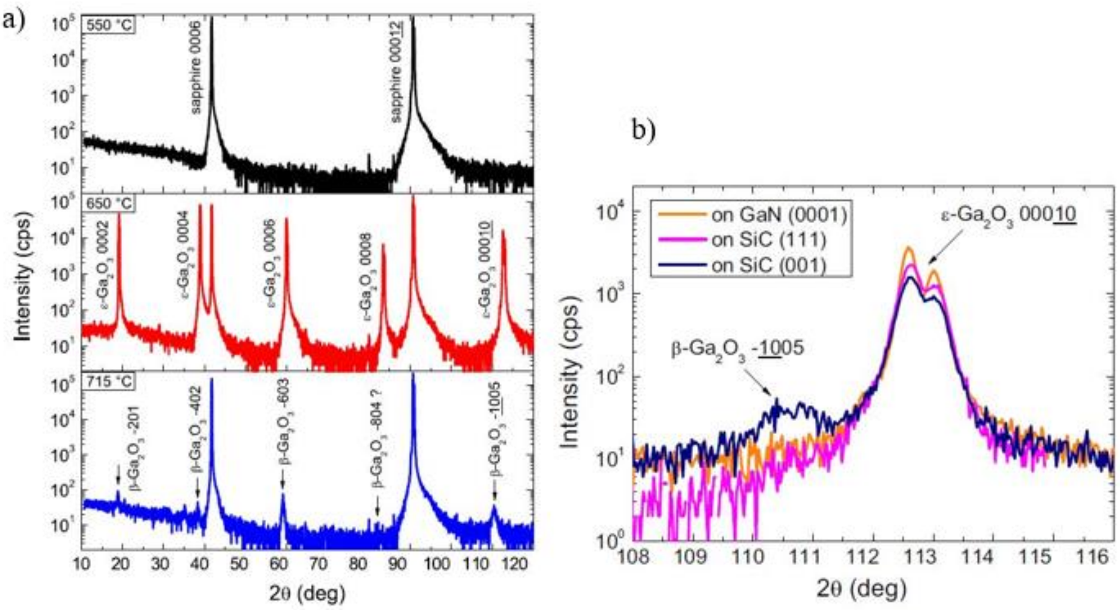

Fig. 1.21 a) XRD patterns of ε-Ga_2O_3 grown on α-Al_2O_3 at: 550°C, 650°C and 715°C, and XRD patterns on different substrates. (Reproduced from Ref.46)

However, the phase formation in MOCVD growth technique and its dependence on different parameters is still matter of investigations, and a general, unambiguous explanation has not yet been provided. Xia et *al.*[68] performed MOCVD on 6H-SiC substrate, selected for its good thermal and electrical conductivity and for its small a-axis lattice mismatch with ε-phase (3.3%). The ε-Ga_2O_3 films were grown at 500°C using triethylgallium (TEGa) and high-purity O_2 as reactants and Ar as carrier gas. The VI/III partial pressure ratio was imposed in oxygen excess and the chamber pressure was set at 3500 Pa. The reactor pressure resulted to be very important in the phase formation for Xia et al., in fact the optimal range to grow the ε-polymorph was approximately 1000-5000 Pa while for growth pressure higher than 5000 Pa the β-phase forms. Furthermore, X-ray diffraction phi-scan investigations were carried out to study the epitaxial relationship and the measurements confirmed the in-plane and out-of-plane relationships to be ε-Ga_2O_3<11-20>||6H-SiC<11-20> and ε-Ga_2O_3(0001)||6H-SiC(0001), respectively. According to the authors, the reactor pressure and the substrate lattice are the main variables that define the kind of phase deposited.

In order to clarify the growth mechanism and Ga_2O_3 phase control, Zhuo et *al.*[69] reported results achieved by different investigations studying the crucial growth parameters. TEGa and high purity O_2 were used as precursors in a reactor with a fixed growth pressure of 9.1 Torr. The temperature was varied between 450°C and 570°C and the VI/III ratio was changed between 500 and 1500. Phase-pure polycrystalline β-Ga_2O_3 was obtained at 535°C with grain structures as detected by SEM. At 505°C growth temperature a mixture of β- and ε-phase were obtained and XRD measurements revealed a better crystal quality of the ε-0006 which have a FWHM three times narrower than β-polymorph. While no diffraction peak was observed on the 480°C sample. In Fig. 1.22a,b the XRD patterns and the phase diagram of the grown thin films as function of the growth temperature and the VI/III ratio are shown.

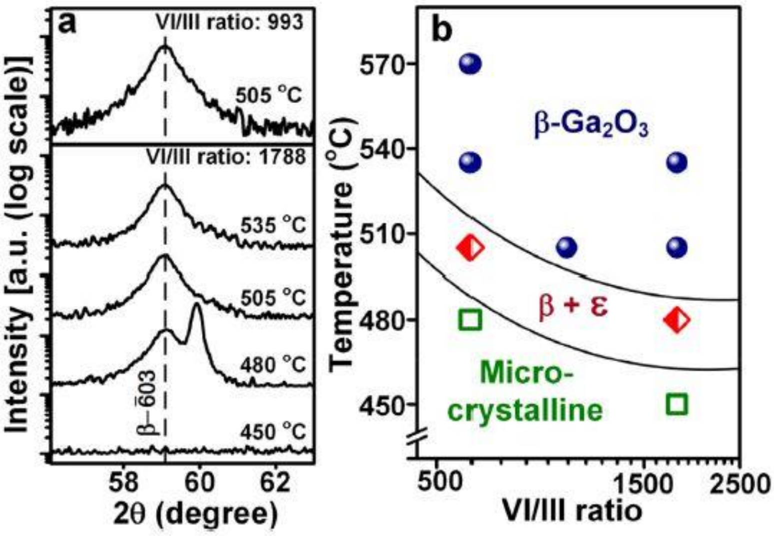

Fig. 1.22 a) XRD data of films grown at different temperatures and VI/III ratios and b) Ga_2O_3 phase diagram fixing TEGa flow rate at 67μmol/min. (Reproduced from Ref.69)

The phase formation and evolution were also investigated as a function of the film thicknesses and the growth rate. The results showed that with their growth conditions the nucleation of β-phase was inevitable. However, ε-Ga_2O_3 comes out more strongly in thicker film and at low growth rate (1 nm/min), which implies that ε is energetically favorable during the first stage of growth (see Fig. 1.23). Thus hypothetically, pure ε-phase can be grown if β-Ga_2O_3 is completely covered after the initial growth stage.

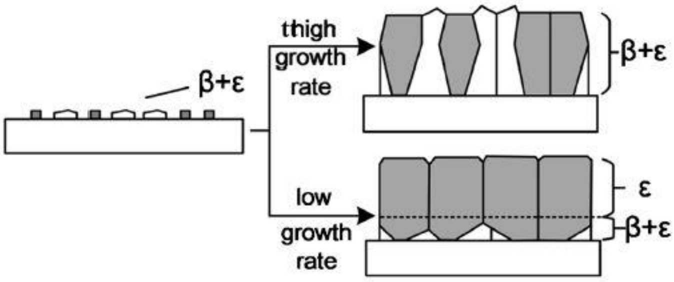

Fig. 1.23 Structural evolution model in function of the growth rate. (Reproduced from Ref.69)

Recently, epitaxial ε-Ga_2O_3 was obtained by MOCVD and MBE method also through catalysts or intermediaries application which promote formation of certain phases[44,49]. Sun et *al.*[44] successfully grew three different Ga_2O_3 phases changing only the flow rates of HCl gas introduced in the MOCVD reactor with fixed precursors (TEGa and O_2) flows. The growths were carried out on sapphire substrates at 600°C and 45 Torr for 1h, alternating five HCl flows from 0 to 60 sccm. XRD measurements (Fig. 1.24) show that, without or with 5 sccm HCl flow, only pure β-phase was obtained. For a HCl flow of 10 sccm a mixture of β- and ε-phase arises and the growth rate increases with the flow. Increasing the flow rate to 30 sccm phase-pure ε-Ga_2O_3 forms, while with 60 sccm a mixture of ε- and α-phase coexists and the latter results the dominant polymorph and the one with highest crystallinity. SIMS investigation exhibits a constant Cl concentration for each HCl flow rate applied, meaning that HCl acts as a growth catalyst and it is not incorporated into the film, but desorbs during the growth. Furthermore, DFT calculations confirmed this hypothesis and allowed to find the relative energies. The results well compare with previous studies[36] which reported a phase formation energy following the order $\beta < \varepsilon < \alpha$. However, in hydrogenated condition the ε-phase relative energy decreased indicating ε-Ga_2O_3 may be more favorable. Thus, the decreasing difference in free energy between the phases, for increasing HCl rate, leads to metastable phases formation.

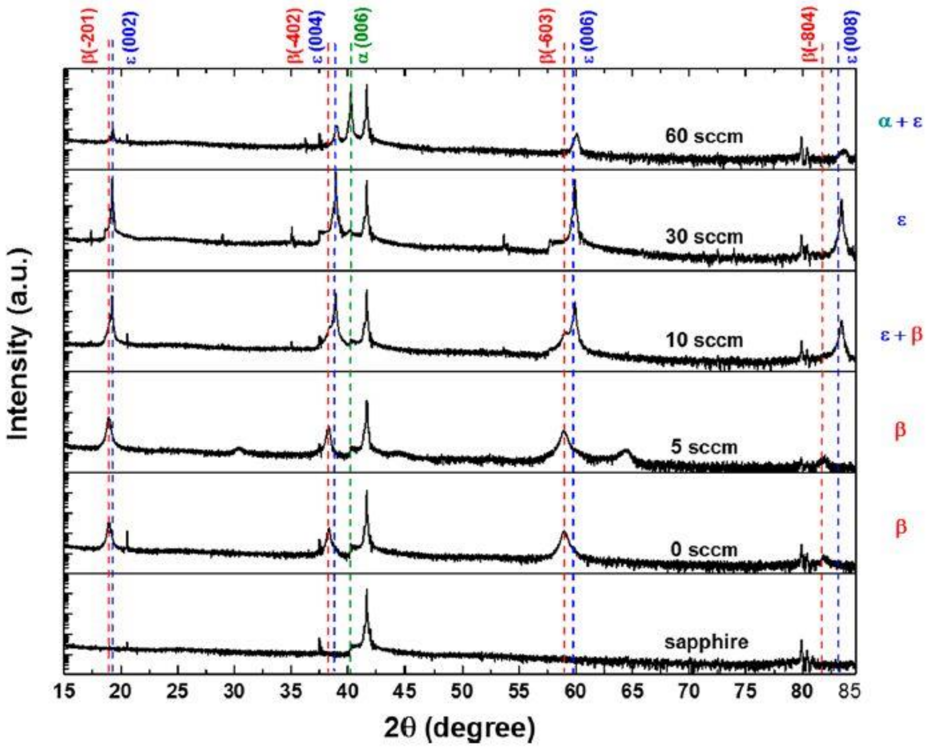

Fig. 1.24 X-ray diffraction patterns of Ga_2O_3-phases formed under different HCl flow rates. (Reproduced from Ref.44)

Kracht et *al.*[49] reported tin-assisted synthesis of ε-Ga_2O_3 by plasma-assisted MBE growth. This technique allows very controlled growth and heterostructures with sharp interfaces, however the growth rate usually results very low. In this case, the presence of thin allowed for an expansion of the growth window to metal-rich condition and considerably increased the growth rate. Furthermore, the reactor temperature was set at 700°C and three series of films were grown under different beam equivalent pressures (BEP) of tin. Depending on the flux, the presence of tin on the surface can promote the ε-phase formation, i.e. only the medium BEP$_{Sn}$ of 10^{-11} mbar produces phase-pure ε-polymorph, while higher flux promotes amorphous film and lower flux generates a mixture-phase (Fig. 1.25a). Thus, two effects are promoted from the tin-assisted epitaxy: the growth rate increases thanks to tin-oxide intermediary that stabilizing the growth on the surface acting as a further oxygen reservoirs, (see Fig. 1.25b), and limiting the volatile suboxides desorption, and, as second point, it allows the formation of orthorhombic ε-Ga_2O_3 when the tin concentration exceeds. The latter effect can be explained taking into account that in the orthorhombic ε-phase the tetrahedral to octahedral ratio results <1 and tin ions of rutile SnO_2 crystal show an octahedral disposition with the oxygens, therefore, tin addition to gallium oxide may promote the octahedral coordination favoring the ε-polymorph formation.

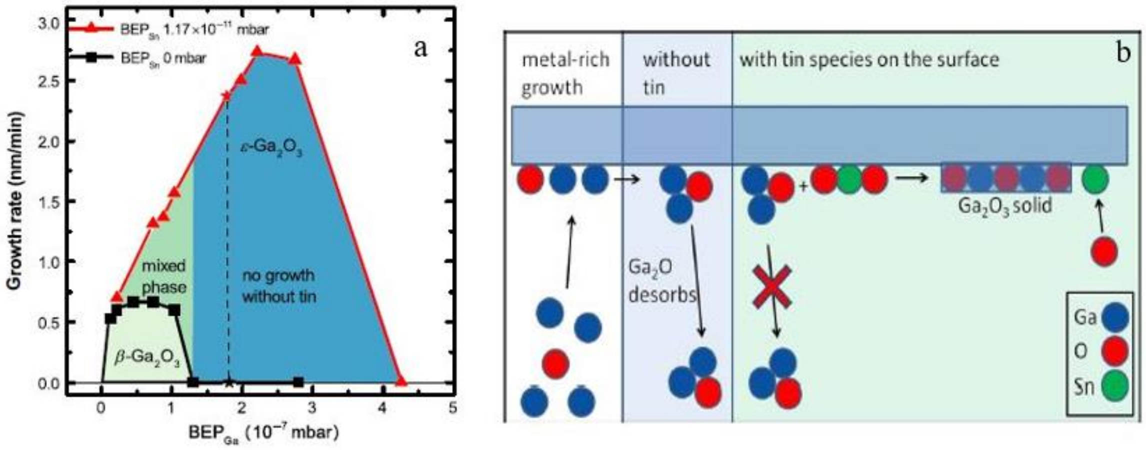

Fig. 1.25 a) Compared growth rates in MBE system of samples grown without and with tin and b) tin-assisted growth model (Reproduced from Ref.49)

It would thus appear that there is no unique way to deposit epitaxial phase-pure ε-Ga_2O_3. Actually, the growth parameters windows changes with the epitaxial method and with the ambient, giving rise to a complex interplay. Nevertheless, the ε-Ga_2O_3 phase has been achieved by different groups and related growth parameters are summarized in (Tab. 1.2).

Method	Substrate	Precursors	Temperature	Pressure	Phase
HVPE (Oshima *et al.*[23])	GaN(0001), AlN(0001) and β-Ga_2O_3(-201)	$GaCl_3$ and O_2	550°C	N.R.	ε-phase
MOCVD-ALD (Boschi *et al.*[46])	Sapphire(0001), 3C-SiC(111), 3C-SiC(001)	TMGa and H_2O	650°C(MOCVD) 550°C(ALD)	100 mbar (75 Torr)	ε-phase
MOCVD (Sun et al.[44])	Sapphire(0001)	TEGa and O_2	600°C	45 Torr	β, ε+β, ε, ε+α
MOCVD (Xia *et al.*[68])	6H-SiC	TEGa and O_2	500°C	3500 Pa (26 Torr)	ε, ε+β, β
MOCVD (Zhuo *et al.*[69])	Sapphire(0001)	TEGa and O_2	450°C-570°C	9.1 Torr	ε+β, β
HVPE (Yao *et al.*[47])	Sapphire(0001)	GaCl (Ga metal + HCl), O_2, Ar carrier gas	650-850°C	500-700 Torr	ε, α
MBE (Kracht *et al.*[49])	Sapphire(0001)	O_2, Gallium and Tin provided by effusion cells	700°C	N.R.	ε, ε+β

Tab. 1.2 Epitaxial growth techniques and associated parameters employed to obtain Ga_2O_3 polymorphs.

1.6 β-Ga_2O_3 stable polymorph

Among Ga_2O_3 polymorphs, the β-phase is the most studied, as already anticipated, for its several properties such as thermal stability up to the melting point, the production rate of high quality bulk material and a large breakdown electric field, which makes it particularly interesting in various applications.

The β-Ga_2O_3 crystal structure was investigated and found to be monoclinic, in *C*2/*m* space group symmetry[70]. The related lattice parameters (a_0=5.80 Å, b_0=3.04 Å, c_0=12.23 Å, β=103°42') were firstly reported by Kohn *et al.*[71] The β-phase unit cell composition is characterized by two different gallium ions (GA1 and GA2) located in two crystallographic non-equivalent positions, with tetrahedral and octahedral coordinates, and three different oxygen ions (O1, O2 and O3), which leads to physical, optical and electrical anisotropy, confirmed theoretically and experimentally[34,42,58]. Yoshioka *et al.*[36] also achieved theoretical values of lattice parameters, space group and volume expansivity of different polymorphs, finding that the volume expansion follows this order: $\beta < \varepsilon < \alpha < \delta$. About the electronic structure, a large quantity of theoretical calculations performed with density functional theory (DFT) and hybrid functionals can be found in literature[17,35,72,73]. The latter results to be more accurate and compares better with experimental measurements. All these studies agree to localize the conduction band minimum (CBM) in Γ-point, while there have been more debates on the valence band maximum (VBM) position due to an almost flat band and very poor dispersion. However, most of the calculations about the bandgap assign the VBM at the M-point [17,35], thus identifying an indirect bandgap (4.66 eV[35], 4.83 eV[17]) (Fig. 1.26). Janowitz *et al.*[74] obtained electronic structure information carrying out angular resolved photoemission spectroscopy (ARPES) and finding a VBM near the M-point and an indirect bandgap of 4.85 eV, which agree very well with theory. Furthermore, β-Ga_2O_3 could be defined an “almost” direct bandgap[17] thanks to a small difference between direct and indirect bandgap[17,35] and more intense direct transitions than the indirect ones. An electron effective mass of 0.27-0.34 m_e was extrapolated[17,35,73], where m_e is the free electron mass, while the flatness of the valence band derives from O(*2p*) orbitals with small dispersion and very large effective mass and density of states for holes. About the effective mass, Ueda *et al.*[42] reported that the electrical anisotropy is due to the anisotropic effective mass.

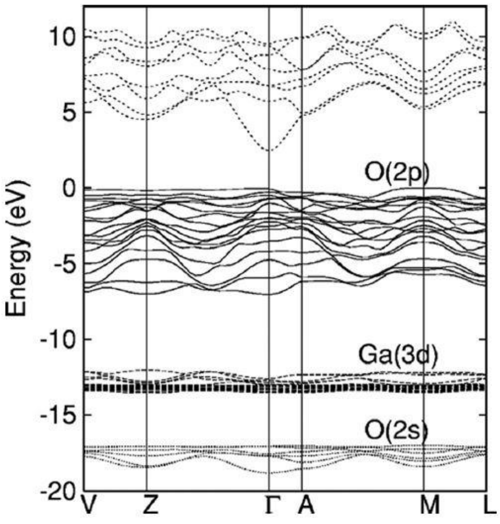

Fig. 1.26 β-Ga_2O_3 band structure with the Fermi level positioned in zero. (Reproduced from Ref.42)

Other notable anisotropic effects were found in thermal conductivity, i.e. in [010] direction the measured thermal conductivity (29 W/mK) results about 3 times higher than that in [100] direction[75–77], and in optical measurements, where is caused by the selection rule of the band-to-band transitions[72].

The β-Ga_2O_3 is a transparent semiconducting oxide (TSO), due to its wide bandgap which provides high transparency in the visible radiation range and is therefore colourless nature. A blueish colouration, generated by free-carrier absorption in near-infrared (NIR) and red range, is visible only in doped material[78]. As anticipated, optical anisotropy is caused by band-to-band transition rules, in fact Matsumoto *et al.*[22], as first, and Ueda *et al.*[42] and Ricci *et al.*[58] subsequently, reported the different absorption values achieved between the observed transitions when light polarized along *b* and *c* directions of (100) β-phase is used for the absorption experiments. They noticed that the bandgap in $E||b$ configuration was about 0.15-0.25 eV higher than the $E||c$ one, considering these direct transitions from the Γ^{2-} point and from the Γ^{1-} of the valence band to the Γ^{1+} position of the conduction band in $E||b$ and $E||c$, respectively (Fig. 1.27).

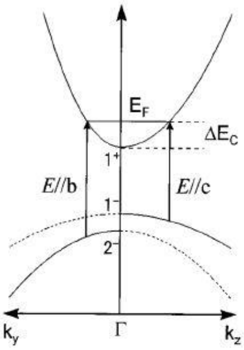

Fig. 1.27 β-Ga_2O_3 model of the band-to-band transitions in *k*-space. (Reproduced from Ref.42)

Optical properties were also measured by cathodoluminescence (CL) and photoluminescence (PL) in order to identify deep and shallow energy levels generated by native defects or contaminants. Most part of these studies propose a donor-acceptor-pair transition model with recombination of the electrons in the donor states and the holes in acceptor states that generates emissions in the visible radiation range (2.4-3.0 eV)[79–81]. In particular, additional doping tends to increase green luminescence at the expense of the blue emissions[82,83]. While, in the UV-range the emissions are attributed to radiative recombination between electrons and a self-trapped hole (STH)[80,81].

Onuma *et al.*[84] first investigated vibrational properties measuring lattice vibration modes from polarized Raman spectra obtained on doped and undoped β-Ga_2O_3. The Raman active modes Ag, related to the electric field vector direction for the incident light and Bg, that corresponding for the back scattered light, were observed separately following the polarization selection rules.

Thus, 30 normal modes are predicted by group theory for monoclinic β-phase, whereby 3 are acoustic and 27 are optical active modes, i.e. $\Gamma_{aco}=A_u+2B_u$, $\Gamma_{opt}=10A_g+5B_g+4A_u+8B_u$, with A_g and B_g Raman active and A_u and B_u infrared active (see Fig. 1.28).

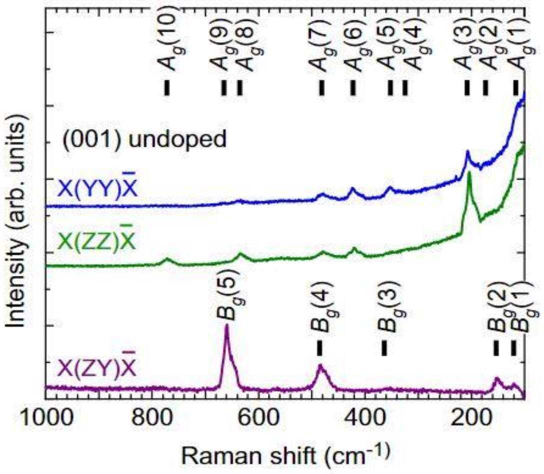

Fig. 1.28 Polarized Raman spectrum of undoped bulk β-Ga_2O_3. (Reproduced from Ref.84)

Some bulk growth methods, such as edge-defined and film-fed technique[10,40] allow to obtain (010) oriented β-Ga_2O_3 which can also be cut to get (-201) substrates. A large quantity of wafers is produced along this orientation, principally, for the critical electric field (E_c) of 8 MV/cm achieved[85,86]. In fact, high electric field is necessary to improve avalanche carrier multiplication, leading to breakdown, and it favors this material in power electronic device applications. The suitability of semiconductors in power applications is expressed in figure-of-merit (FOM) and different FOM exist. For example, Baliga’s figure of merit (BFOM is used to estimate dc conduction losses during transistor switching and in β-Ga_2O_3 results to be four times larger than in GaN and SiC. However, a remarkable disadvantage in using Ga_2O_3 for power devices is caused by the little thermal conductivity estimated in Huang’s high temperature figure of merit (HTFOM)[87] with a value which is several times lower compared to any other power semiconductor materials.

Chapter 2 - Growth method

The aim of this second chapter is the description of the basic theoretical features of the chemical vapor deposition (CVD) technique, principally focusing on metal-organic chemical vapor deposition (MOCVD), i.e. the epitaxial growth method used to obtain the studied samples. Furthermore, the experimental set up will be subsequently described and the best results will be presented. The deposition activities were carried out at CNR-IMEM institute, in collaboration with Dr. Matteo Bosi.

2.1 Epitaxial growth process

First epitaxial growth evidence of different crystal species dates back to the first half of the 19th century, however, the term "epitaxy" was introduced in the first half of 20th century, with the meaning of "arrangement on" [88]. In the last years, the epitaxial growth method reached a wide success in industrial application due to its potentials as low cost technique, elevate thickness control and high material mass-production for electronic and optical devices. Various epitaxial techniques were developed and could be classified in macro-groups: molecular beam epitaxy (MBE), solid phase epitaxy (SPE), liquid phase epitaxy (LPE) and vapor phase epitaxy (VPE). The latter is further divided into two categories depending on the species transportation to the substrate: physically (physical vapor deposition PVD) or chemically (chemical vapor deposition CVD). Nowadays, among all these methods, MBE and MOVPE (metal organic vapor phase epitaxy) are the most used to grow crystal structures of atomic level precision. In particular, MOVPE, compared to MBE, has some better features, in fact it can be carried out using a large number of chemical species to deposit different solid phases, with high degree of purity, at relatively low temperatures and atmospheric pressure and is characterized by a faster diffusion which implies a large growth rate.

The epitaxy process can be generally defined as a well-controlled phase transition between two crystalline phases in certain temperature and pressure conditions, which leads to a final crystalline solid deposition on an oriented substrate. In the case of iso-chemical composition system between the epilayers and the substrate, the growth mechanism is called homoepitaxy, while for different structural and chemical composition of epilayers and substrate the process is called heteroepitaxy. In both cases the deposition final product is a result of a complex nucleation and growth mechanism. The nucleation process is characterized by the formation of clusters of atoms or molecules, called nuclei, which agglomerate in certain position to create "islands" that, proceeding with the growth, may join up together forming chains and, finally, a continuous epilayer. The nucleation continues until there is no more space to generate nuclei between two clusters due to the nucleus "critical size", larger than the nucleation space. Merged clusters, arisen in a metastable supersaturated phase, lead to a complete crystallization.

The fundamental difference between epitaxy and the bulk crystal growth is related to the presence of the substrate which mainly influence the deposition introducing misfit, thermal stress and defects at the substrate-film interface. The interplay between the substrate, the precursors and the growth parameters can provide five different crystal growth modes: Frank-van der Merwe mode (FM-mode), step flow mode (SF-mode), layer plus island or Stranski-Krastanov mode (SK-mode), island or Volmer-Weber mode (VW-mode) and columnar growth mode (CG-mode) (see Fig. 2.1)[88]. The first two modes generate a layer-by-layer growth in which atoms and molecules are strongly bound to the substrate. In SK-mode an initial intermediate thin layer arises on the top of which subsequent atoms are arranged to form "islands". In the last two modes (VW-mode and CG-mode) atoms are more strongly bound to each other, thus columns or islands are nucleated on the substrate without any intermediate buffer layer. The crystallographic lattice mismatch and the chemical affinity between substrate and film are the main parameters that determine the growth mode.

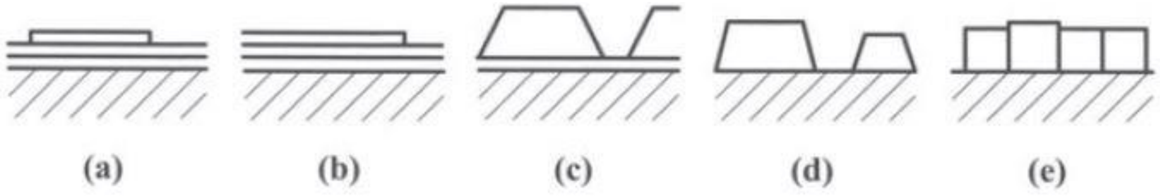

Fig. 2.1 Representation of most diffusing crystal growth modes on flat substrate surfaces: a) Frank-van der Merwe (FM) or layer-by-layer mode, b) step flow (SF) mode, c) Stranski-Krastanov (SK) or layer plus island mode, d) Volmer-Weber (VW) or island mode and e) columnar growth (CG) mode. (Reproduced from Ref. 88)

Chemical vapor deposition growth technique needs to be performed taking into consideration the chemical reactions which could be involved. The precursors reactions are defined and divided into several categories[89]:

- Pyrolisis, the most common reaction in a MOCVD system, in which gaseous compounds are deposited on the hot substrate surface after thermal dissociation.
- Reduction, where hydrogen usually is used as reducing agent.
- Exchange, that occurs when an element is replaced by another element.

- Disproportionation, that is characterized by the increasing and decreasing of the oxidation number of an element forming two new compounds.
- Coupled reaction, when two reactions occur simultaneously.

2.2 CVD method principles

CVD growth mechanism is based on the reaction between precursor species with molecular compounds and the substrate surface atoms. The precursor gas mixture is injected into the reactor chamber with a carrier gas, usually hydrogen or inert gas, and let to flow onto the heated substrate, where it may decompose and react to give a film. Sometimes an atmospheric pressure is set in the reaction chamber, however usually a low pressure is preferred in order to increase the growth rate and deposit a more uniform film. Other important factors in order to obtain thickness, stoichiometry and carrier concentration homogeneity are the choice of the reactants and the reactor geometries. Among several proposed reactors, one of the most used is the “cold-wall” reactor in horizontal design in which the substrate is maintained at higher temperature compared to the reactor walls, promoting a large temperature gradient and a mass transport to the hotter region (endothermic reaction). In the hot-wall reactor type, precursor decomposition may instead take place near the wall rather than on the substrate zone, however, in some cases the hot-wall configuration is necessary in order to avoid undesired convection due to a temperature gradient. Reactants may be involved into two different phase reactions, i.e. homogeneous reactions between the gaseous compounds, which leads to undesired gaseous homogeneous nucleation and non-adherent coating, and the heterogeneous reactions at the gas-solid interface.

A schematic representation of the reaction zones of a CVD process is shown in Fig. 2.2. The whole deposition mechanism may be described as the combination of two fundamental factors: the mass transport process and the kinetic-driven reactions. When the main gas-flow reaches the growth region, a part of atoms and intermediate species diffuses through the boundary layer region towards the substrate surface on which they are adsorbed and diffuse until they find an appropriate crystal lattice site where they finally crystallize. The reaction processes generate by-products which desorb and diffuse back towards the bulk of the flow, and then transported towards the outlet.

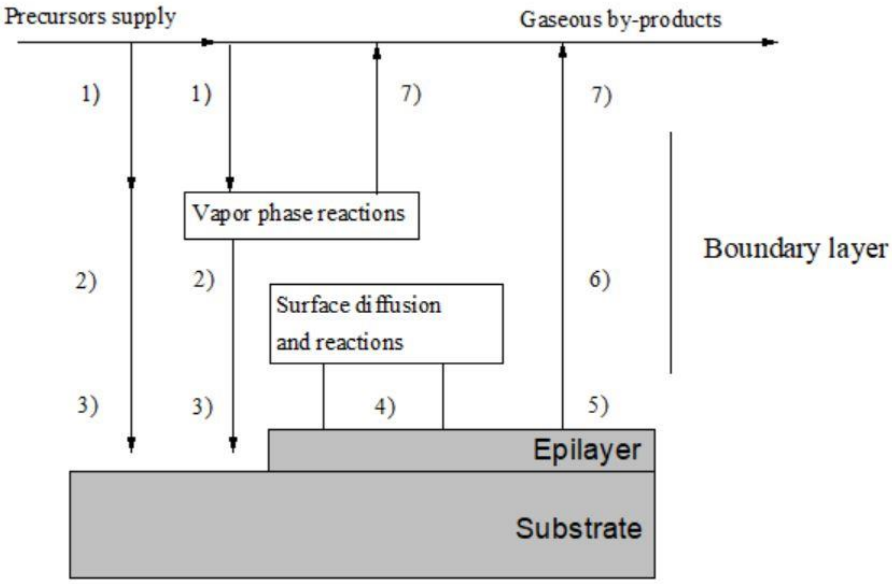

Fig. 2.2 Schematics of chemical and physical mechanisms of a CVD growth system: 1) precursor transport to the growth region, 2) gas phase diffusion of reactants and intermediates, 3) adsorption onto surface lattice sites, 4) surface diffusion and reactions of adsorbed species, 5) desorption of unreacted species and by-products, 6) by-products back-diffusion towards the main gas flow and 7) removal from the reactor.

Considering a growth system with different precursor species, a heterogeneous reaction could be defined as follow:

$$aA_{gas} + bB_{gas} + cC_{gas} \rightarrow M_{solid} + dD_{gas} \tag{2.1}$$

Where M corresponds to the solid final phase created, A, B and C are the reactant elements, D is the by-product desorbed species and a, b, c, d are the initial and final stoichiometric reaction coefficients of the phases. Equation (2.1) does not take into account any possible intermediate or homogeneous vapor phase reaction, however it can be used to describe the system thermodynamics.

An important role in vapor phase epitaxy reactions is the choice of the proper precursor species. These can be divided in several groups: halides, carbonyls, hydrides and metalorganics. The latter are involved in MOCVD growth technique and are classified as follow: methyl, ethyl, n-butyl, i-butyl, n-propyl, i-propyl and alkyl, with the additional prefixes mono (M), di (D) or tri (T) in order to define the quantity of specific radicals[88,90]. Reactants selection rules principally take into consideration properties such as toxicity, high degree of purity, pyrolysis temperature, economic convenience, stability at low temperature and reaction efficiency.

As anticipated, the aim of a CVD growth is to obtain a crystalline solid phase, as final product, through a series of chemical reactions, and the whole epitaxial process may be described and summarized in four conceptual tools:

- interface formation and phase transition thermodynamics
- mass transport fluid dynamics
- surface diffusion and reaction kinetics
- chemical bond creation, quantum mechanics

2.3 Thermodynamics aspects

The thermodynamic conditions related to a CVD process allow to define phase composition and to determine the growth mechanism driving force in an equilibrium system at constant pressure and temperature. Taking into consideration the reaction (2.1) previously reported, the reaction process equilibrium constant K is

$$\log(K) = \frac{\Delta G}{T} \;\; ; K(T) = \frac{p_A^a p_B^b p_C^c}{p_D^d}$$

where T is the temperature and ΔG represents the Gibbs free energy of the reaction. Furthermore, the p_I^i are the precursor and by-product species partial pressures taking part in the reaction. The chemical potential of a given system is an important parameter that allows to understand which reactions occur and to derive supersaturation optimal condition. The vapor phase chemical potential for the I-th species is

$$\mu_I(T) = \mu_I^0(T) + RTlogp_I$$

in which $\mu_I^0(T)$ is the standard chemical potential calculated at 1 atm pressure and temperature T. In equilibrium situation, solid and vapor phase chemical potentials result equal and the expression can be written as

$$\mu_{cryst} = \mu_{vapor} = a\mu_A^0 + b\mu_B^0 + c\mu_C^0 - d\mu_D^0 + RTlog\big(K_e(T)\big) \tag{2.2}$$

However, altering the vapor phase composition, by increasing reactants concentration and removing constantly the desorbed by-products, a non-equilibrium state is achieved that allows to obtain a steady growth process. Similarly to the expression (2.2), the chemical potential can be expressed as

$$\mu_{vapor} = a\mu_A^0 + b\mu_B^0 + c\mu_C^0 - d\mu_D^0 + RTlog\big(K(T)\big) \tag{2.3}$$

From expressions (2.2) and (2.3) the chemical potential difference it’s easily calculated as $\Delta\mu = \mu_{vapor} - \mu_{cryst}$, which identify the vapor phase supersaturation, i.e. the thermodynamic driving force of the growth process. It is possible to distinguish different situations related to the supersaturation, which define a successful or unsuccessful crystallization. In the case of $\Delta\mu = 0$, equilibrium condition is promoted, however as already explained, in order to achieve a crystal growth, an out-of-equilibrium system need to be created, which occurs only when $\Delta\mu > 0$ and leads to the solid film formation. The chemical potential difference can finally be rewritten as

$$\Delta\mu = RTlog\left(\frac{K(T)}{K_e(T)}\right) \tag{2.4}$$

Furthermore, in a non-equilibrium state the reaction rate in the growth direction is given by

$$R = \mathfrak{R}_{\rightarrow}\left[1 - e^{-\frac{\Delta\mu}{RT}}\right] \tag{2.5}$$

where $\mathfrak{R}$ strongly depend by the $\Delta\mu$, in fact under elevate supersaturation condition the reaction rate tend to the maximum value $\mathfrak{R}_{\rightarrow}$ and for decreasing $\Delta\mu$ the rate will decrease too approaching to the equilibrium case $\Delta\mu = 0$.

2.4 Gas flow dynamics and kinetic aspects

The gas behavior flowing into the growth chamber is controlled and defined by fluid dynamics laws. A typical reactant gas may be presents different states, such as molecular state and viscous state in which the mean free path is longer and shorter than the tube dimension, respectively. Two main regimes appear in a viscous state gas: a laminar flow regime, with low gas velocity and parallel flowing gas layer, and turbulent regime, characterized by higher velocities and chaotic movement. In order to obtain the desired deposition, a laminar regime has to be established. This is possible at decreased precursors velocity, which tends linearly to zero in the boundary layer region near any surface (substrate or reactor walls), generating an almost stagnant flow that controls the gaseous species transport toward the substrate. Instead, in turbulent regime condition or in presence of vortices (rolls), high flow rates and difficult transport control will cause an unsuccessful crystal growth and a decreasing conversion efficiency between metastable reactants and stable solid phase. Reynolds number is a dimensionless parameter which identify these different regimes in an isothermal environment and is expressed as

$$R_e = \frac{\rho V D}{\eta}$$

where ρ, V, D and η represent respectively the gas density, the velocity, the tube diameter and the viscosity. A laminar flow occurs for $R_e < 1100$, a turbulent regime appears for $R_e > 2100$ and a mixed condition is present in the intermediate range[91]. A schematic illustration of the flow modes is shown in Fig. 2.3, where they are displayed as a function of the Reynolds and Rayleigh number, another dimensionless quantity related to the flow regimes given by:

$$R_a = \frac{g \beta D^3 \Delta T}{\eta \alpha}$$

where g is the gravitational constant, β the thermal expansion coefficient, ΔT the temperature difference and α the thermal diffusivity.

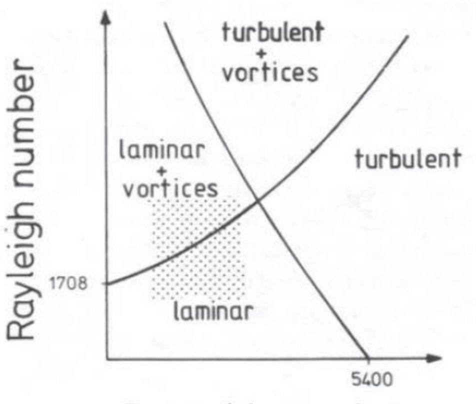

Fig. 2.3 Different flow-dynamical modes occurring as a function of Reynolds and Rayleigh numbers. In CVD growth laminar regime is the preferential mode, however sometimes vortices occur inside the reactor due to a border line temperature gradient. (Reproduced from Ref.88).

Furthermore, in order to provide a complete description of the fluid dynamics that can occurs in a CVD process it is necessary to define the profile of velocity, temperature and vapor species concentration in the boundary layer regions. In particular, these regions correspond to the zones starting from the inlet of the reactor and increasing in thickness until a flow stabilization. Here the parameter profiles, already introduced, result different from the same quantities in the main gas stream. The boundary layer thickness can be written as $\delta = (\frac{x}{R_e})$, in which x is the distance from the inlet and R_e is the Reynolds number. The thickness clearly increases with increasing x and with decreasing gas flow velocity.

The gas velocity profile results uniform and parallel to the tube walls on the entrance (laminar-flow), however it is quickly influenced by the null-velocity boundary condition and a large gradient comes out between the maximum and zero velocity at the reactor central core and near every surface into the chamber, respectively. Velocity, temperature and reactant concentration profiles are well identified in Fig. 2.4 and itis evident that the boundary layer may correspond for each variable[90].

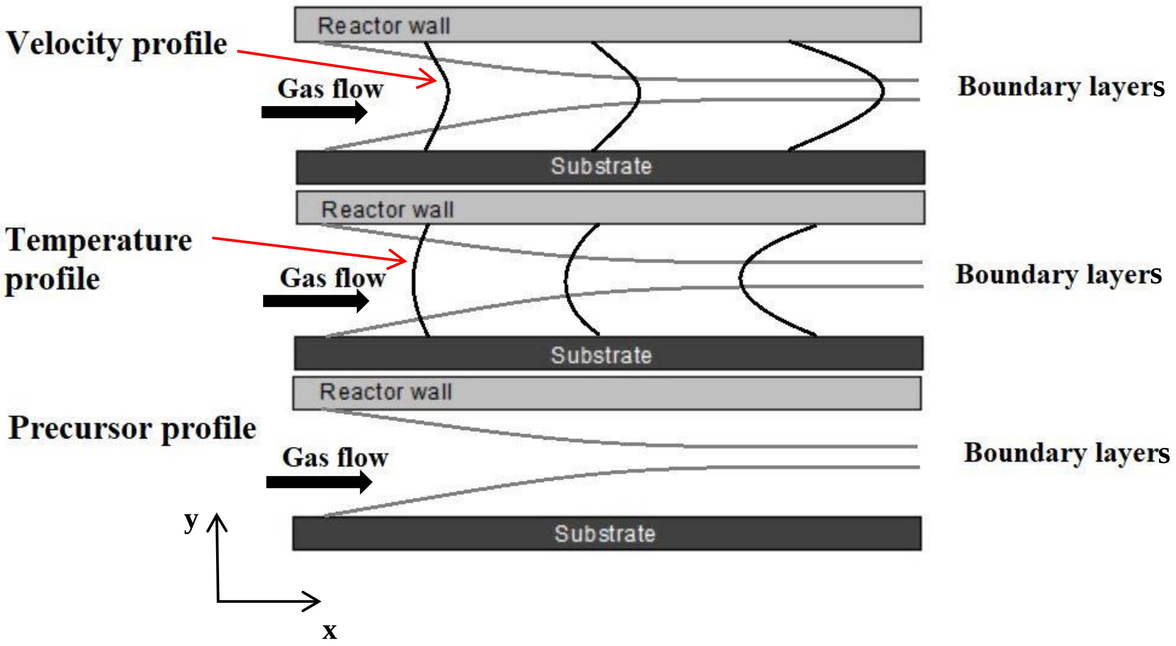

Fig. 2.4 Schematic velocity, temperature and concentration profiles and boundary layers in a horizontal geometry CVD reactor chamber.

As anticipated, mass transport and kinetic reaction mechanisms play an active role in CVD process and allow to determine the growth rate. Mass transport phenomena occur when precursors and by-products are supplied and removed, respectively, by the flowing carrier gas and also when gas species atoms or molecules diffuse during the growth due to concentration and thermal gradients (convective and diffusive fluxes). The convective and diffusive transport of the reactants can be expressed by

$$J_i = J_i^{conv} + J_i^{diff} = \frac{p_i v}{kT} - \frac{D_i}{kT}\left[\nabla p_i + \frac{\alpha_i}{T} p_i \nabla T\right] \tag{2.6}$$

where p_i is the partial pressure of the i-th species, D_i and α_i correspond to the diffusion and the thermo-diffusion coefficients of the species i in the vapor phase. The diffusive component is formed by two contributions deriving from ordinary diffusion and thermo-diffusion (Soret effect) generated by concentration gradient and temperature gradient, respectively. The convective component affects the transport outside the boundary layer region, together with the diffusive one, however, near the substrate, convection tends to be null and diffusion results dominant.

In order to analyze correctly mass transport processes, basic Navier-Stokes equations need to be taken into consideration[89]. In Fig. 2.2 the sequential CVD growth process steps were defined and these are characterized by growth rate limitations, causing different consequences on the deposited material properties. These limitations are divided in several categories: *thermodynamic control, surface kinetics control, mass transport control, nucleation control and homogeneous reaction control.* The last two rate-limiting steps are important when the growth velocity is driven by nucleation at low supersaturation (nucleation limitation) or by certain gaseous species (homogeneous reaction limitation). On the other hand, the overall deposition rate is mostly controlled by the combined balance of the first three phenomena. In the case of thermodynamic control, it occurs, under high temperatures and low flow velocity, when the deposition velocity and the rate of the gases introduced into the growth chamber are equal. The mass transport regime dominates at lower temperature and low partial pressure conditions, and fast surface reactions as well as slow supplied precursors in metastable vapor phase arise. In the kinetic driven process fast reactants diffusion into the main flow is combined with slow reaction, creating a favorable mechanism to deposit at the solid-vapor interface under large partial pressures and further lower temperatures. Furthermore, mass transport and kinetic transport controls present also a different temperature dependence. If the first is weakly influenced because both convective and diffusive flows are only indirectly dependent on the temperature, the latter exhibits an exponential behavior as shown in Fig. 2.5.

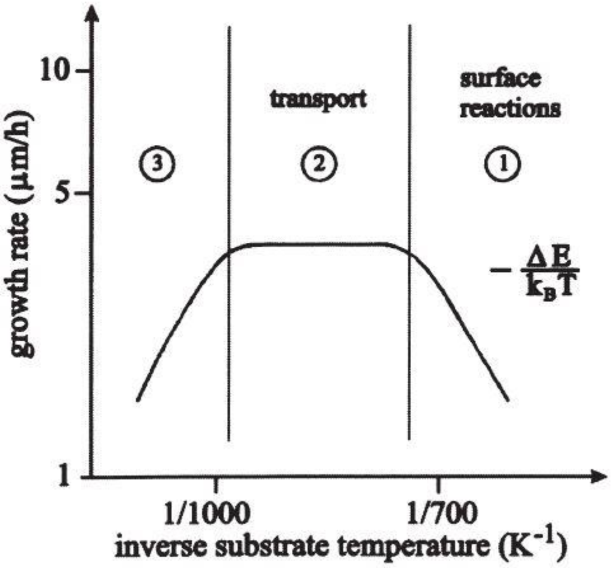

Fig. 2.5 Temperature dependence of three main regimes in a MOCVD growth. (Reproduced from Ref.88)

At very high temperatures a decreasing growth rate is observed (zone (3) in Fig. 2.5). This phenomenon might be due to a growing species desorption from the surface or to a pre-deposition on the reactor walls caused by a wide increase of temperature throughout the reactor chamber.

2.5 Epitaxial growth setups and parameters

Gallium oxide thin film growth was carried out at IMEM-CNR Institute in a home-made MOCVD reactor, with horizontal geometry. In this reactor, a non-rotating graphite susceptor is centrally positioned with a round cavity on its top ideated to contain a two inches *c*-Al_2O_3 substrate. In the backside part of this graphite plate three holes are present in which two resistor plugs are inserted in order to heat the susceptor and the substrates on it, and a thermocouple located in the central hole. The thermocouple communicates with a PID (proportional-integral-derivative) controller which ensures a desired plate temperature modulating the supplied power. The graphite heater surface is built with a slope angle of 5° with respect to the horizontal gas flow with the aim of improve the boundary layer homogeneity. Different precautions inside the reactor allow to deposit high quality thin films. In order to protect the deposition from contaminants and promote a laminar flow, a quartz cover was applied on the top and, moreover, a porous graphite 'sponge' positioned around the susceptor limits the heat dispersion. Precursors involved in the deposition process are trimethylgallium (TMGa) and ultrapure water, both stored, in liquid form under constant temperature control at 1-5°C and 30°C respectively, in stainless steel containers called “bubblers”. The vapor pressure of these regulated thermostatic baths is controlled and after imposing a certain pressure value carrier gas (H_2) flows out “bubbling” through the liquid and flowing in the vapor above (see Fig. 2.6). The water choice, instead of molecular O_2, is related to a better surface morphology and generally to a good thin film growth, as also reported for the β-phase[13,92]. A double-dilution line system, formed by two separated lines, is used to deliver gas species into the reactor in order to avoid a precursors pre-mixing and reactions in the gas phase. A vent line is also connected to the precursor lines and to the reactor. This line allows a flow stabilization before switching them into the reactor; it further leads the process residual gases to a cracking furnace which decompose unreacted species at 650°C. Different purified carrier gases were tested (H_2, N_2, He, Ar), however a better ε-Ga_2O_3 crystal quality was reached employing hydrogen and helium. Fig. 2.6 shows the MOCVD growth system just described.

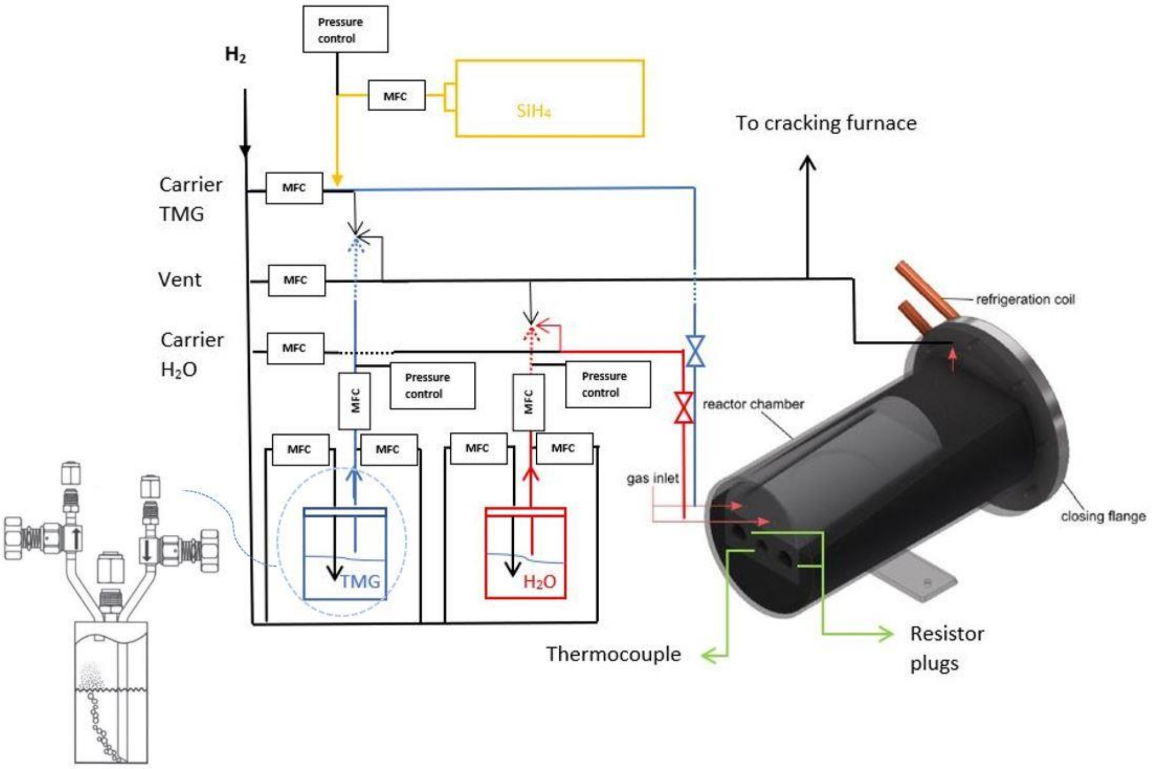

Fig. 2.6 Schematic representation of the home-made MOCVD system for the ε-Ga_2O_3 thin film growths. On the left the detail of a bubbler holding liquid phase precursors and the generated vapor phase reactants flowed to the reactor chamber.

Reactor chamber total pressure, monitored by a rotary pump, is varied from ambient pressure to about 80mbar, while reactants amount, quantified in sccm (standard cubic centimeters per minute), and their partial pressures are controlled by mass flow controllers (MFCs) and by bubblers pressure and temperature regulation. Precursor partial pressure P_{gp} inside the reactor [91] may be written:

$$P_{gp} = \frac{F_{bubb} P_{reactor}}{F_{tot} P_{bubb}} \tag{2.7}$$

where F_{bubb} is the flow through the bubblers, F_{tot} represents the total gas flowing into the chamber, $P_{reactor}$ and P_{bubb} correspond to the total pressure and to the partial pressure into the bubbler, respectively. The $P_{vap}(T)$ parameter [93–95], i.e. TMGa or water vapor pressure inside the bubblers, introduces the partial pressure temperature dependence and can be expressed from the following simple relations

$$log_{10} P_{TMGa} = \left(8.07 - \frac{1703}{T_{TMG,bubb}}\right); lnP_{H2O} = \left(20.386 - \frac{5132}{T_{H2O,bubb}}\right) \tag{2.8}$$

in which the temperature and the vapor pressure are expressed in K and mmHg, respectively.

Chemical reactions that may occur at solid-gas interface have been proposed by Baldini *et al.*[92] starting from the consideration that trimethylgallium pyrolize in double-step unimolecular reaction, first losing methyl groups and then forming monomethylgallium (2.9-2.10)[88,96–98], thus the latter tends to hydrolize in water generating $Ga(OH_3)$ and finally Ga_2O_3 (2.11-2.12). The reactions can be expressed as follow

$$Ga(CH_3)_3 \longrightarrow Ga(CH_3)_2 + CH_3 \tag{2.9}$$

$$Ga(CH_3)_2 \longrightarrow Ga(CH_3) + CH_3 \tag{2.10}$$

$$Ga(CH_3) + 3H_2O \longrightarrow Ga(OH)_3 + CH_4 + H_2 \tag{2.11}$$

$$2Ga(OH)_3 \longrightarrow Ga_2O_3 + 3H_2O \tag{2.12}$$

Furthermore, in order to achieve Si-doped thin films, an external silane source was provided. For the experiments described in this thesis a diluted mixture of 0.05% silane (SiH_4) in pure hydrogen (H_2) was employed. Silane is injected from its container into the TMGa line and they flow together to the reactor chamber. The silane partial pressure is calculated as the ratio between the effective SiH_4 flow (F_{Si}) and the total flow (F_{tot}) that reaches the reactor. Silane is known to pyrolize in silylene or disilane through unimolecular homogeneous reactions[99], however chemical reaction mechanisms which involve the silane and gallium oxide precursors are not yet detailed studied.

The best MOCVD growths of undoped and Si-doped Ga_2O_3 films, with the most representative parameters are reported in the following Table 2.1 and Table 2.2.

Samples (#)	**T(K)**	**P(mbar)**	P_{TMGa}	P_{H_2O}	$\frac{H_2O}{TMGa}$	**Carrier gas**	**Time(min)**
270	600	60	1.70E-02	1.17E-04	145	H_2	30
271	600	60	1.70E-02	1.17E-04	145	H_2	30
272	600	60	6.90E-02	1.08E-04	640	H_2	30
273	600	60	6.90E-02	1.08E-04	640	H_2	3
274	600	60	1.81E-01	6.59E-04	275	H_2	54
275	600	60	1.81E-01	5.27E-04	343	H_2	49
276	600	60	1.81E-01	5.27E-04	343	H_2	201
277	600	60	1.81E-01	5.27E-04	343	H_2	201
278	600	60	1.81E-01	5.27E-04	343	H_2	201
279	600	60	6.90E-02	1.08E-04	640	H_2	30
280	600	60	1.81E-01	5.27E-04	343	H_2	201
281	600	60	1.81E-01	5.27E-04	343	H_2	201
298	600	60	1.45E-02	1.17E-04	125	H_2	30
299	610	60	1.70E-02	1.17E-04	145	H_2	60
300	600	80	4.85E-02	1.11E-04	436	H_2	60
301	600	80	1.70E-02	1.17E-04	145	H_2	60
302	610	75	9.08E-02	1.04E-04	872	H_2	60
303	610	75	9.08E-02	1.04E-04	872	H_2	60
304	610	75	1.70E-02	1.17E-04	145	H_2	60
305	610	75	1.70E-02	1.17E-04	145	H_2	60
317	600	60	1.70E-02	1.17E-04	145	H_2	40
318	600	60	1.70E-02	1.17E-04	145	H_2	40
319	600	60	1.70E-02	1.17E-04	145	H_2	40
320	600	60	1.70E-02	1.17E-04	145	H_2	40
321	600	60	1.70E-02	1.17E-04	145	H_2	40
322	600	60	1.70E-02	1.17E-04	145	H_2	40
323	600	60	1.70E-02	1.17E-04	145	H_2	40
324	600	60	1.70E-02	1.17E-04	145	H_2	40
325	600	60	1.70E-02	1.17E-04	145	H_2	40
330	600	60	1.70E-02	1.17E-04	145	H_2	60
331	600	80	1.74E-02	1.60E-04	109	H_2	60
332	600	60	1.70E-02	1.17E-04	145	H_2	60
333	610	60	1.70E-02	1.17E-04	145	H_2	60
334	610	60	1.70E-02	1.17E-04	145	H_2	60

336	610	72	1.41E-02	1.17E-04	121	N_2	60
337	610	72	1.41E-02	1.17E-04	121	N_2	60
338	610	72	2.76E-02	1.14E-04	242	N_2	60
339	610	72	3.41E-02	1.41E-04	242	N_2	60
340	610	72	3.05E-02	1.26E-04	242	N_2	60
341	610	72	2.76E-02	1.14E-04	242	N_2	120
357	610	60	3.19E-05	1.70E-02	145	H_2	60
367	610	75	3.87E-02	1.67E-04	233	H_2	120
368	610	60	1.70E-02	1.17E-04	145	H_2	60
369	610	60	1.70E-02	1.17E-04	145	H_2	60
370	610	60	2.51E-02	1.73E-04	145	H_2	60
371	610	60	3.31E-02	1.70E-04	194	H_2	60
372	610	60	4.84E-02	1.67E-04	291	H_2	60
373	610	60	4.84E-02	1.67E-04	291	H_2	60
377	610	60	4.86E-05	1.70E-02	291	H_2	50
378	610	60	4.95E-05	5.18E-03	291	H_2	60
379	610	60	4.84E-02	1.67E-04	291	H_2	60
380	610	60	9.00E-02	3.10E-04	194	H_2	60
381	610	60	4.84E-02	1.67E-04	174	H_2	60
382	610	60	3.31E-02	1.70E-04	291	H_2	60
383	610	60	4.84E-02	2.78E-04	291	H_2	60
384	610	60	4.84E-02	1.67E-04	291	H_2	20
385	610	60	4.84E-02	1.67E-04	291	H_2	120
386	610	60	1.70E-02	1.17E-04	145	H_2	34
387	610	60	1.70E-02	1.17E-04	145	H_2	34
388	610	60	1.70E-02	9.72E-05	349	H_2	34
389	610	60	3.31E-02	9.49E-05	698	H_2	30
390	610	60	6.33E-02	9.06E-05	352	H_2	30
391	610	60	7.59E-03	2.16E-05	352	H_2	60
386	610	60	3.31E-02	9.49E-05	349	H_2	15
387	610	60	3.31E-02	9.49E-05	349	H_2	60
400	610	60	3.31E-02	9.49E-05	349	H_2	13
401	610	60	3.31E-02	9.49E-05	349	H_2	13
402	610	60	3.31E-02	9.49E-05	349	H_2	20
403	610	60	3.31E-02	9.49E-05	349	H_2	20
404	610	60	3.31E-02	4.77E-05	695	H_2	30
405	610	60	3.31E-02	9.49E-05	349	H_2	20
406	610	60	3.31E-02	9.49E-05	349	H_2	20
407	610	60	3.31E-02	9.49E-05	349	H_2	20
408	610	60	1.70E-02	4.86E-05	349	H_2	42
409	610	60	3.31E-02	9.49E-05	349	H_2	20

410	610	60	3.31E-02	9.49E-05	349	H_2	20
411	610	60	3.31E-02	9.49E-05	349	H_2	20
412	610	60	3.31E-02	9.49E-05	349	H_2	20
413	610	60	3.31E-02	9.49E-05	349	H_2	20
414	610	60	3.31E-02	9.49E-05	349	H_2	15
415	610	60	3.31E-02	9.49E-05	349	H_2	15
416	610	60	3.31E-02	9.49E-05	349	H_2	25
417	610	60	3.31E-02	9.49E-05	349	H_2	25
418	610	60	3.31E-02	9.49E-05	349	H_2	10
419	610	60	3.31E-02	9.49E-05	349	H_2	1
420	610	60	3.31E-02	9.49E-05	349	H_2	22
421	610	60	3.31E-02	9.49E-05	349	H_2	22
422	610	60	3.31E-02	9.49E-05	349	H_2	22
423	610	60	3.31E-02	9.49E-05	349	H_2	1.5
425	610	60	2.43E-05	9.49E-05	349	H_2	320
433	610	60	3.19E-05	2.43E-05	698	H_2	60
434	610	60	6.71E-05	3.19E-05	532	H_2	60
435	610	60	4.86E-05	6.71E-05	252	H_2	60
436	610	60	2.43E-05	4.86E-05	349	H_2	60

Table 2.2 List of undoped samples grown by MOCVD and related growth parameters. Partial pressures P_{TMGa} and P_{H2O} are calculated by (2.8) equations.

Samples (#)	**T(K)**	**P(mbar)**	P_{TMGa}	P_{H_2O}	$\frac{H_2O}{TMGa}$	**Time(min)**	**Carrier gas**	**SiH_4 flow (sccm)**
306	600	60	1.17E-04	1.70E-02	145	60	H_2	0.001
307	600	60	1.17E-04	1.70E-02	145	60	H_2	0.005
308	600	60	1.17E-04	1.70E-02	145	60	H_2	0.00025
309	600	60	1.17E-04	1.70E-02	145	60	H_2	0.0025
311	600	60	1.17E-04	1.70E-02	145	60	H_2	0.0025
312	600	60	1.17E-04	1.70E-02	145	60	H_2	0.05
313	600	60	1.17E-04	1.70E-02	145	60	H_2	0.25
314	600	60	1.23E-04	1.78E-02	145	60	H_2	0.05
316	600	60	6.59E-04	1.81E-01	275	201	H_2	0.05
326	600	60	1.17E-04	1.70E-02	145	60	H_2	0.005
327	600	60	1.17E-04	1.70E-02	145	60	H_2	0.01
328	600	60	1.17E-04	1.70E-02	145	60	H_2	0.005
329	600	60	1.17E-04	1.70E-02	145	60	H_2	0.005
335	610	60	1.17E-04	1.70E-02	145	60	H_2	0.005
342	600	80	1.14E-04	2.48E-02	218	120	N_2	0.005

344	600	80	1.14E-04	2.48E-02	218	120	N_2	0.001
347	610	75	1.67E-04	3.87E-02	233	122	N_2	0.0125
348	610	75	1.67E-04	3.87E-02	233	120	N_2	0.0125
349	610	75	1.67E-04	3.87E-02	233	120	N_2	0.0125
356	600	60	1.17E-04	1.70E-02	145	60	H_2	0.005
358	600	60	1.17E-04	1.70E-02	145	62	H_2	0.005
365	610	75	1.67E-04	3.87E-02	233	120	N_2	0.025
366	610	75	1.67E-04	3.87E-02	233	120	N_2	0.025
374	610	60	1.67E-04	4.84E-02	291	60	H_2	0.05
375	610	60	1.67E-04	4.84E-02	291	120	H_2	0.05
376	610	60	1.67E-04	4.84E-02	291	120	H_2	0.005
393	610	60	9.49E-05	3.31E-02	349	62	H_2	0.005
394	610	60	9.49E-05	3.31E-02	349	62	H_2	0.001
396	610	60	9.06E-05	6.33E-02	698	62	H_2	0.005
397	610	60	4.77E-05	3.31E-02	695	62	H_2	0.005
399	610	60	9.49E-05	3.31E-02	349	62	H_2	0.005
426	610	60	9.49E-05	3.31E-02	349	60	H_2	0.005
427	610	60	9.82E-05	9.94E-03	101	60	H_2	0.005
428	610	60	9.82E-05	9.94E-03	101	60	H_2	0.005
429	610	60	9.49E-05	3.31E-02	349	60	H_2	0.0125
430	610	60	9.49E-05	3.31E-02	349	60	H_2	0.0125
431	610	60	9.49E-05	3.31E-02	349	60	H_2	0.025
432	610	60	9.49E-05	3.31E-02	349	60	H_2	0.005
437	610	60	2.43E-05	1.70E-02	698	120	H_2	0.005
438	610	60	3.19E-05	1.70E-02	532	60	H_2	0.005
439	610	60	4.86E-05	1.70E-02	349	60	H_2	0.005
440	610	60	4.86E-05	1.70E-02	349	60	H_2	0.005
441	610	60	3.19E-05	1.70E-02	532	60	H_2	0.005
442	610	60	3.19E-05	1.70E-02	532	60	H_2	0.005
443	610	60	4.86E-05	1.70E-02	349	60	H_2	0.0125
444	610	60	2.46E-05	8.59E-03	349	120	H_2	0.005
447	610	60	4.86E-05	1.70E-02	349	62	H_2	0.005
448	610	60	4.86E-05	1.70E-02	349	62	H_2	0.0075
450	610	60	4.95E-05	5.18E-03	105	62	H_2	0.005

Table 2.1 List of Si-doped samples grown by MOCVD and related growth parameters.

Chapter 3 - Thermal stability of ε-Ga_2O_3

The thermal stability of MOCVD ε-Ga_2O_3 thin films, investigated by different techniques, will be discussed in this chapter in order to study the actual phase stability and the transition temperature.

As already anticipated, the thermodynamically metastable nature of ε-Ga_2O_3 implies that this polymorph tends to convert to β-phase at relatively high temperature. Nevertheless, considering its better matching with different substrates and its higher crystallographic symmetry, the ε-phase material may be used for device fabrication, provided that all fabrication steps fall in the temperature range where the phase is thermally stable. As shown at a later point, the upper threshold is about 700°C.

When a structure identified as ε-Ga_2O_3 was synthesized for the first time in the fifties[26], the authors found that it remained stable up to 870°C, though the crystal structure was not yet really known and continued to be unclear for more than fifty years. In the last few years, the ε-polymorph was epitaxially obtained by several groups[23,46,68], and specific structural analysis revealed its real crystal structure[33]. Consequently, the thermal stability of ε-phase has been further investigated[23,68]. Oshima *et al.*[23] first reported results about the crystal structure evolution of HVPE growth films on GaN substrates, under different annealing temperature. In Fig. 3.1a, a set of HT-XRD measurements recorded at different T is shown and one can note that the ε-phase diffraction peaks dominates up to 700°C. The further increase of the temperature causes the appearance of the β-Ga_2O_3 (401) peak and, while the β-phase intensity increases, the ε-Ga_2O_3 (0004*)* intensity rapidly decreases, almost disappearing around 800°C. Gallium oxide phase transition has been studied also by Xia *et al.*[68], performing HR-XRD measurements on MOCVD thin films grown on 6H-SiC substrates, in a temperature range from 700°C to 1000°C with a step of 50°C. Fig. 3.1b shows the spectra of the as-grown (A) and annealed samples (800°C = B, 850°C = C, 900°C = D). The spectrum of 850°C annealed film shows β-Ga_2O_3 (-603) diffraction peak together with a decreasing ε-Ga_2O_3 (0006) peak, while the latter completely disappears at 900°C annealing temperature. Therefore, this indicates that MOCVD growth of ε-phase thin films results thermally stable up to 800°C, i.e. the complete phase transformation to β-polymorph occurs at higher temperature compared to HVPE-grown films.

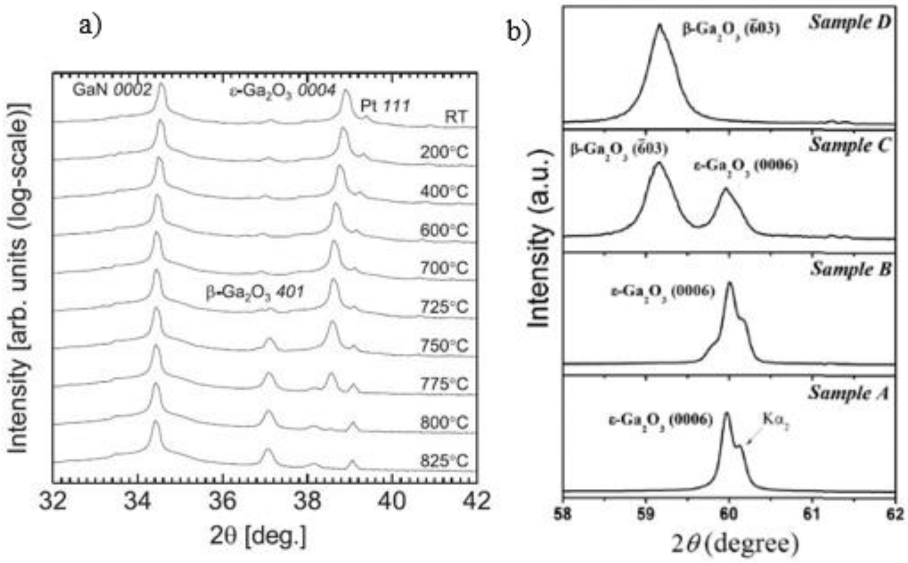

Fig. 3.1 a) HT-XRD patterns of as-grown and thermally treated ε-Ga_2O_3 grown on GaN (0001) substrate and b) amplified XRD data of as-grown and thermally treated ε-phase films grown on 6H-SiC. (Reproduced from Ref.[23] and Ref.68).

3.1 Thermal stability - Experimental set up and results

For the first time, a full study on thermally activated Ga_2O_3 transition phase from ε- to β-polymorph has been carried out in the frame of the present thesis performing several complementary characterization methods [100]. The ε-Ga_2O_3 specimens were selected with a size of about 0.6 x 0.6 cm^2, cut from thin films deposited by MOCVD on (001)-oriented Al_2O_3 at 650°C and low pressure. Ultrapure water and Trimethylgallium (TMG) were used as precursors and delivered to the growth reactor with He as carrier gas. The reactants flows were set to obtain a H_2O/TMG partial pressure ratio of 1000. After the cleaning steps with organic solvents, the as-grown samples were placed into a Eurotherm tubular furnace for the annealing procedure. Table 3.1 reports the list of samples along with the parameters of annealing experiments.

Sample#	**Annealing Temp. (°C)**	**Time (h)**	**Ambient gas**	**Average cooling rate in different temperature ranges between actual gas annealing temperature and 500°C (°C/min)**					**Film thickness (nm)**	**Final phase**
				1000-900°C	900-800°C	800-700°C	700-600°C	600-500°C		
146b2	700	3	O_2				3.0	2.7	500	ε
146g1	700	3	N_2				3.0	2.7	500	ε
146g2	800	3	O_2			3.8	3.0	2.7	500	~ε
146g3	800	3	N_2			3.8	3.0	2.7	500	-
146g5	900	3	O_2		5.0	3.8	3.0	2.7	500	β
146g6	900	3	N_2		5.0	3.8	3.0	2.7	500	β
146c	1000	6	O_2	7.5	5.0	3.8	3.0	2.7	500	β
146e	1000	2	O_2	2.0	2.0	2.0	2.0	2.0	500	β
224d	1000	3	O_2	7.5	2.0	3.8	3.0	2.7	450	β

Table 3.1 Summary of relevant parameters and annealing procedures of ε-phase epilayers.(Reproduced from Ref.100).

Concerning the annealing procedure, a duration time of 2-3 h was chosen, i.e. much longer than any technological step involved in device fabrication. Treatments at 700°C, 800°C and 900°C were carried out, separately, in oxygen or nitrogen atmosphere to investigate the decomposition of ε-Ga_2O_3 (oxygen escape) occurring under high temperature in different ambients. The reported average cooling rates value identify the furnace cooling rate between the given annealing temperature and 500°C, with steps of 100°C. Below 500°C the cooling rate rapidly decreases, due to furnace inertia, and the system need several hours to reach the room temperature. Anyway, also for extended period, these temperatures do not cause changing of crystallographic features.

XRD measurements were performed before and after thermal processes by using ARL X’tra diffractometer equipped with a Si(Li) Thermo Electron solid-state detector and CuK_α radiation. Some specimens were further investigated by TEM analysis. During the preparation steps, samples, in cross-section position, were thinned by Ar ion beam milling and, then, in order to prevent charge effect, a few nm of amorphous carbon layer was evaporated on the surface. Thus, the TEM investigations were carried out by partners at the Institute for Technical Physics and Materials Science, Hungarian Academy of Sciences, Budapest, using a Philips CM20 transmission electron microscope operating at 200kV. SAED patterns and HR-TEM images were acquired by using a JEOL 3010 working at 300kV and equipped with LaB_6 cathode and Gatan Orius CCD camera. Finally, a very thick ε-phase film (about 10µm), grown for a longer time exactly with the same parameters of other samples, was examined by DSC, by partner at the Leibniz Institute for Crystal Growth in Berlin, using a NETZSCH STA 449C "Jupiter" equipment.

Concerning XRD patterns, all as-grown samples result to be pure-phase ε-Ga_2O_3, with typical peaks related to (002), (004) and (006) reflections and positioned at 2θ = 19.17°, 38.35°, 59.87° respectively (see Fig. 3.2). After thermal treatments at 700°C for 3 h, either in N_2 or O_2 atmosphere, the samples 146b2 and 146g1 show an unchanged structure as observable in Fig. 3.3. At 800°C annealing temperature the ε-phase peak intensities strongly decreased, in particular in N_2 ambient, and no reflections were detected (neither ε- nor β-peaks), except the sapphire contribution (Fig. 3.4). The absence of β-phase and the 'annihilation' of the ε-reflection intensities suggests that at 800°C the structure lies in an intermediary disordered condition. Thus, the X-ray patterns demonstrates a loss of sample crystallinity, independently of the annealing ambient, that could be caused by a domain reduction to nano-domain, due to the exposition for a long period to high temperature, with a size lower than the typical coherence length of the X-ray. After several months these measurements were repeated and it could be said that this "amorphization" results permanent. A complete conversion to β-phase is observed in samples annealed at 900°C (146g5 and 146g6), where typical (-201) orientation gives rise to a peak sequence positioned at 2θ = 18.97°, 38.46°, 59.2° (Fig 3.5). Compared to as-grown samples, the β-converted films showed a specific broadening and a lower intensity of the peaks which indicates that the new crystalline structure due to phase transition is strongly defected. Noteworthy, the different atmospheres (O_2 or N_2) involved in the thermal treatments produced the same behavior, confirming a notable stoichiometry and composition stability of Ga_2O_3 in the explored temperature range.

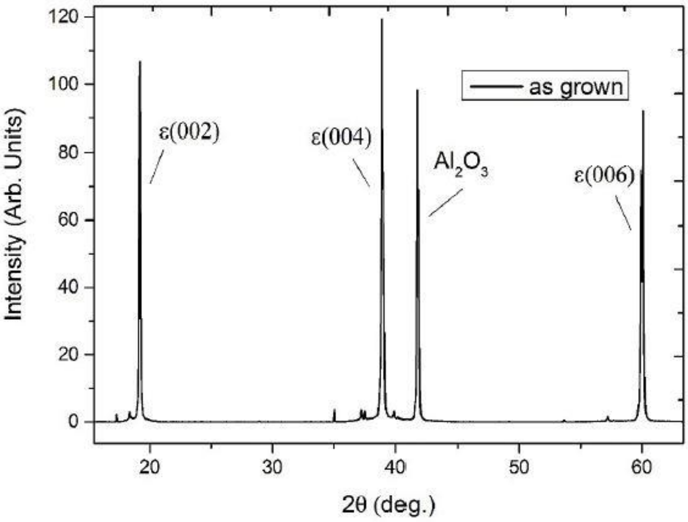

Fig. 3.2 X-ray diffraction pattern of MOCVD as-grown ε- Ga_2O_3. (Reproduced from Ref.100).

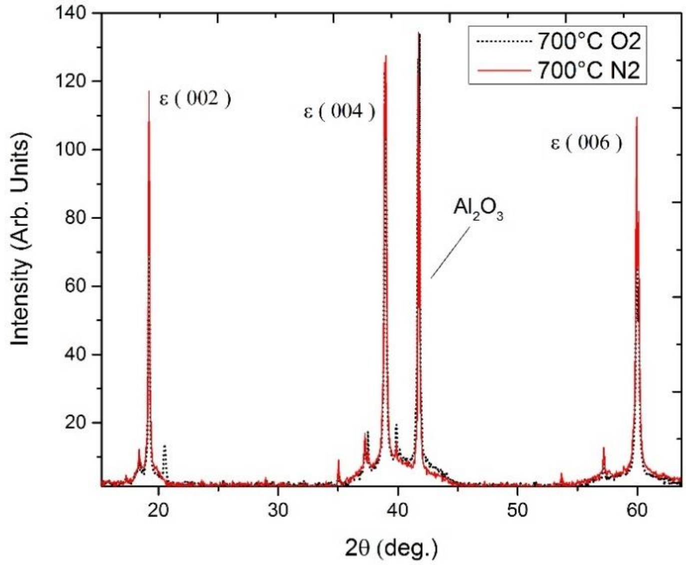

Fig. 3.3 X-ray diffraction pattern of MOCVD ε-Ga_2O_3 thin films annealed under O_2 and N_2 atmosphere at 700°C. (Reproduced from Ref.100).

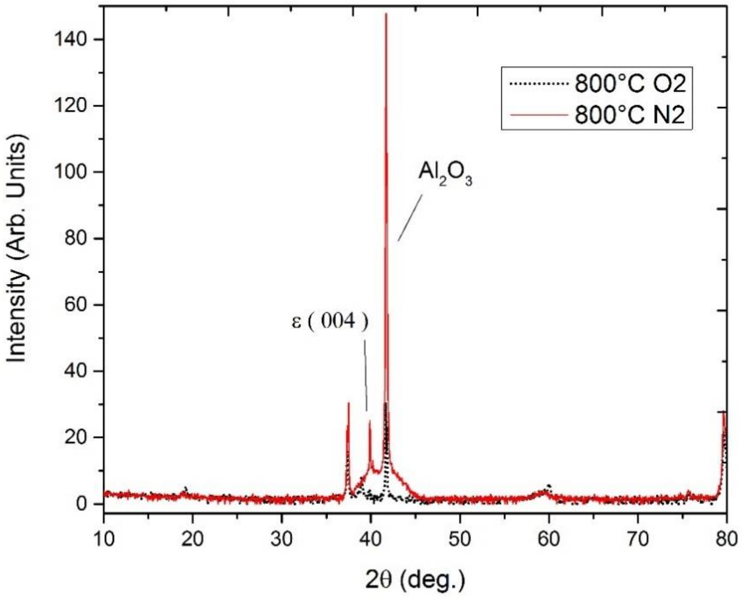

Fig. 3.4 X-ray diffraction pattern of MOCVD ε-Ga_2O_3 thin films annealed under O_2 and N_2 atmosphere at 800°C.

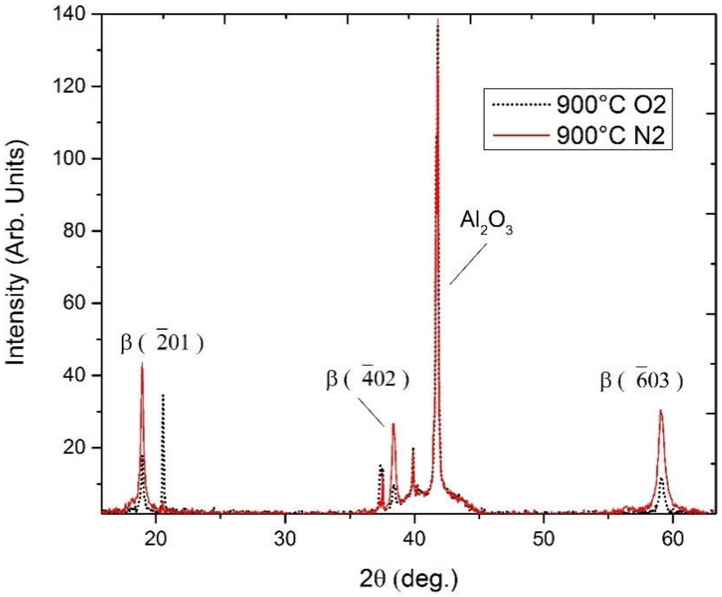

Fig. 3.5 X-ray diffraction pattern of MOCVD ε-Ga_2O_3 thin films annealed under O_2 and N_2 atmosphere at 900°C. (Reproduced from Ref.100).

Thermal treatments of ε-thin films at 1000°C in oxygen atmosphere exhibit a complete conversion to β-phase (146c and 146e) even for 2 h annealing time, confirmed also by high-resolution (HR)-TEM investigations. A substantial difference was observed in lattice orientation between samples cooled rapidly or slowly. In Fig. 3.6, the cross-section of sample #146c, which was initially cooled at relatively fast rate (~7.5°C/min, see Table 3.1), shows a film completely consisting of β-polymorph and two wide sub-layers, with different in-plane orientations but with the same out-of-plane orientation [310]* (see Fig. 3.6a,b,c). Instead, a slow cooling (2°C/min), in the case of #146e specimen, seems to promote the formation of β-Ga_2O_3 grains (Fig. 3.7), with the same [-201]* orientation parallel to the [001]* substrate direction and four different in-plane orientations, originated from two pairs of (-201)-type twins.

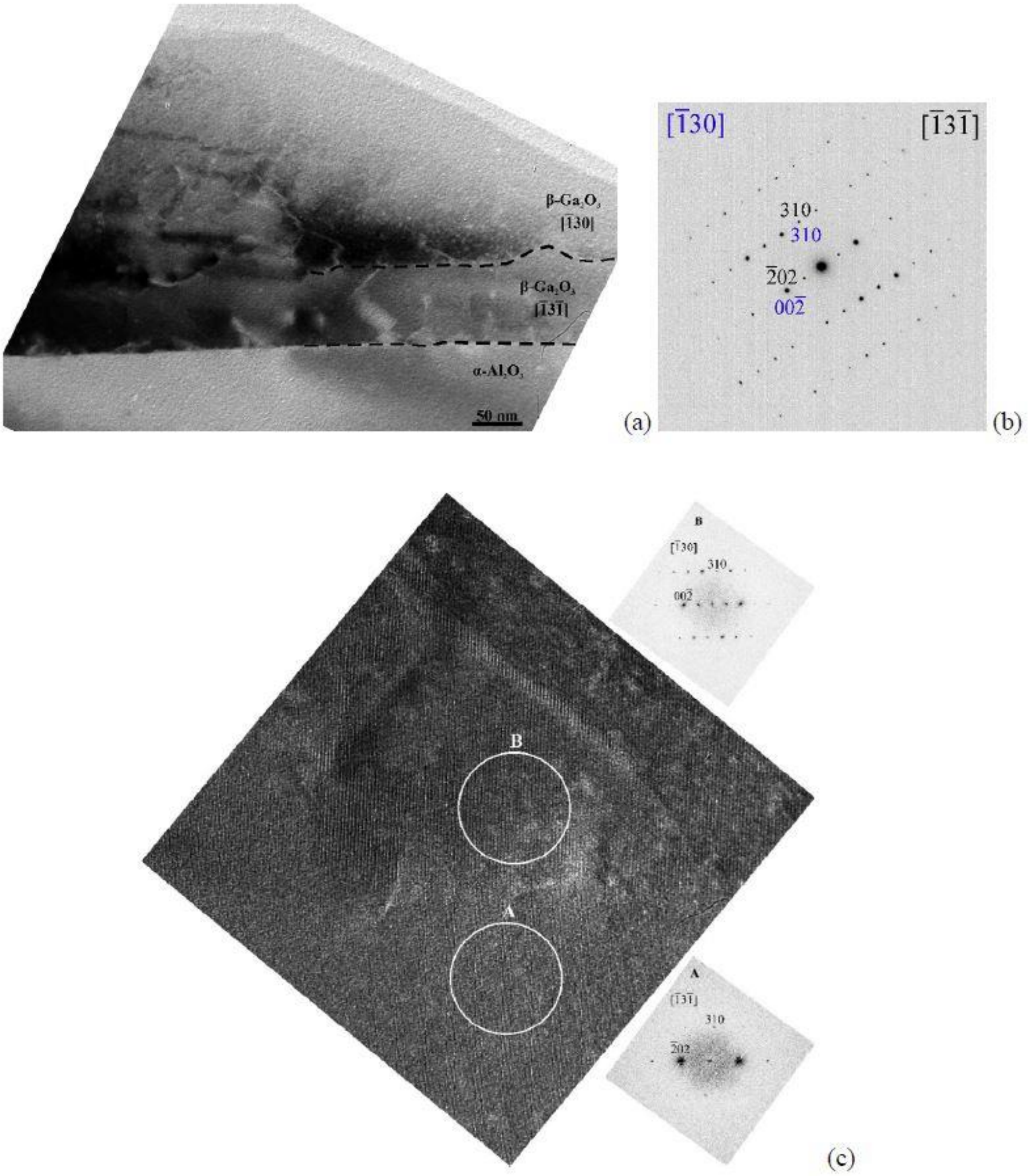

Fig. 3.6 TEM analysis of sample #146c thermally treated at 1000°C and cooled rapidly; a) BF, b) SAED and c) HRTEM image with the corresponding FFTs which demonstrate the presence of β-Ga_2O_3. (Reproduced from Ref.100).

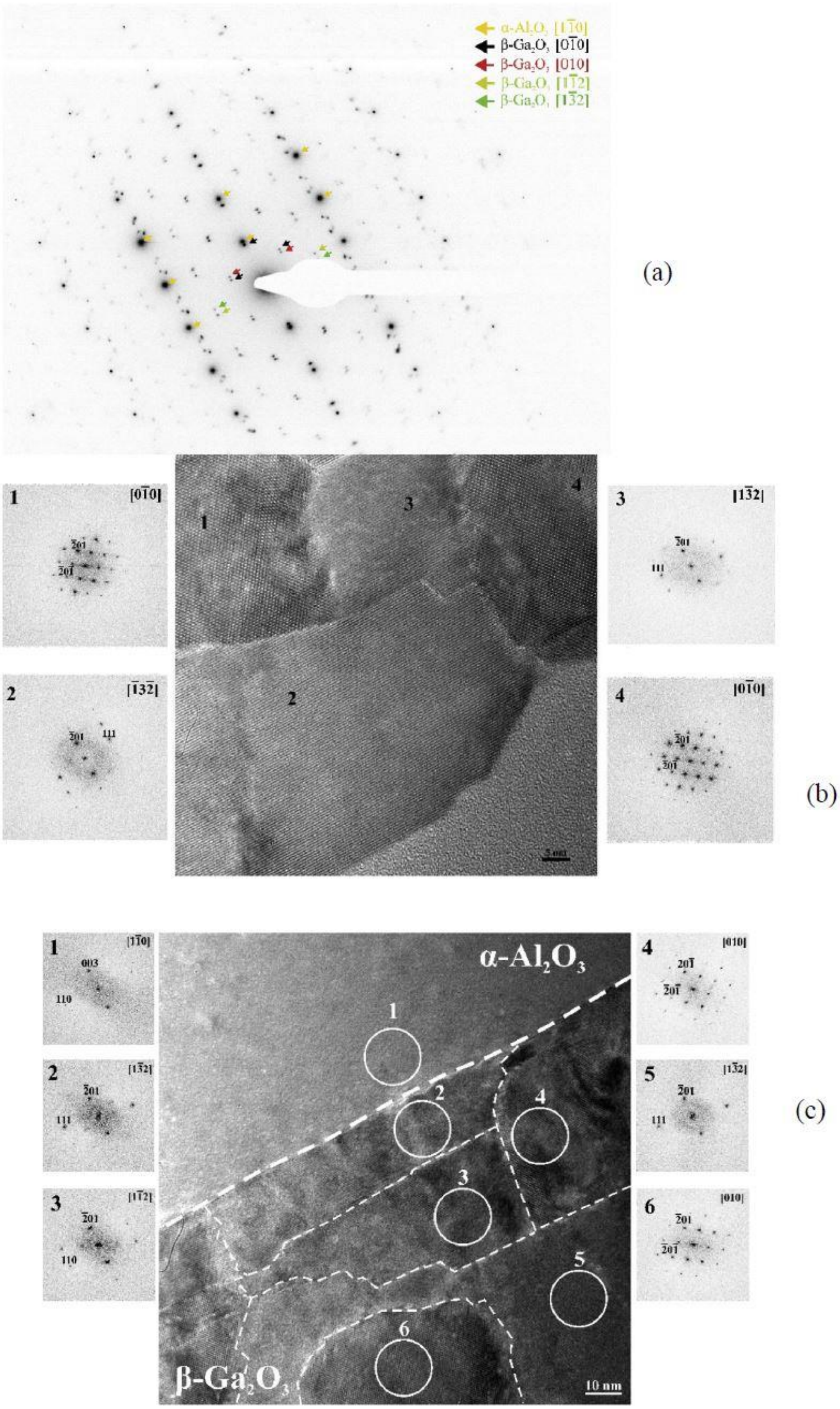

Fig. 3.7 TEM analysis of sample #146e thermally treated at 1000°C and cooled slowly; a) SAED, b) and c) HRTEM images of epitaxial β-Ga_2O_3 with the corresponding FFTs. (Reproduced from Ref.100).

Additionally, DSC analysis were performed in order to clarify the kinetics of the phase transition from the as-grown ε-Ga_2O_3 to the stable β-phase. This investigation technique allows to perform thermal analysis measuring the thermal flow difference between the studied sample and a reference specimen, while they are exposed to the same variable controlled temperature. The results are reported in Fig. 3.8, where two calorimetric curves recorded at two different heating rates of 5 and 10 K/min are shown. These curves were obtained from two separate fragments of the same very thick specimen, which provided, despite the large thickness, a little quantity of sample mass of about 1.5mg. The small sample mass, unfortunately, generated very noisy experimental data which did not allow to find the process activation energy and to carry out a detailed kinetic analysis.

As observable in Fig. 3.8, the thermal effects for lower heating rate result less evident, due to the possibility of transformation heats to thermalize with the system over extended time period. Concerning the 10 K/min curve a weak temperature effect is registered around 640°C, where the DSC endo-thermally bends down indicating an increased heat capacity. Furthermore, with the first derivative (dashed line) a value of 622°C, which identify the onset of the anticipated endothermal bend, is found. Two more exothermal effects were observed at 824°C and 891°C, respectively, and, scaling the area of the larger exothermal peak to the sample mass is possible to estimate the phase transition heat of about 70 kJ/mol. All described thermal phenomena are visible, although less pronounced, also for the 5 K/min characteristic. In this case, the measuring system thermal inertia caused a shift of the two exothermal peaks towards lower temperatures by 25K and 12K, respectively, and furthermore, unlike the 10 K/min curve, the area of the band peak at around 799°C is estimated larger than the band at 879°C. The peak position and area modifications between the two characteristics are typically due to kinetical reactions.

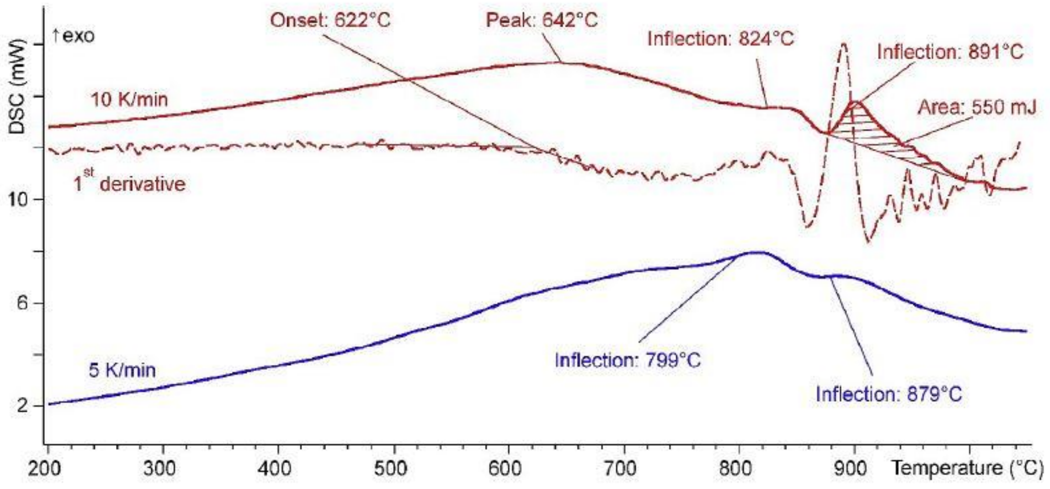

Fig. 3.8 DSC characteristics of two ε-Ga_2O_3 films grown on c-sapphire detected at 10 and 5 K/min. Dashed line represent the first derivative of 10 K/min. (Reproduced from Ref.100).

To summarize all results, it can be said that ε-phase crystal structure begins to re-organize starting from about 650°C, as shown by DSC analysis, even if no real transition can be identified by XRD measurements up to 700°C. After that temperature, a rapid lattice modification occurs, leading to apparent “amorphization” at 800°C, confirmed by the “flat” XRD patterns and by the endothermic drop after the first curves bending in both DSC profiles. The transition to β-Ga_2O_3 goes to completion when exceeding a temperature of 880°C-890°C, as confirmed by DSC, XRD and TEM measurements. Above such threshold, the transition to the stable β-phase results to be energetically favorable.

Chapter 4 - Electrical and optical characterization

The aim of the fourth chapter is to describe the electrical and optical properties of ε-Ga_2O_3 thin films obtained carrying out several different investigations. The study of these features was realized fabricating very simple resistors depositing Ohmic contact structures on square shaped specimens. The contact optimization is the starting point in order to perform electrical and photo-electrical characterization. For this reason, the multiple structures tested to find the best ohmic conditions are the first topic discussed in the following. After that, the description of the electrical investigations on Si and Sn doped samples, specifying conditions and methods of measurement applied, is presented. The achieved results are then commented in the light of EPR, ToF-SIMS and RBS investigations, given by collaborations with other research groups. Finally, reported optical and photo-electrical characterizations on undoped films demonstrate the possible use of the ε-polymorph for the realization of UV solar-blind photodetector.

In order to achieve device applications, the control of the conductivity through doping and limitation of compensating defects and trap states play a fundamental role for any semiconductor material. Being a wide bandgap semiconductor, not intentionally doped Gallium Oxide results intrinsically an insulating material at ordinary temperatures, therefore, in order to achieve conductivity properties and fabricate technological devices, doping must be provided. A large quantity of results is reported about the n-type doping of β-Ga_2O_3, which has been intensively investigated for several years. Originally, the unintentionally n-type doping behavior was attributed to oxygen vacancies inside the structure, which were supposed to be the cause of shallow donor formation[101]. This initial interpretation often derived from the observation of the correlation between β-Ga_2O_3 conductivity and the oxygen partial pressure in the growth systems[78,102]. However, this model has now been shelved considering that oxygen vacancies have been identified as deep donors (1eV)[17] and thus characterized by a very high activation energy, therefore they could not affect significantly the carrier concentration at room temperature. Instead, shallow donors in unintentionally doped β-phase samples seem to be related to the introduction of Si contamination. Indeed, all elements belonging to the group-IV (Si, Ge, Sn), suspected to generate n-type conductivity, have been theoretically and experimentally deeply investigated and, as reported in recent literature[17,103,104] they can be associated to shallow donor levels. In support to these results, in Ref.18, an ionization energy of 36.6 meV for isolated donor impurities was estimated. Calculations carried out to define the role of Si and Ge in β-Ga_2O_3 suggested a preferential occupation of tetrahedral Ga sites, while Sn prefers the octahedral Ga site coordination[17,103]. In β-polymorph, intentionally silicon and tin doping, have been carried out by ion implantation and through bulk and epitaxial growth methods[16,92,102,105–107] reaching a controllable carrier concentration up to 10^{19} cm^{-3}. Similar concentrations were also reported for the α-polymorph deposited by mist-CVD[108].

Electrical properties of β-Ga_2O_3 were further studied by Irmscher *et al.*[18], who reported temperature dependent resistivity and Hall effect measurements (Fig. 4.1a,b). Temperature dependence of the resistivity, shown in Fig. 4.1a, matches well with a moderately doped semiconductor behavior: between 30K and 130K the freeze out phenomenon takes place and a thermally activated transport in conduction band (CB) is observed, at lower temperatures impurity band conduction becomes dominant while at temperature above 130K an increasing resistivity occurs due to a decreasing mobility. The not strictly linear behavior of the resistivity values in the case of the red-colored data is probably due to a more resistive sample where the transition to a mere hopping conduction occurs at lower temperatures. This effect is also consistent with the electron concentration data where the bent of the curve is just hinted in Fig. 4.1c and moved to lower temperatures. This bent is more evident in the other samples of the same pictures, where, due to higher doping, the hopping conduction occurs at higher temperature. The low T Arrhenius plot (below ~100K) exhibits a typical piecewise linear trend. In Fig. 4.2b Hall mobility at RT results to be about 130 cm^2/Vs and reached maximum values from 280-500 cm^2/Vs at 100K. Concerning p-type conduction in beta-gallium oxide, there have been several theoretical studies[109–112],[113], however up to now there is no reported evidence of successful hole conductivity. Experimentally, a p-type conduction was observed in such polytype by Chikoidze *et al.*[114], however no further confirmations about the bulk material are reported in the literature; conversely a self-trapping of holes is rather highlighted by Varley *et al.*[109]. This agrees with the fact that the valence band in gallium oxide results practically flat and the holes are frozen. It is worth to mention that, differently, Liu *et at.* reported on p-type conductivity in beta-Ga_2O_3 nanowires due to nitrogen impurities. They evaluated nitrogen as a possible acceptor dopant, because of its lower ionization energy and ionic radius comparable to Oxygen, which could favor the substitution and relevant doping. This assumption agrees with the calculations of Zhang *et al.*[115] which found nitrogen to behave as shallow acceptor impurity. More in general, Lyons *et al.*[116], concerning the other polymorphs, found a comparable self-trapping energy for the hole, with a very low mobility, which preclude a p-type conductivity. Although a p-type conductivity was theoretically predicted, very poor results have been experimentally provided, suggesting that a real hole conduction has not yet been

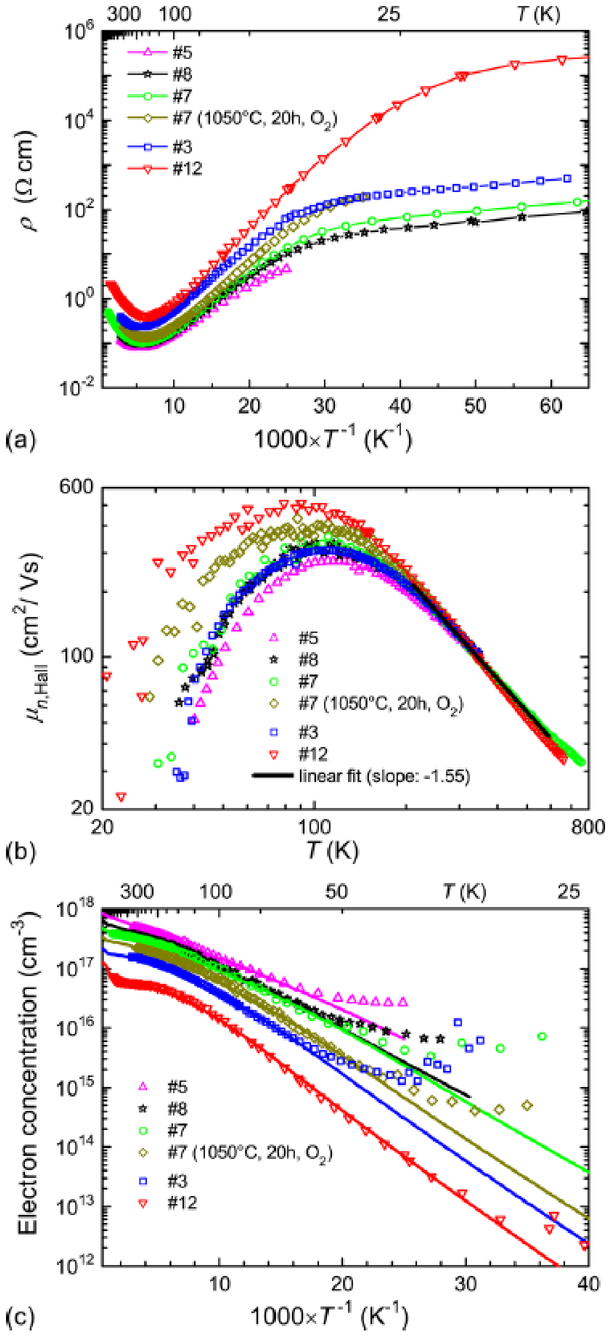

Fig. 4.1 Temperature dependent a) resistivity and b) electron Hall mobility data measured on β-Ga_2O_3 films. (Reproduced from Ref.18).

achieved and is discouraged by different recent works. Among these, Mulazzi *et al.*[56] calculations revealed a completely flat valence band and a high negative effective mass suggesting the presence of frozen holes. Dong *et al.*[111] performed first-principles calculations using DFT model to investigate the compensation mechanism as well as dopant and native defect interactions in nitrogen doped β-phase concluding, that that N dopant acts as deep acceptor and could not effectively dope p-type.

4.1 Ohmic contacts to ε-Ga_2O_3

The characterization of wide bandgap semiconductors and the realization of high quality devices strongly depend on the choice and the features of metal contacts. Despite several methods adopted, ideal ohmic contacts are hardly reproducible on gallium oxide, due to a significant influence of electrode quality and surface morphology. Ohmic contact performances are usually described using an important parameter such as the specific contact resistance, expressed in Ω cm^2 and independent of the contact geometry. The development of low specific contact resistance is essential to avoid overheating issues during current flow in device operation as well as slowdown of device switching speed. Typically, wide bandgap materials exhibit a high barrier at metal/semiconductor interface[117,118]. Generally, in undoped samples, the barrier is high enough to hinder the carrier transport. In order to reduce the potential barrier and obtain the desired conduction, local (below the contact area) heavy doping or elevate RTA temperature are applied to enhance electron tunneling or thermally activated barrier jump, respectively. Depending on the effective doping concentration and/or temperature, three different transport mechanisms can occur across the barrier: transport controlled by (i) field-effect (FE), which appears at lower temperature and is characterized by a predominant tunneling of the carriers, by (ii) thermionic field effect (TFE) that comes out at higher temperature and it is operative in a doping range of 10^{16}-10^{18} cm^{-3}; in this case both tunneling transport and thermal emission over the barrier are evident. (iii) Finally, the thermionic effect (TE), where current transport occurs only by thermionic emission over the potential barrier, is the third mechanism of charge transport through the contact barrier. If a metal is used, another important parameter to achieve ohmic contacts is the metal work function, which has to be similar or smaller than semiconductor electron affinity (4 eV for n-type β-Ga_2O_3)[119].

Pearton *et al.*[28] reported, in a detailed review, the metals/alloys that exhibit the best performance if used as Ohmic and Schottky contacts deposited on β-Ga_2O_3. The most common bilayer contact structures are Ti/Au and Ti/Al[120–124], deposited by using different techniques. In this structure Ti represent the metal element at the interface, while Au or Al are cap layers added to protect the metal below and to reduce the contact sheet resistance. However, with the aim to further optimize the electrodes, several other complex structures and elements were tested [28] in the last few years. Furthermore, in many cases local doping by ion implantation under the contact areas and rapid thermal annealing in controlled atmospheres have been carried out to improve the contact performance.

While the contact deposition on β-polymorph was intensively investigated, a lack of information about Ohmic contact on ε-Ga_2O_3 results evident. In the following, results related to deposition and characterization of Ohmic contacts realized on ε-phase thin films are presented and discussed. This is probably the first extensive investigation about ohmic contacts on ε polymorph.

Before carrying out any characterization, film thickness and uniformity were tested on the whole deposited area; the crystalline symmetry of the lattice was verified by x-ray investigation. Layer thickness was measured by optical interferometry, detecting the reflectivity fringes through a JASCO UV-VIS V-530 spectrometer and considering the refractive index n_λ values of undoped epsilon-Ga2O3 layer at RT in the same wavelength range (reported in Appendix A). Finally, the 2 inch samples were cut in specimen of 5 x 5 mm^2, which were successively cleaned by organic solvents, in order to remove surface dust, and by selective etching with a solution of $HF:HNO_3$=50:50. The latter treatment was particularly important for Sn-doped samples to eliminate residual SnO_x from the surface, as it will be further explained, but it was applied to every sample.

In order to evaluate specific contact resistance and perform resistivity and Hall effect measurements, two different contact layouts were realized: transfer length method (TLM) and van der Pauw (vdP) configuration. Furthermore, two methods were alternatively used to deposit electrodes, i.e. thermal evaporation or sputtering.

The thermal evaporation was carried out in a homemade system, at IMEM-CNR institute .Samples are mounted onto a holder, covered by a stencil mask with the desired contact layout openings and placed inside the chamber with the ε-layer facing down at about 30 cm from two heated tungsten crucibles. The two crucibles are filled with the solid materials that must be evaporated (99,999 Au and 99,999 Ti purity). High “clean” vacuum (using pumps without oils) of 10^{-6} mbar is created. Then, crucibles are heated alternatively, up to Au and Ti boiling temperatures of about 1405°C and 1715°C for a vapor pressure of 10^{-4} mbar, respectively. The evaporation is monitored by a deposition rate and thickness controller. The deposition rate is kept at 2-3 Å/sec for titanium and from 1 to 3-4 Å/sec for Au, while thicknesses of 300 Å and 700 Å, respectively, were set. However, sometimes as a consequence of very high evaporation temperature, especially for the Ti, caused the crucibles breaking and, furthermore, a good reproducibility has never been reached.

Consequently, to avoid these problems DC and RF sputtering deposition were tested and performed at ThiFiLab of University of Parma, using several materials. In the sputtering deposition technique, the depositing material and the substrate are positioned on two parallel electrodes, facing each other. When a potential difference is applied between anode and cathode, in presence of Argon gas, a glow discharge occurs. Electrons are accelerated to the substrate (anode) by the electrical field, and, colliding with Argon neutral atoms inside the chamber, generate ions. Then, secondary electrons, emitted by the target contribute in the glow discharge creating a continuous ionization. The target on the cathode is hit by ionized elements (Ar^+), which transfers energy and momentum to the target atoms, breaking their bonds. Therefore, atoms extracted from the target surface may reach the substrate surface, generating here a thin layer. Moreover, a “reactive sputtering” could be executed by using a gas mixture with an inert (Ar) and a reactive gas (O_2), giving two ionic species in the chamber Ar^+ and O^+, which play an important role for the deposition of the desired compound. Furthermore, DC- and RF-sputtering were carried out for target of metal elements and insulating material, respectively, because when a direct current is applied for sputtering an insulating material the surface of the target charges rapidly by positive ions Ar^+, preventing a continuous discharge. Such a condition is avoided by the use of an alternating current, by decoupling the cathode (target) with a suitable capacitor. As anticipated, different materials were deposited by sputtering, in addition to the more usual bilayer Ti/Au, to achieve the best ohmic conditions. Initial attempts to get good Ti/Au contacts by sputtering were frustrated, because of the impossibility to perform a rapid thermal annealing at high temperatures (800-900°C). Unfortunately, the contacts exhibited a not linear current-voltage characteristics. Also prolonged thermal annealing at lower temperatures (below the transition T of the ε polymorph) did not provide linear I-V plots, probably due to the formation of TiO_2 interface layer. Successively, Ti/Al, AZO(Al-doped ZnO)/Ti/Au and AZO/Au contacts were tested, without improvement of the ohmic behavior, suggesting the existence of a common problem, that we identified to be formation of Al_2O_3 at the metal-Ga_2O_3 interface via Oxygen subtraction from Ga_2O_3. To avoid this inconvenient, UZO/Au and UZO/ITO (Undoped ZnO/Indium Tin Oxide (In2O3-90% doped with SnO2-10%) structures were deposited, but again non ohmic I-V curve were found for undoped ε-Ga_2O_3 samples. More recently, ITO, ZnO/ITO and ITO/Pt also exhibit non ohmic behavior. For this reason, Au and Pt were definitively excluded from the contact structures, due to their probable diffusion inside Ga_2O_3 films when heated at high temperatures. The best ohmic characteristics were obtained with a sputtering deposition of a bilayer SnO_{2-x}/ITO (See Fig. 4.2).

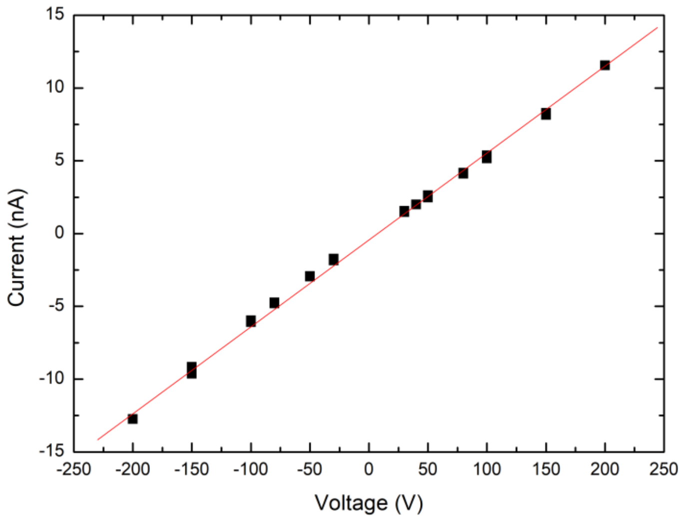

Fig. 4.2 Typical current-voltage characteristic, recorded in dark, of a ε-Ga_2O_3 film with SnO_{2-x}/ITO contacts.

It results evident, from this initial study of ohmic contact on ε-Ga_2O_3, that, compared to β-polymorph, the same contact structure behaves differently when deposited on the surface of the two polymorphs. Additional tests are required to improve electrodes functionality. In particular, the evaluation of pros and cons of an ex-situ thermal treatment is needed. Table 4.1 reports the investigated contact structures and their deposition parameters.

Sample	Deposition Technique	Contact configuration	Materials	Contact behavior
146	TE	TLM	Ti/Au	Ohmic
398 Ud I2	TE	TLM	Ti/Au	Non-Ohmic
393 Si C1	DC Sp.	vdP	ITO	Ohmic
394 SiL1	DC Sp.	vdP	ITO	Ohmic
368 Sn E4	RF-DC Sp	vdP	ITO/Pt	Non-Ohmic
369 Sn E1	RF-DC Sp	vdP	ITO/Pt	Non-Ohmic
421 Sn 2	RF-DC Sp.	vdP	ZnO/ITO	Non-Ohmic
421 Sn 3	RF-DC Sp.	TLM	ZnO/ITO	Non-Ohmic
440 Si 1	RF-DC Sp.	vdP	SnO_{2-x}/ITO	Ohmic
425 Sn-1 4a	RF-DC Sp.	vdP	SnO_{2-x}/ITO	Ohmic
421 Ud 3	RF-DC Sp.	TLM	SnO_{2-x}/ITO	Ohmic
421 Ud 4	RF-DC Sp.	TLM	SnO_{2-x}/ITO	Ohmic

Table 4.1 Electrical behavior and deposition parameters of some contact structures.

It is worth underlying that the production of the ohmic SnO_{2-x}/ITO contact was possible by applying similar conditions used to produce Sn-doping of Ga2O3 layers via diffusion, which included RF-sputtering and depositing of about 50 nm of a mixture of tin monoxide and metal tin (SnO+Sn). The sample surface outside the chamber exhibited a light brown color due to the high concentration of metal tin, which could change depending on the sputtering parameters. The SnO+Sn mixture was chosen to avoid the formation of micro droplets, using only pure tin, during the diffusion at high temperature. For this reason, a "reactive" sputtering was realized introducing oxygen to promote the tin oxidation on the target and achieve SnOx. Diffusion of the tin atoms within film was then obtained by annealing at 600°C for 4 hours. After this treatment the sample surface resulted quite transparent proving that the metallic tin penetrated the Ga_2O_3 film. Then, the SnOx residual on the film surface was removed with a chemical wet etching ($HF:HNO_3$=50:50), as mentioned above. The real penetration of the tin as dopant was investigated by electrical, ToF-SIMS measurements (discussed in the following).

4.2 Electrical characterization

In this chapter the n-type doping of ε-Ga_2O_3 is presented and described. Silicon and tin dopants were involved in this work by using two different methods to incorporate them inside the films. As anticipated, Si-doped samples were achieved directly during the MOVPE deposition, injecting a silane flow into the growth system, while Sn-doped specimens were obtained by diffusion of metal tin after RF-sputtering and annealing procedures as reported in the previous section.

The sputtered contacts were successively deposited on the corners of square samples (see Fig. 4.3), in order to carry out transport measurements by van der Pauw method: two adjacent contacts are connected to the current source and the other two to the voltmeter. This popular method allows to measure samples of irregular shape as long as the contacts are ohmic, located at the rim of the sample and very small respect the sample surface[125–127]. Actually, the theory behind the van der Pauw method is based on the assumption of point-sized contacts. If the electrode area is not negligible with respect to sample area then a correction of both resistivity and Hall coefficient data must be applied[128,129], which depends on the ratio between the sample side and the contact side. In our samples, the same ratio was maintained for all the samples, generating little uncertainties of the order of 5% and 10% for resistivity and Hall voltage, respectively[129]. Concerning the Hall effect measurements, a magnetic field of 0.8T was used and a Keithley Hall measurement setup was employed, while the electrical characterization was performed under vacuum conditions, in a temperature range from 10K to 600K, initially going down from RT to 10K and successively increasing the temperature up to 600K. After reaching a certain temperature stability, the current to apply was chosen in a range where all the I-V characteristics between couples of adjacent contacts were linear. Voltages were measured between two terminals of the square sample providing current on the other two terminals (shown in Fig. 4.4).

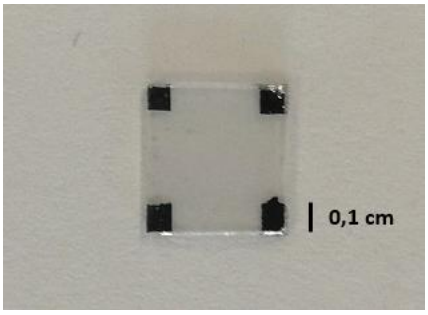

Fig. 4.3 Van der Pauw contact configuration realized on a square specimen with a 0.5 cm side.

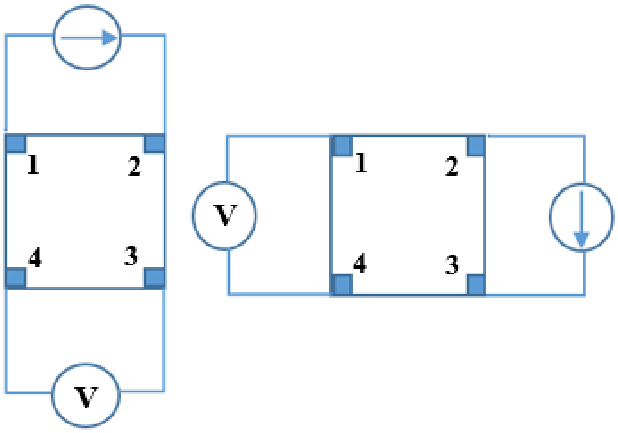

Fig. 4.4 Schematic configurations of sample connections employed for resistivity measurements.

Thus, the related pseudo-resistances can be defined: $R_{12,34} = \frac{V_4 - V_3}{I_{12}}$, $R_{23,41} = \frac{V_1 - V_4}{I_{23}}$. The van der Pauw method is based on the relation between $R_{12,34}$ and $R_{23,41}$ expressed by:

$$\exp\left(-\frac{\pi d}{\rho} R_{12,34}\right) + \exp\left(-\frac{\pi d}{\rho} R_{23,41}\right) = 1 \tag{4.1}$$

where d represents the thickness of the film and ρ the material resistivity. Knowing the thickness and the pseudo-resistances, from the (4.1) it results immediate to estimate the ρ value. Then, the solution may be written as follows:

$$\rho = \frac{\pi d}{ln2}\frac{R_{12,34} + R_{23,41}}{2} f(\frac{R_{12,34}}{R_{23,41}}) \tag{4.2}$$

where f is defined the van der Pauw function and depends only by the ratio $\frac{R_{12,34}}{R_{23,41}}$ as is observable in Fig. 4.5. This relation between the f factor and the ratio $\frac{R_{12,34}}{R_{23,41}}$ is defined:

$$\cosh\left[\frac{\left(\frac{R_{12,34}}{R_{23,41}}\right) - 1}{\left(\frac{R_{12,34}}{R_{23,41}}\right) + 1}\frac{ln2}{f}\right] = \frac{1}{2}\exp\left(\frac{ln2}{f}\right) \tag{4.3}$$

Consequently, the resistivity value is obtained from (4.2) equation, calculating the resistance ratio and finding the f parameter from Fig. 4.5.

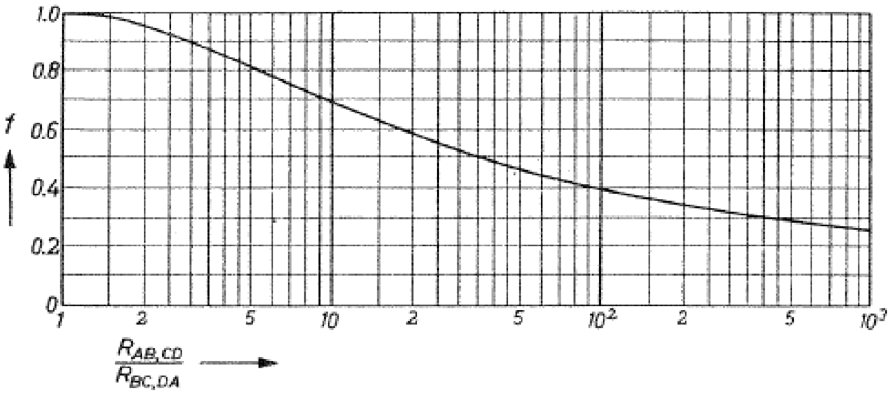

Fig. 4.5 Characteristic curve of the geometric factors. (Reproduced from Ref.125).

Fig. 4.5 shows that the more resistance ratio deviates from unity the more the sample deviates from perfect square shape and f decreases well below 1. After completing the first combination, current is reversed for total 8 measurement combinations to be finally averaged (ρ_{avg}).

On the other hand, Hall effect measurements provided also several information, which may be derived from the Hall voltage, such as the conductivity type, the carrier density, and, considering also the resistivity, the mobility. Applying a magnetic field perpendicular to the sample surface, the Hall voltage is detected employing the configurations presented in Fig. 4.6.

In this case, current source is positioned between two opposite contacts and voltages are measured on the other opposite two. Eight Hall voltage values are registered reversing the current directions and inverting the magnetic field (positive and negative), in order to eliminate offsets.

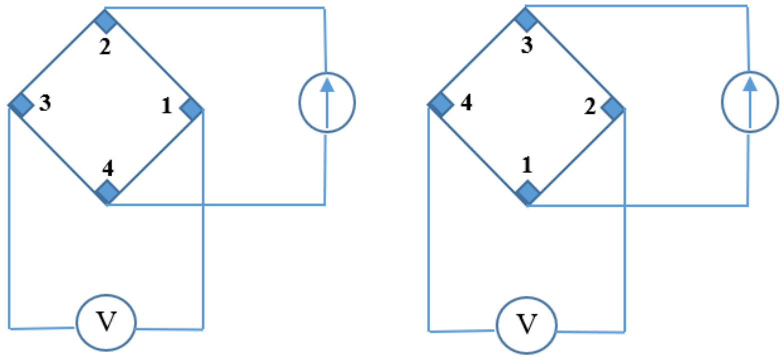

Fig. 4.6 Schematic illustration of sample connections involved in Hall voltage measurements.

Thus, Hall coefficient R_H, calculated in cm^3/C were determined by:

$$R_H = \frac{d}{B}\Delta R_{13,24} \tag{4.4}$$

The provided eight Hall voltages allowed to achieve the two Hall coefficients R_{HC} and R_{HD}, then averaged obtaining:

$$R_{Havg} = \frac{R_{HC} + R_{HD}}{2} \tag{4.5}$$

and, consequently, Hall mobility can be calculated trough the expressions:

$$\mu_H = \frac{|R_{Havg}|}{\rho_{avg}} \tag{4.6}$$

Furthermore, it is important to note that negative or positive Hall coefficients are related to n-type or p-type material respectively. The carrier concentration n in a n-type semiconductor can be estimated by:

$$n = \frac{1}{|e^- \times R_{Havg}|} \tag{4.10}$$

in which e^- is the electron charge.

The Hall coefficient sign of the investigated samples resulted negative and thus identify a n-type doping. Considering that silicon and tin are demonstrated to be donors in β-polymorph, the same behavior could be expected in ε-Ga_2O_3. Additionally, a previous ARPES study on Si-doped thin films detected a Fermi level (FL) positioned about 0.2 eV below the CBM and a really flat valence band[56], in agreement with theoretical predictions[56], which supports the idea of large hole effective mass and extremely low mobility, which ultimately does not provide any hole conductivity. All these results support the hypothesis of n-type doping, induced by Si and Sn impurities in ε-phase films. The most representative data, related to silicon and tin doped samples, are shown in Fig. 4.7 and Fig. 4.8, where the curves are reported in an Arrhenius plot and in a "Mott plot" (here defined as the plot of ln(ρ) vs $T^{-1/4}$), respectively. With respect to the resistivity measurements reported in Fig. 4.1(a), carried out on β-Ga_2O_3[18], in this case the Arrhenius plot exhibits a continuous variable slope, whereas an evident linear behavior is observed in Fig. 4.8, suggesting a transport mechanism based on the variable range hopping (VRH), described by the Mott law. Mott demonstrated that the behavior of the temperature-dependent resistivity $\rho(T)$, at low temperatures and can be expressed as follows:

$$\rho = \rho_0 \exp\left[\left(\frac{T_0}{T}\right)^{\frac{1}{4}}\right] \tag{4.11}$$

where ρ_0 identify the resistivity at infinite temperature and T_0 depends on the state localization radius ξ=1/α and on the density of states near the Fermi level $g(\varepsilon_F)$, assumed constant (for non-interacting electron gas):

$$T_0 = \frac{C}{K_B g(\varepsilon_F)\xi^3} \tag{4.12}$$

In (4.12) K_B refers to the Boltzmann constant and $C = \frac{8^3}{9\pi}$ ≈18.1 represents a dimensionless proportionality constant which depends on the hopping sites configuration in the model[130]. Such a behavior is indicative of a hopping transport mechanism, in which sites having energy levels around the Fermi level are involved.

The relation (4.11) can be rearranges as: $\ln(\rho) = \ln(\rho_0) + \left[\left(\frac{1}{T}\right)^{\frac{1}{4}} * (T_0)^{\frac{1}{4}}\right]$, so that a linear trend is obtained in a "Mott plot", where $(T_0)^{\frac{1}{4}}$ identifies the slope of the curves. This analysis is applied in Fig. 4.7

The electrical data at room temperature (RT) and the general parameters are presented in Table 4.2. It can be noted that in some samples the Hall voltage, and consequently the Hall mobility and coefficient, were not measurable. When detectable, the Hall mobility presents values of few cm^2/Vs and the carrier concentration related to the Hall coefficients resulted of the order of 10^{17}-10^{18} cm^{-3}.

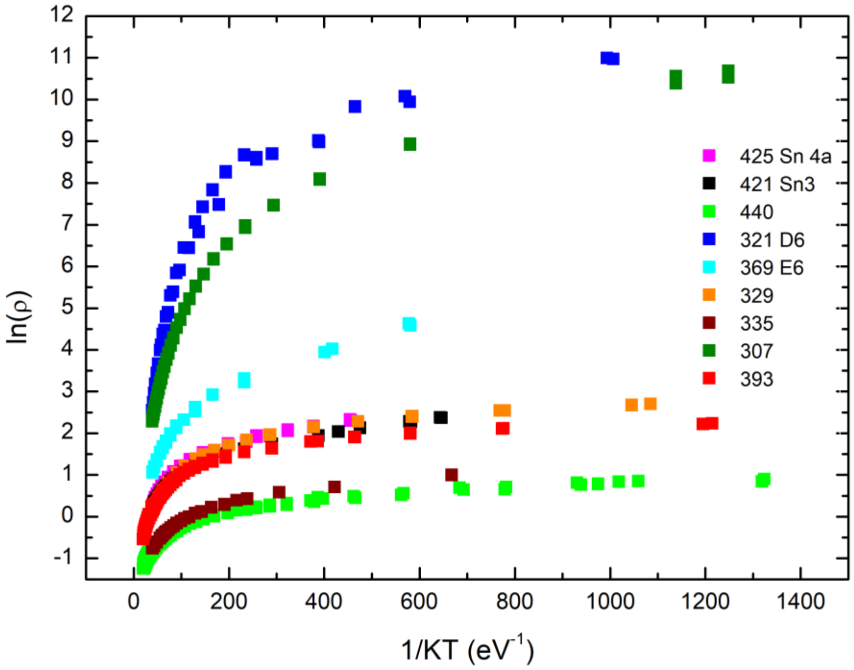

Fig. 4.7 Arrhenius plot of Si and Sn doped samples. Natural logarithm of the resistivity data vs 1/KT.

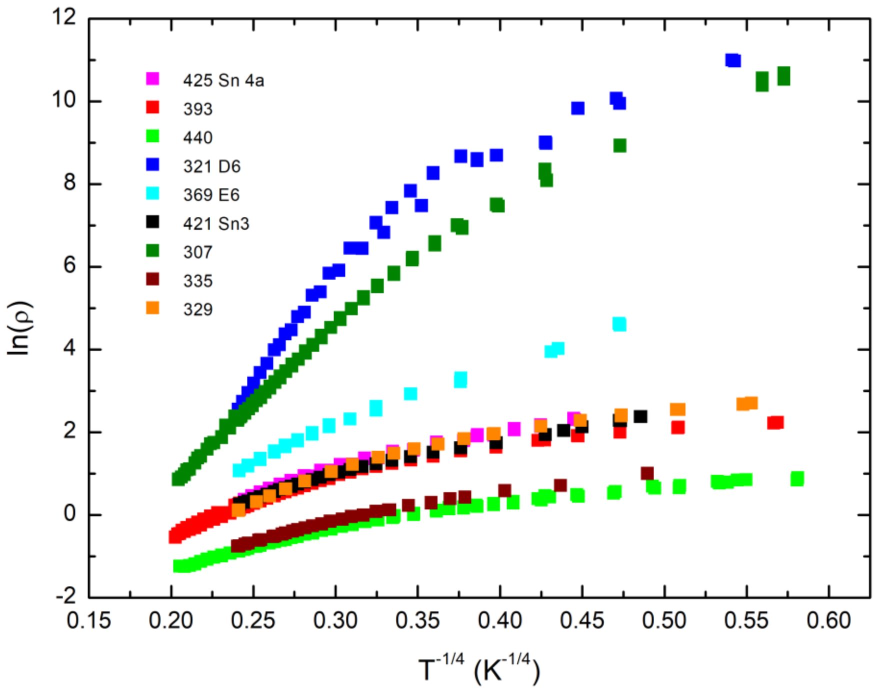

Fig. 4.8 Mott plot of Si and Sn doped samples. Natural logarithm of the resistivity data vs (T)$^{-1/4}$.

Sample (#)	MOCVD Growth T (°C)	Doping method	Silane flux (sccm)	Post-sputtering annealing time (min)	Thickness (nm)	RT resistivity (Ωcm)	RT Hall mobility (cm^2/Vs)	RT Hall density (cm^{-3})
425 Sn4a	610	Sn-diffusion	-	120	6000	1.28	NM	NM
393	610	Si-MOCVD	0.005	-	1100	1.1	1.8	3.00 x 10^{18}
440	610	Si-MOCVD	0.005	-	700	0.4	4.36	3.42 x 10^{18}
321 D6	600	Sn-diffusion	-	120	310	12.8	2.4	2.00 x 10^{17}
369 E6	610	Sn-diffusion	-	240	300	2.1	NM	NM
421 Sn3	610	Sn-diffusion	-	240	300	3.6	NM	NM
307	600	Si-MOCVD	0.005*	-	1000	9.8	NM	NM
335	610	Si-MOCVD	0.005*	-	460	0.47	4.5	2.90 x 10^{18}
329	600	Si-MOCVD	0.005*	-	560	1.6	1.6	2.40 x 10^{18}

Table 4.2 Room temperature electrical results and main parameters of some investigated samples.

A carrier localization can occur in conditions of disorder, due to random impurity distributions but also potential fluctuations due to lattice defects, also for low impurity densities. In these conditions, Mott supposed that at low temperatures only electrons frozen on localized states that have energies within a small band near the Fermi level (optimal energy) participate to transport, and therefore, a hopping conduction between these states could be observed, instead of an electron conduction in the CB. The electron faculty to leave the occupied site in order to fill an empty one depends on the proximity, in energy, between the two sites (see Fig 4.9). This "hopping" process from a site i to a site j, with related energies ε_i and ε_j and localized wave functions φ_i and φ_j, corresponds to a tunneling effect assisted by phonons, which provide the energy difference ($w_{ij} = \varepsilon_j - \varepsilon_i$) between the final and the starting state.

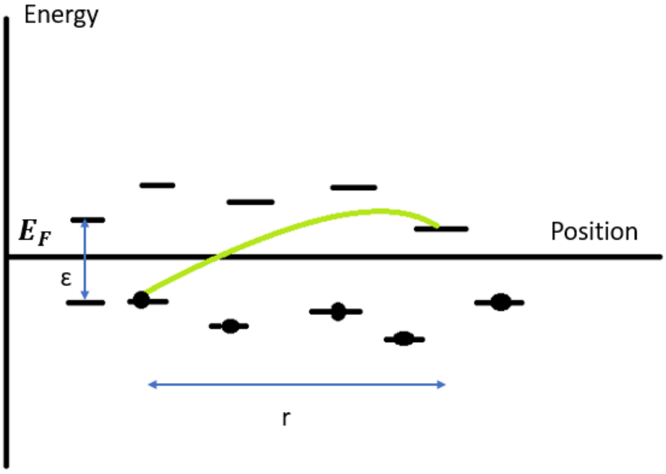

Fig. 4.9 Model of hopping process between localized states.

The process probability per time unit can be expressed by

$$v_{ij} \propto \exp\left(-2\alpha R_{ij} - \frac{w_{ij}}{KT}\right) \tag{4.13}$$

where R_{ij} represents the distance between the two sites, while 1/α is a constant parameter independent of the site, denominated localization length. Consequently, when v_{ij} reaches its maximum, thus with a minimum value of the exponential argument, the biggest contribute to the conductivity is achieved. This occurs at sufficiently low temperature, or also at high temperature but in presence of high disorder (which enhances the energy level fluctuations, then also the possible w_{ij} energy separation), when the factor $\frac{w_{ij}}{KT}$ is not negligible compared to $2\alpha R_{ij}$, promoting a VRH transport. In this case, R_{ij} and w_{ij} refer to optimal length and optimal energy, respectively, and are both temperature-dependent. The number of sites N_{ij} in a unit volume may be written as

$$N_{ij} = g(\varepsilon_F) w_{ij} = \frac{1}{\left(\frac{4}{3}\right)\pi R_{ij}^3} \tag{4.14}$$

where $g(\varepsilon_F)$ represents the density of localized states at the Fermi level. Practically, in a reference volume, the number of sites separated by a distance R_{ij} equals the number of energy states in the optimal band w_{ij}, equal to the product $g(\varepsilon_F)w_{ij}$. Substituting the (4.12) in (4.11) and minimizing the exponential argument, the optimal hopping length can be found:

$$R_{opt} = \frac{3}{8\alpha}\left(\frac{T_0}{T}\right)^{\frac{1}{4}} \tag{4.15}$$

and then the optimal energy is extracted by substituting the relation (4.13) into the last hopping probability relation obtained finding:

$$w_{opt} = \frac{K_B T}{4}\left(\frac{T}{T_0}\right)^{\frac{1}{4}} = \frac{K_B T^{3/4}}{4} \times slope \tag{4.16}$$

Specifically, in VRH the quantity R_{opt} and w_{opt} identify respectively the average distance between localized states in the temperature-dependent optimal band in proximity of the FL, and the activation energy necessary to thermally stimulate the jumps. This energy corresponds to the bandwidth around the Fermi level where the localized states involved in the hopping process lie and can be extrapolated from (4.16) equation containing the slope values obtained from the Mott plot of the data.

Thus, as shown in Fig. 4.7 and 4.8, all investigated Si and Sn doped ε-Ga_2O_3 thin films are characterized by a transport mechanism which follows the Mott theory. For this reason, the Arrhenius plot reported in Fig. 4.7 cannot be fitted by any straight line, while the characteristics in Fig. 4.8 exhibit two clear consecutive slopes corresponding, probably, due to two different defects which take part to separate hopping processes activated in two distinct temperature ranges. Fig. 4.10 shows, in particular, the two transport regimes of two selected samples and their related fits. It is interesting to note that lower resistivity samples are characterized by lower slopes, self-consistently. The investigated samples #307 and #440 are, respectively, very resistive and very conductive, as reported in Table 4.2. Analyzing the two temperature-dependent regimes, two different slopes for each sample were extrapolated from the fits. Sample #307 provided slopes of 19 ± 0.2 $K^{1/4}$ for the low temperature range and 39.2 ± 0.1 $K^{1/4}$ for the high temperatures. In the case of sample #440 the slopes resulted of 3.5 ± 0.1 $K^{1/4}$ for the HT and 11.7 ± 0.5 $K^{1/4}$ for the LT. Considering a localization radius of the order of the nanometers [131], the density of sites of the #307 and #440 films, extracted by the equation (4.14), results about 10^{17}-10^{18} cm^{-3} (LT-HT regimes) and 10^{19}-10^{20} cm^{-3}(LT-HT regimes), respectively. The density of sites obtained from a "Mott plot" in a VRH transport identifies the concentration of the localized states involved in the hopping process and could be well compares with the RT Hall density, which is instead related to the net donor concentration. Unfortunately for the sample #307 (and a few others), the Hall density was not measurable; however, this comparison was possible for most of the investigated samples. Considering that in order hopping to take place the density of the available states needs to be higher than the carrier concentration. It is thus reasonable to obtain a RT Hall density slightly lower than the localized site densities, as effectively observed. This was also the case of sample #440, shown in Fig. 4.10.

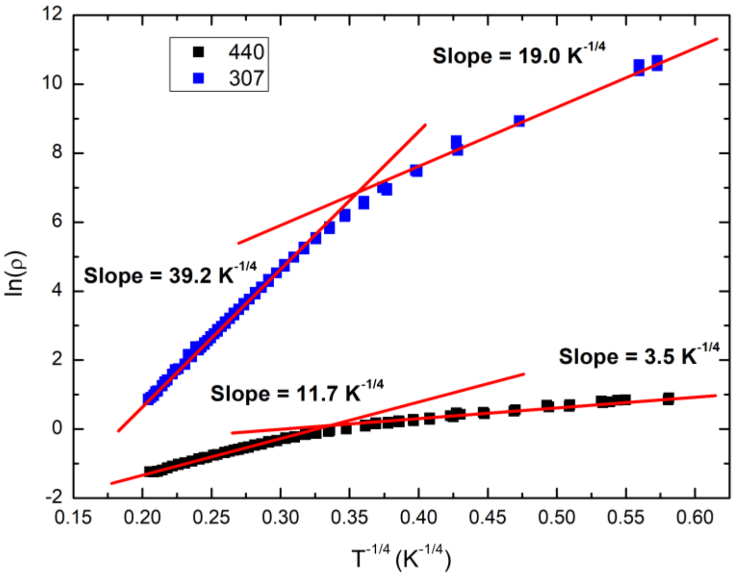

Fig. 4.10 Mott plots of sample #307 and #440 and linear fits of the data using eq. (4.11) with a slope of $(T_0)^{\frac{1}{4}}$.

The presented double slopes, analyzing data with a Mott plot, is due to different hopping mechanisms involving silicon and tin impurities. It would be appropriate to consider also the possibility of the complex defect formation with a different energy with respect to the energy of Si or Sn on Ga sites, although EPR investigation, discussed below, highlighted for Si a behavior like a hydrogenic impurity in Ga tetrahedral sites. However, complex defects and structural disorder may introduce deeper energy states, as already seen in previous investigations[56]. The nature and behavior of deep levels certainly lying into the energy gap will be described in detail in the next chapter. New light on this behavior has been shed by the comparison of these data with the results of EPR investigation, which will be discussed in the following.

A result consistent with the transport mechanism which involves localized states in this narrow band near the FL, instead of a free carrier conduction, is provided by ARPES measurements carried out on some samples presented in Table 4.2. In fact, this recent work suggests that at RT the conduction band is not populated and the Fermi level is positioned about 0.2 eV below the CB. Furthermore, in variable range hopping process, compensation effects have to be taken into account. The acceptors, together with a high point defect density, may contribute to these effects acting as electron traps so increasing the empty donor concentration. Therefore, this compensation phenomenon caused by defect-related deep levels, justifies the observed lower Hall density compared to localized site concentration.

4.3 ToF-SIMS, RBS and EPR investigations

ToF-SIMS, RBS and EPR spectroscopy investigations were performed by partner institutions in order to support and confirm the described transport model and, in particular, the origin of the two different transport regimes, the defects nature, the impurities incorporation and the compensation effects. The results of these investigations were reported in Refs.132,133, and other will be object of further publications.

Although these measurements were not direct part of the present doctoral work, it was decided to briefly outline them to give the reader a more complete picture of the doping and transport mechanisms in ε-Ga_2O_3.

Time of Flight-Secondary Ion Mass Spectroscopy (ToF-SIMS) was carried out at IMM-CNR, Milan, to detect the effective penetration and incorporation of silicon and tin impurities. A dual beam ION-TOF IV (ION-TOF GmbH) was used to analyze different size areas, using Cs^+ ions and Ga^+ ions with respective energies of 2 keV and 25 keV. A sputtering time of 5 seconds was applied with intervals of 200 ms of pausing time between sputtering and the related analysis. More details on the instrumentation and the proceedings are described in Ref.134. It is important to highlight that the obtained ToF-SIMS depth profiles can provide only information about the presence and uniformity of the introduced impurities, while unfortunately a quantitative analysis of related chemical concentration cannot be achieved. The Fig. 4.11 (a) and (b) show Si and Sn profiles of two doped samples. In the case of the Si-doped sample, the Si and SiO_2 secondary ions were detected, with the latter ion dominating with respect to the elemental Si, due to the presence of oxide in the matrix (Ga_2O_3) of the films. In proximity of the interface between the film and the sapphire substrate a slight peak appears, which may be interpreted as an artefact caused by a sudden chemical matrix change. However, it can be said that a quite homogeneous Si incorporation occurred in the whole film thickness, as expected by the in situ doping by silane during the entire growth. The Sn-doped film on the other hand is characterized by a typical exponential diffusion profile, as shown in Fig. 4.11b. Furthermore, a second artefact represented by a little bump near the interface between the ε-Ga_2O_3 and the SnO_x overlayer appears.

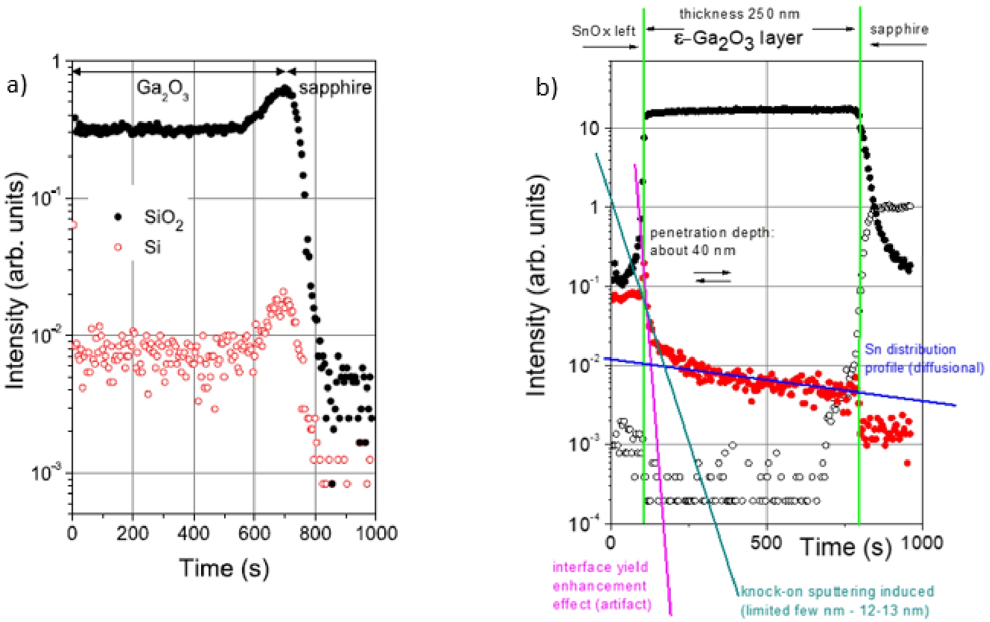

Fig. 4.11 ToF-SIMS profiles of a) Si and SiO2 secondary ions (sample #329)[132] and b) Sn (red full circles), Ga-O (black full circles) and Al-O (black open circles) related species (sample #421).

Additional Rutherford backscattering (RBS) measurements were carried out at the Institute for Technical Physics and Materials Science, Hungarian Academy of Sciences, Budapest, on Sn diffused samples to further prove the tin penetration in the gallium oxide layer. The Figs. 4.12 (a) and (b) present the spectra recorded at different tilt angles (7° and 60°) and the parallel simulations performed with the RBX code, assuming similar layer structures for both tilt angles. There is good agreement between measured and calculated data. These experiments essentially say that the SnOx layer after annealing exhibits a decreasing Sn content between uppermost surface and layer/substrate interface, consistent with a loss of Sn atoms diffused into Ga_2O_3. A continuous SnO_x layer can be observed on top, while getting down an interfacial thin mixed structure is detected with both Ga- and Sn-oxide. It is indeed difficult to identify a net interface, although pure gallium oxide film with a well-defined thickness is also clearly observed. It is worth to note that the layer thicknesses in *nm* corresponds to approximate values considering they are recalculated in atoms/cm^2 using the density of stoichiometric SnO_2 and Ga_2O_3. With these results a successful Sn diffusion into the epilayers can be confirmed.

- 60 nm $Sn_1O_{2.6}$
- 12 nm $Sn_{0.5}$ $Ga_{0.5}O_2$
- 12nm $Sn_{0.17}$ $Ga_{0.83}O_2$
- 520 nm Ga_2O_3

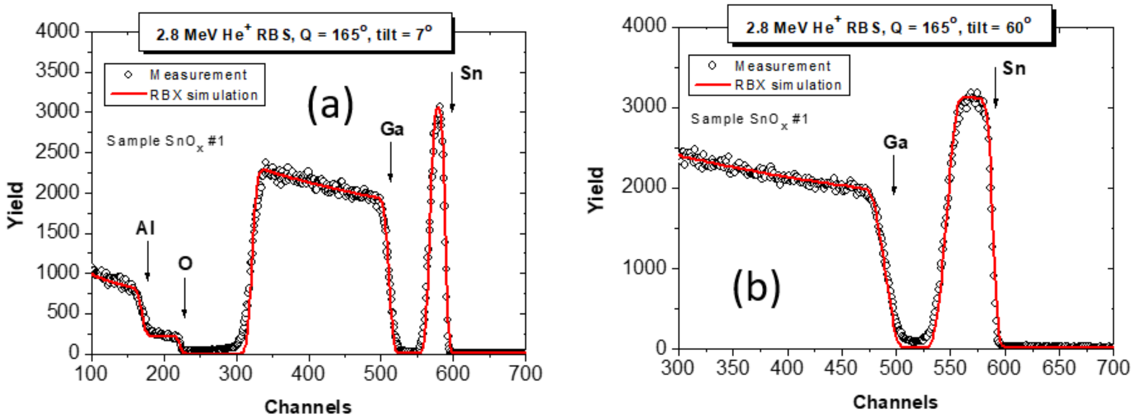

Fig. 4.12 2 MeV He$^+$ RBS spectra taken at sample tilt angle of 7° (a) and 60° (b). The arrows indicate the spectrum edges for different components.

The preferential position occupied by dopants in ε-Ga_2O_3 is an information necessary to fully understand the electronic properties and transport mechanism. In β-Ga_2O_3 Ga sites are characterized by octahedral and tetrahedral coordination and, as already known[17,70,103], the Si impurities tend to occupy tetrahedral Ga sites. In the ε-phase, instead, considering a more complex crystal structure with three non-equivalent Ga sites[33], among which two have octahedral symmetry and one is tetrahedrally coordinated, the incorporation on the preferential lattice site by the impurities and the related properties is more complicated. Very recent EPR investigations were performed by cooperating partners at Institut des Nanosciences de Paris (INSP) Sorbonne Université on some of the Si-doped samples presented above, to clarify the donor behavior and to determine the defect density[133]. The measurements were carried out in an increasing temperature range from 4K to RT. All the spin Hamiltonian parameters were found analyzing EPR spectra and applying a magnetic field rotation in three orthogonal lattice planes.

The EPR spectra, related to #335 sample, are shown in Fig. 4.13 and represent the signal of a spin S=1/2 center. This is consistent either with electrons bound to donors, and free electrons. An average concentration of 2.1×10^{18} cm^{-3} spins were obtained considering a homogeneity in defect distribution, a value consistent with the results of ToF-SIMS investigation. This value well compares also with the carrier concentration given by RT Hall effect measurements (i.e.

2.90×10^{18} cm^{-3}), demonstrating a direct relation between the paramagnetic defect and the n-type conductivity.

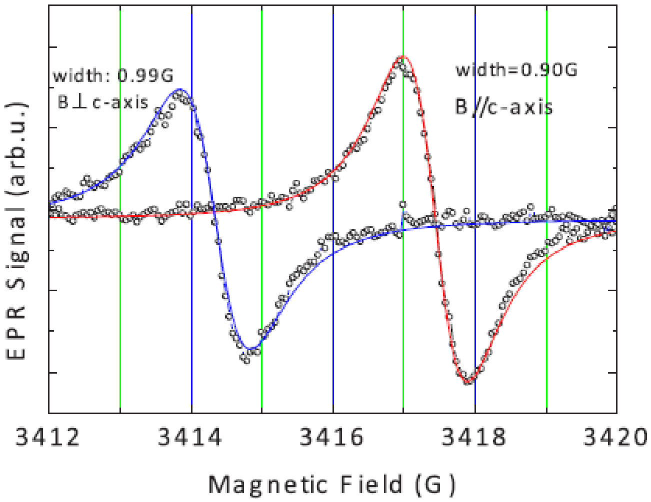

Fig. 4.13 EPR data obtained at RT (circle) and simulations with a Lorentzian line shape for the B//c (red) axis and B⊥c axis (blue). (Reproduced from Ref.133).

The isotropic *g* tensor, related to the donor, resulted weakly dependent on the temperature and is estimated to be about 1.96, for both the orientation of the magnetic field B//c and B⊥c, obtained from EPR measurements carried out in different lattice directions. Furthermore, the almost identical *g* factor in the whole range of temperatures denote that the paramagnetic Si donor is effective-mass like. On the other hand, the EPR signal intensity and linewidth exhibited a strong temperature dependence, as shown in Fig. 4.14 (a,b,c). The T-variation of these quantities resulted different in different temperature ranges, each connected to a specific transport regime. Two temperature regions are evident, especially in the EPR signal intensity plot (Fig. 4.14b and its inverse), from 295K to 100K and for T<50K. Considering a similar *g* tensor for conduction electrons and shallow effective mass donors[135], a useful method to distinguish the regimes is provided by the different susceptibility. For T>100K a Paul-like susceptibility is observed, characterized by ionized donors and electron transport in conduction band while localized electrons on Si impurities are detected for T<50K. Further information on the conduction mechanism was achieved by the linewidth ΔB_{pp} at low temperature (see Fig. 4.15), where an impurity band conduction dominates, and a VRH transport mechanism is observable in two different regimes related to two temperature ranges, confirming the electrical measurement results. In particular, equal slopes in the *Mott plot* of resistivity and EPR linewidth are observed.

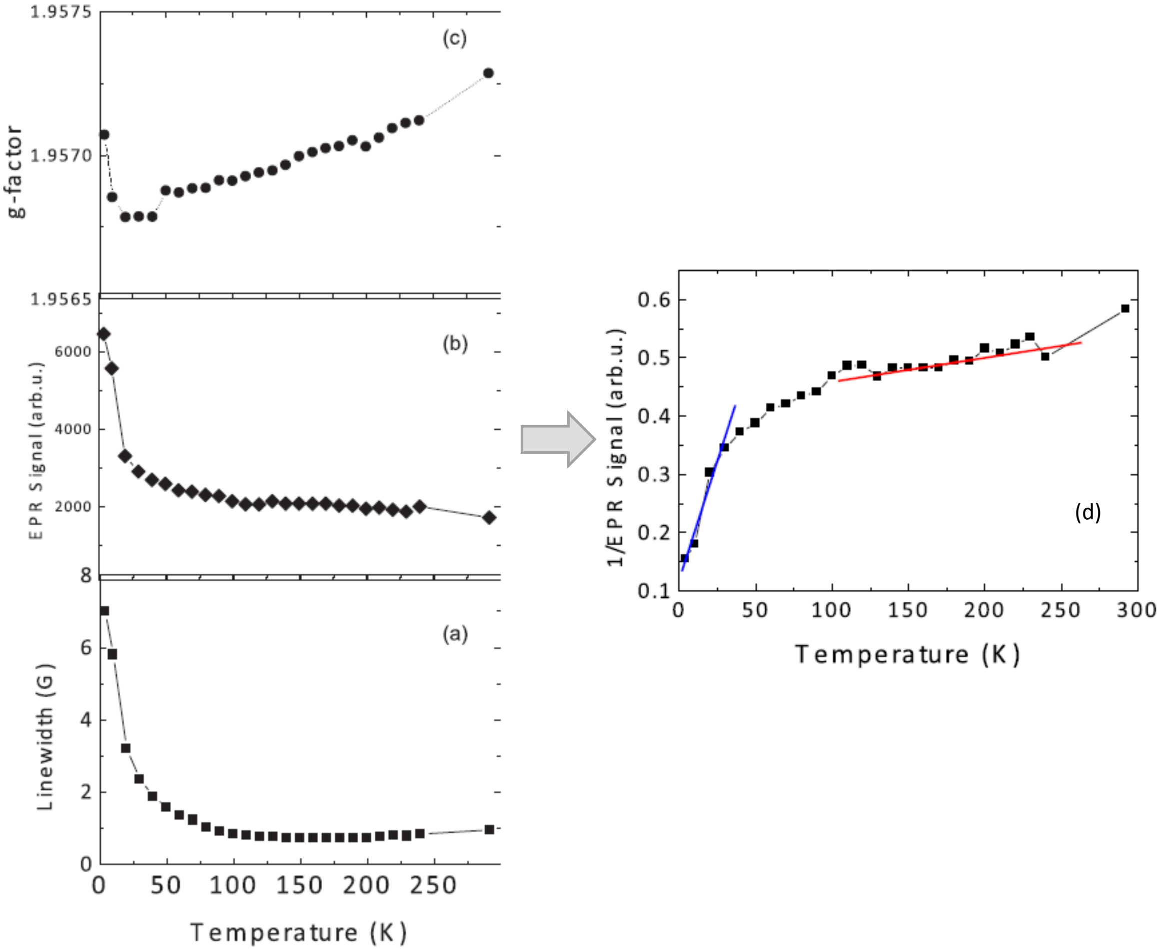

Fig. 4.14 Temperature dependent a) EPR linewidth in a range from RT to 4K, b) EPR signal intensity and c) effective *g* tensor for B//c axis. d) inverse EPR signal intensity and related fits. (Reproduced from Ref.133).

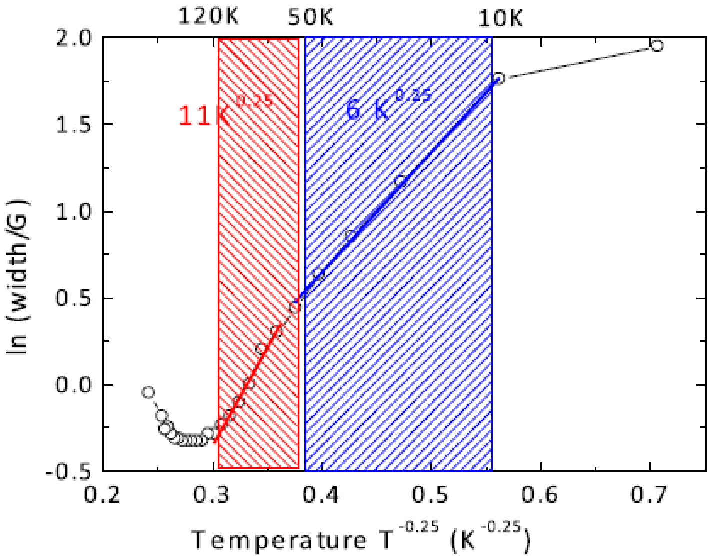

Fig. 4.15 EPR linewidth data and related fitting in two different temperature ranges describing two VRH processes. (Reproduced from Ref.133).

However, by increasing further the temperature, the Lorentzian line shape of the EPR spectra and a small peak-to-peak linewidth of ΔB_{pp}=1.0 G indicate an electron delocalization (see Fig. 4.13), whereas in the electrical investigation again a VRH transport is detected. In order to reconcile this discrepancy and provide an explanation of the double VRH conduction mechanism, the dopant clustering model is introduced. The donor-cluster formation has been hypothesized in heavily doped semiconductors and strongly depends on the doping concentration[136]. In our samples, whereas at low temperatures the VRH conduction can be attributed to electrons that hop between isolated Si donors, it is possible to suppose that, by increasing enough the temperature, electrons become delocalized into donor-clusters and a VRH conduction between these clusters could be thermally activated following the percolation theory[130,137]. Then, because EPR is sensitive to the delocalization of the electron wavelength, this technique detects such electrons as free, in extended states, but such a delocalization is limited to a donor-cluster, not to the whole crystal.

Such a VRH process between donor clusters has never been found in others gallium oxide polymorphs; in the ε-Ga_2O_3 it may be favored by a non-random dopant disposition due to the placement of the tetrahedral Ga sites only in alternate planes orthogonal to the c-axis. EPR detected a single paramagnetic defect that, considering also the theoretical results by Lany *et al.*[103], may be ascribed to Si on tetrahedral Ga sites. It is also suggested that Si behaves as a shallow effective-mass donor. As no other paramagnetic defects related to silicon impurities were detected by EPR, one can conclude that the substitution of Si onto the two octahedral Ga sites is negligible.

Through the analysis of the temperature dependence of the EPR linewidth, an activation energy related to the donor is estimated. From the Arrhenius plot of these data, an activation energy value of 6 meV is found.

4.4 Optical, electrical and photoelectrical properties of undoped films

As anticipated, improved metal contacts are necessary in electronic devices and for this reason it is useful to determine the contact resistivity, which plays an important role in electrical and optical characterization. The van der Pauw measurements allow to detect the material sheet resistance, using a 4-point technique, so excluding contact resistance effects. However, through the Transfer Length Method (TLM)[138] it is possible to extract sheet and specific contact resistance analyzing the measured *I-V* characteristics and, furthermore, to achieve activation energy value involving temperature dependent investigations. This method has not be mistakenly exchanged with the Transmission Line Model[138–142], also abbreviated as TLM, which is characterized by different measurement configuration.

Originally reported by Shockley[142], the TLM model is characterized by a pattern of aligned contacts of length L and width Z and unequally spaced by the distances d_i (see Fig. 4.17). The specimen width is instead indicated by W, assuming that the difference between the contact and the sample width should be as small as possible ($\delta = |W - Z| \ll Z$). The total resistance R_T between two metal electrodes contains the contribution of contact resistance, i.e. $R_T = 2R_m + 2R_C + R_{sh}$, where R_m refers to the contact material resistance, R_C is the resistance at the metal/semiconductor interface and R_{sh} represents the semiconductor sheet resistance. Together $2R_m + 2R_C$ provide the overall contact resistance, however in most cases a situation of $R_m \ll R_C$ occurs and then the resistance related to the contact metal R_m can be neglected in comparison with the R_C contribution. Then the specific contact resistivity ρ_C is related to the contact resistance by the relation $R_C = \frac{\rho_C}{W \cdot L_T}$, where L_T is the transfer length under the contacts and the product $W \cdot L_T$ represents the area over which the contact resistance is calculated. The transfer length L_T may be well defined as the distance traveled by carriers (electrons in this case) below the electrodes before they flow from the semiconductor into the metal, and could be formalized as

$$L_T = \sqrt{\frac{\rho_C}{R_{sh}}} \tag{4.17}$$

Fig. 4.16 shows the schematic representation of the transfer length and the path of least resistance chosen by the current when it flows from the semiconductor to the contact. Considering the specific contact resistivity ρ_C and the film sheet resistance R_{sh}, the potential distribution under the electrode can be expressed by:

$$V(x) = \frac{I\sqrt{R_{sh}\rho_C}}{Z} \frac{\cosh\left[\frac{L-x}{L_T}\right]}{\sinh\left(\frac{L}{L_T}\right)} \tag{4.18}$$

where I is the current flowing into the contact. In proximity the contact edge (x=0), the voltage reaches the highest value while it drops exponentially leaving the edge to $1/e$ of its value. The related current also drops down moving from the edge causing a phenomenon known as current crowding which follows the relation: $I(x) \propto \exp\left(-\frac{x}{L_T}\right)$.

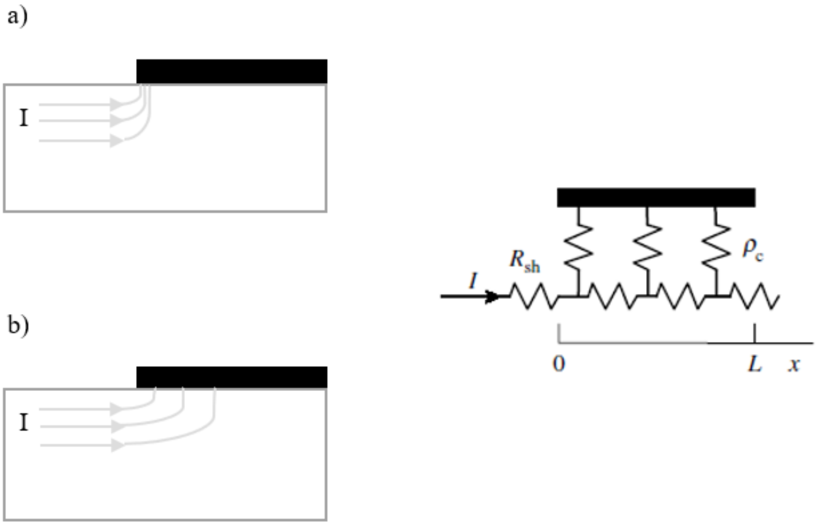

Fig. 4.16 Current flow from the semiconductor to the contact for a) lower and b) higher transfer length L_T, and on the right the resistance path of the equivalent circuit. ((Reproduced from Ref.138).

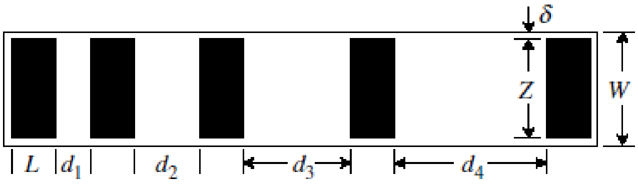

Fig. 4.17 Transfer Length Method (TLM) schematic pattern of contacts unequally spaced. (Reproduced from Ref. 138).

The total resistance, obtained from *I-V* characteristics, is plotted as a function of the contact distance *d* (see Fig. 4.17). The resulting plot provides three parameters, i.e. the sheet resistance, the contact resistance and the specific contact resistivity. The first one is extrapolated from the slope of the fitting curve trough the expression

$$\frac{\Delta(R_T)}{\Delta(d)} = \frac{R_{sh}}{Z} \tag{4.19}$$

The intercept of the fit at $R_T = 0$ and at $d = 0$ gives $-d = 2L_T$ and $R_T = 2R_C$, respectively, which lead to the specific contact resistivity, appearing in (4.18), and to the contact resistance.

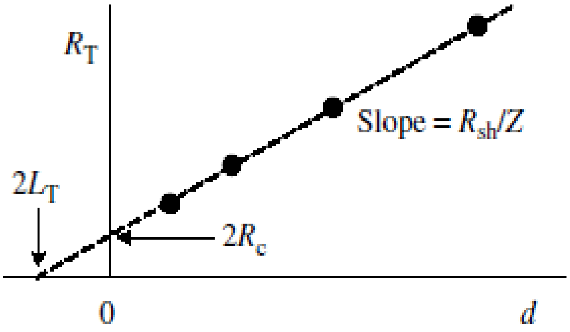

Fig. 4.18 Plot of total resistance, extracted by *I-V* characteristics, as a function of contact spacing. (Reproduced from Ref.138).

The measurements in dark were performed by using a Keithley Source Meter 2400, applying current and measuring voltage with two probes on each couple of contacts. The temperature dependent measurements were carried out with a Delta design 9023 climatic chamber, which was able to reach a temperature of 300°C. Additional measurements were also carried out illuminating the sample with a Xenon Lamp Oriel 6263 powered by a Spectra Physics 69931 power supplier. A monochromator Oriel Cornerstone 130/74000 was used to select the radiation wavelength incident on the sample surface. The typical wavelength involved for these investigations was 265 nm (4.68 eV), which corresponds to the energy bandgap of the studied samples. The TLM contact pattern, deposited on the studied films, and the simple photo-resistors schematic model created in planar geometry are shown in Fig. 4.19 (a) and (b).

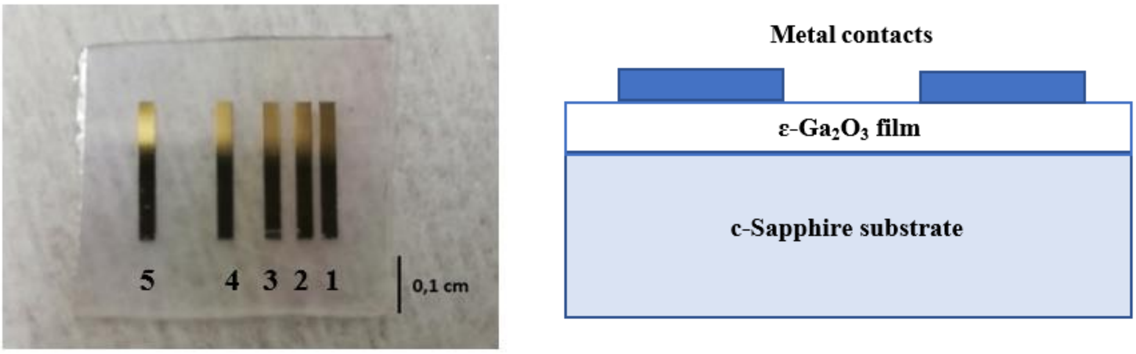

Fig. 4.19 On the left, the picture of the TLM contact configuration and, on the right, the schematic model of the simple photo-resistors investigated.

The *current-voltage* characteristics of undoped samples were obtained in dark and under illumination condition employing biases in the range 0-200V. Among the several investigated samples, the photo-resistor fabricated with specimen #146 exhibited the best ohmic conditions and performance. Figs. 4.20 (a,b) shows the *I-V* curves, taken over a wide voltage range, related to couples of contacts deposited at different distances (see Fig. 4.19), i.e. 1-2 = 0.2 mm, 2-3 = 0.4 mm, 3-4 = 0.8 mm and 4-5 = 1.6 mm respectively. The measured currents resulted proportional to the contact distances. An ohmic behavior of the curves was found for measurements performed in dark and under illumination. Typically, in dark measurements condition resistivity of the order of 10^7-10^8 Ωcm were estimated in undoped samples. The temperature dependent investigations were carried out at different temperatures up to 300°C and an increasing conductance of few orders of magnitude was observed. In some cases, the elevated resistivity at low temperature of the undoped samples, in dark measurement conditions, resulted in the order of the instrument input impedance and did not allow to record reasonable *I-V* characteristics. For this reason, in order to obtain resistivity parameters, temperature dependent investigations were carried out at different fixed temperatures from 250°C to 300°C. Then, the extracted value of resistivity led to an activation energy of 0.63 eV through an Arrhenius plot (Fig. 4.21). This energy value may be related to thermal ionization of a level positioned at about 0.7 eV below the CB, already observed by Pavesi *et al.*[21] on similar samples, producing a pinning of FL. The *I-V* characteristics in Fig. 4.20 (b) represent the plot of the data measured under UV radiation (265nm) at room temperature and environmental atmosphere conditions, which exhibit a photo-generated current of at least two order of magnitude higher than the value obtained by dark measurements.

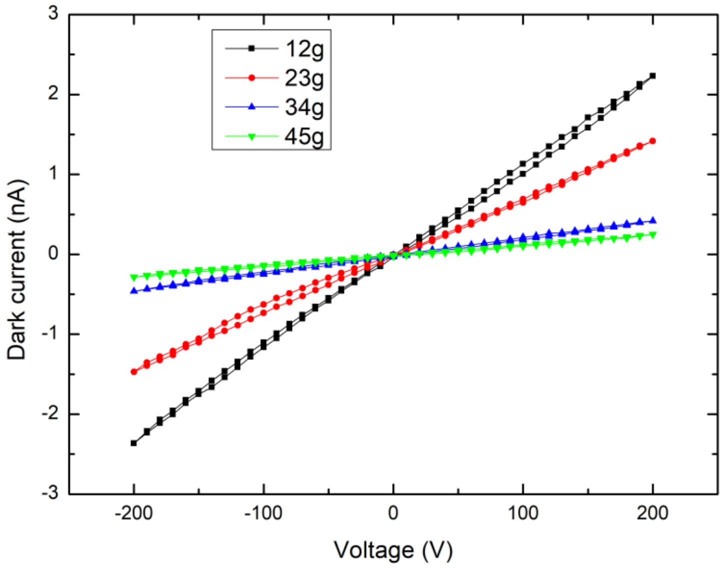

Fig. 4.20 a) *Current-Voltage* curves measured over a 0-200V voltage range on all the contact couples, spaced by different d_i, in dark conditions.

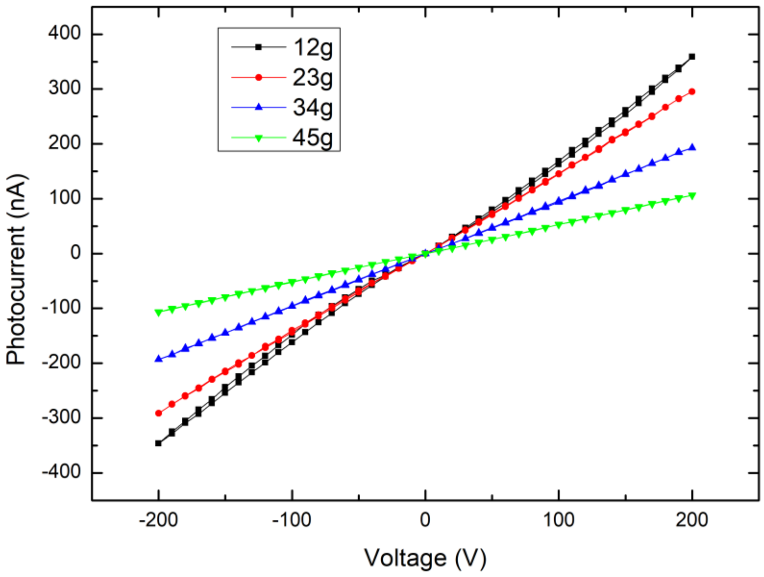

Fig. 4.20 b) *Current-Voltage* curves measured over a 0-200V voltage range on all the contact couples, spaced by different d_i, under UV illumination (265nm).

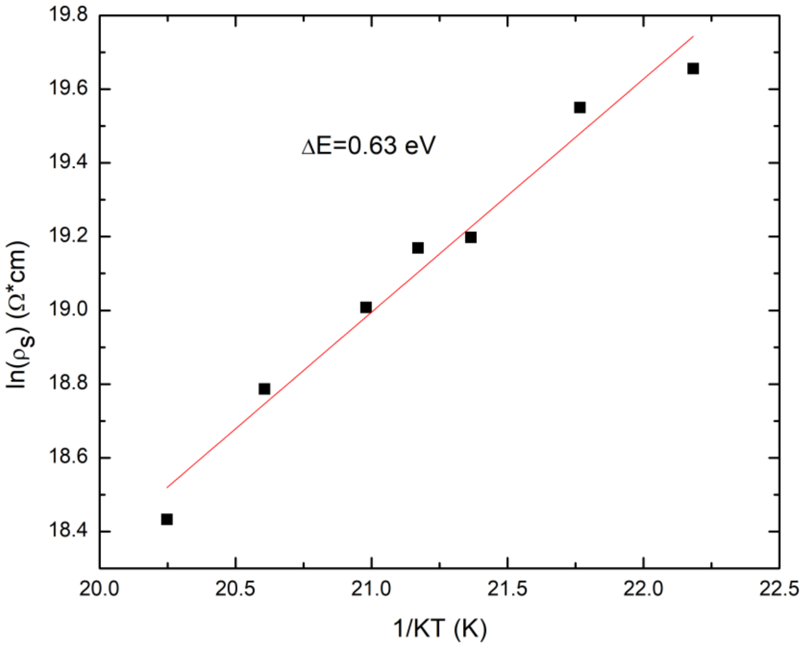

Fig. 4.21 Arrhenius plot of the natural logarithm of the semiconductor resistivity ρ_s.

Furthermore, solar-blind UV photodetectors could in principle be fabricated by employing ε-Ga_2O_3, as proved by significant photo-responsivity results. The photo-generated signal (Fig. 4.22), under UV radiation, exhibited a quite good stability over long periods of few hundred seconds and the time necessary to reach stationary conditions after on/off switching time is about 10s. Multiple cycles were repeated and the response remained practically the same, confirming a significant stability and reproducibility.

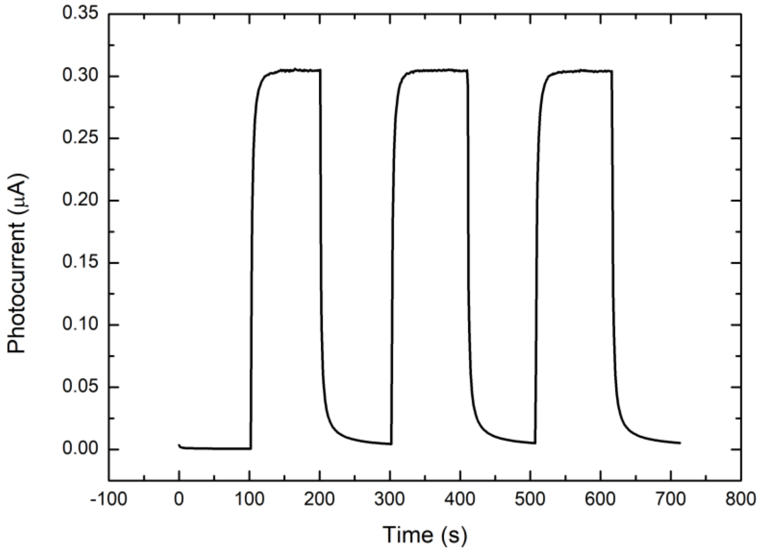

Fig. 4.22 Time-dependent photo-response obtained using UV radiation (265nm) and applying a bias of 200V.

Responsivity tests were also carried out in standard condition (25°C and constant humidity). The sample photo-response was measured on a wavelength range from 400nm to 250 nm with a step of 1 nm, and corrected considering the Xenon Lamp emission, which is taken with a Newport Optical Power Meter 840 and divided by the calibration curve. Then, the obtained values were normalized on the sample active area between the investigated contacts. Finally, the responsivity results, expressed as the ratio between the photo-current data and the normalized lamp power, were plotted in function of wavelength (Fig. 4.23).

Due to its wide bandgap, the ε-Ga_2O_3 films show a significant response only to deep UV, of several order of magnitude compared to the signal corresponding to below-bandgap wavelengths. The sample grown using H_2 resulted the most sensible to UV radiation, as observable in Fig. 4.21. Furthermore, As shown in the same figure, the responsivity is not flat between 400 nm and bandgap edge. This phenomenon can be probably related to presence of defect-related energy levels. Independently from the carried involved during the growth, the onset of the curve is present in each observed sample. Among the analyzed films, the one grown with H_2 as carrier gas exhibits a less pronounced behavior in the same wavelength range, may be indicating an amount of defects lower than the sample grown with other carriers. However, it must be said that, partially, this “hump” could be due to some artifacts introduced by the lamp emission and other optical components which may have affected the whole set of responsivity measurements. Anyway, the considerable response to UV illumination and the optical characteristics very similar to those β-Ga_2O_3[20] make this polymorph a serious candidate for solar-blind detectors

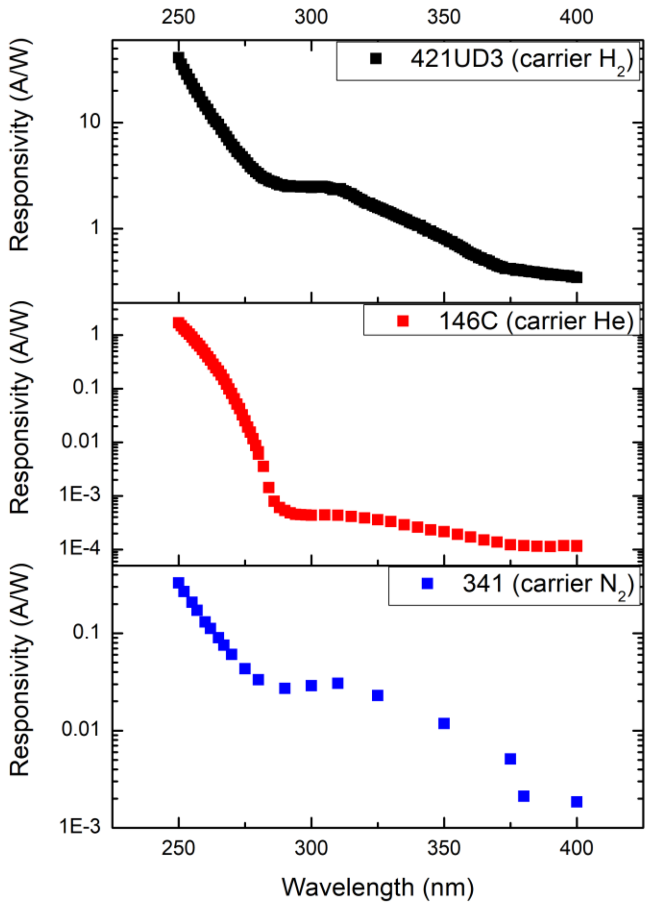

Fig. 4.23 Responsivity results of undoped samples grown using different carrier gas. Data are recorded over the 400-250nm wavelength range.

Chapter 5 - Deep level investigation

Defect-related deep levels heavily affect the semiconductor properties and it is therefore important to understand their behavior and nature. In Ga_2O_3, as well as in other semiconductor oxides, deep levels can introduce compensation effects, reducing carrier mobility[143]. Further they can cause a "pinning" of the Fermi level[18],[144] and behave as traps[145], thus limiting the breakdown voltage[146]and can give rise to PPC (persistent photoconductivity) phenomena[147]. For this reason, deep levels in ε-Ga_2O_3 films have been widely investigated in the frame of this thesis and the obtained results are reported and discussed in this chapter. These deep defect states in gallium oxide are intensively investigated by different techniques and their main features are known[61,83,148–154]. Through DLTS (deep-level transient spectroscopy) and DLOS (deep-level optical spectroscopy) measurements, Zhang et *al.*[61] identified five trap levels into the energy gap of β-Ga_2O_3 bulk crystals, located at 0.62 eV, 0.82 eV, 1.00 eV, 2.16 eV and 4.40 eV below the conduction band, with concentration of traps between 10^{14}-10^{16} cm^{-3}. The higher concentrations were detected for the levels at 0.82 eV and 4.40 eV, which depend from deep traps associated to Mg_{Ga}, Fe_{Ga} or V_O[17,116,155] and V_{Ga}[156], respectively. The first three trap energy levels are in agreement with the results published by Irmscher et *al.*[18]. Furthermore, the presence of deep levels in semiconductors is often investigated by luminescence measurements which allow to detect the defects through the recombination of photogenerated carriers. In β-Ga_2O_3, typical emission spectra exhibit UV and blue luminescence (BL) bands[80,82,83,149,150]. The first one has been attributed to a recombination of free electrons and self-trapped holes (STH)[82,109], while the blue emission seems to be related to a donor-acceptor pair (DAP) recombination which involves deep donors and acceptors[80]. The origin of the donor levels is attributed to interstitial Ga_i and to oxygen vacancy V_O[80,83,116], with a calculated ionization energy higher than 1 eV[17,116]. The deep acceptors are, instead, associated to V_{Ga} or V_O-V_{Ga} complexes[80,83,154]. In Si-doped crystals a resistivity-dependent BL is observed and the UVL seems to involve Si_{Ga} impurities in DAP transitions[81].

Concerning the ε-polymorph, information related to deep levels in literature is poorer. Pavesi et *al.*[21] first noticed deep energy bands in ε-Ga_2O_3 by PCS and absorption measurements, as already shown in Fig. 1.18b, in the first chapter of this thesis. Furthermore, they estimated a thermal activation energy of the conductivity of 0.7 eV, which is justified by a Fermi level pinned in that position by deep donor levels. One should note that such ionization energy seems to be comparable to that of the unknown donor observed in β-Ga_2O_3[18,61]. The presence of deep levels is further confirmed by Pavesi et *al.*[21] involving cathodoluminescence spectroscopy which detected three transitions from CB to three acceptor levels positioned at 2.34 eV, 2.67 eV and 2.75 eV below the conduction band, respectively.

5.1 Absorption and Cathodoluminescence measurements

As anticipated (Fig. 4.21), photo-response measurements show in some samples, the onset of the signal around 350nm (3.54 eV) probably indicative of deep bands into the energy gap. Additional absorption spectra were carried out in a wavelength range between 800-200nm, performed with a double beam dispersive spectrophotometer Varian 2390. The optical bandgap were observed on a large set of samples with different thickness and resulted between 4.6 eV and 4.8 eV, in good agreement with previous works reported in the literature[21,23]. In many cases, independently of the carrier gas used during the growth processes, a significant absorption started already at 2 eV and the spectra exhibited a long tail before reaching the fundamental absorption edge. It is worth to note that a weak absorption well below the band edge may be due also to defects at the surface or at the film/substrate interface, other than to bulk deep levels, as seen in Ref.21 on very similar samples. Although samples grown with hydrogen and nitrogen carrier show similar spectra, mostly the N_2 seems to promote the formation of bands inside the gap. Fig. 5.1 shows the absorption spectra of two ε-phase films, grown involving H_2 and N_2 carriers, whose are observable significant long tails. Clear interference fringes are also observed in the range between 4.5 and 1.5 eV.

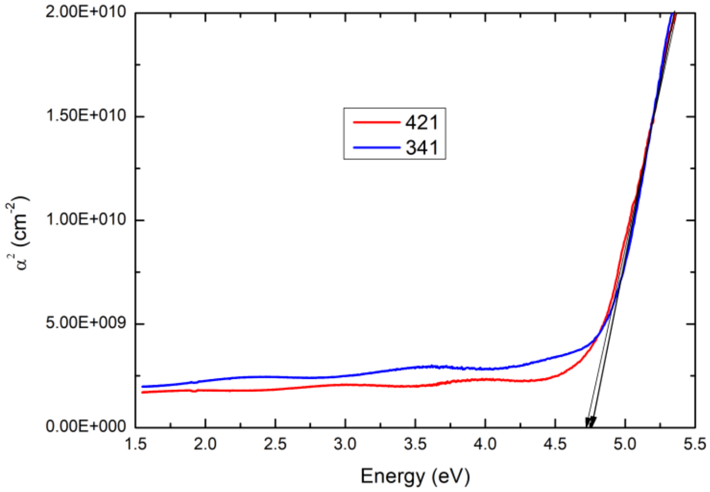

Fig. 5.1 Absorption spectra of undoped ε-Ga_2O_3 samples grown with H_2 and N_2 as carrier gas.

In order to further investigate the nature of these deep levels, temperature-dependent cathodoluminescence measurements were carried out during a research period at the University of Valladolid in Spring 2019. This investigation was carried out on a set of ε-Ga_2O_3 samples grown under different conditions using a MonoCL2 system from Gatan installed in a field-scanning electron microscope (FESEM-LEO 1530). A Peltier-cooled CCD detector was utilized for the spectral analysis while panchromatic images were recorded with a photomultiplier tube. Each film was investigated at 80K, while CL spectra dependent on the temperature were taken on some selected samples in a range of 80-280K. The energy of the e-beam was varied from 5 and 30KeV and the corresponding penetration depths, in gallium oxide layers, were estimated between 270 nm and 4 µm, respectively, using Montecarlo simulation through the Casino software. A negligible charging effect was observed in all the applied experimental conditions. In thinner films the e-beam probably reached the substrate, therefore, in order to avoid ambiguous interpretations, temperature-dependent spectra of the sapphire substrate were acquired to be able to identify any contribution from the substrate to the CL spectra of the thin films and consider it in the analysis of the relevant epitaxial structures . Fig. 5.2 shows the sapphire CL spectra as a function of the temperature, where the only evident emission is observable in the UV region at 3.75 nm (330nm), while a quite flat behavior characterizes the visible range, suggesting that no significant contribution could affects the Ga_2O_3 emissions in this region.

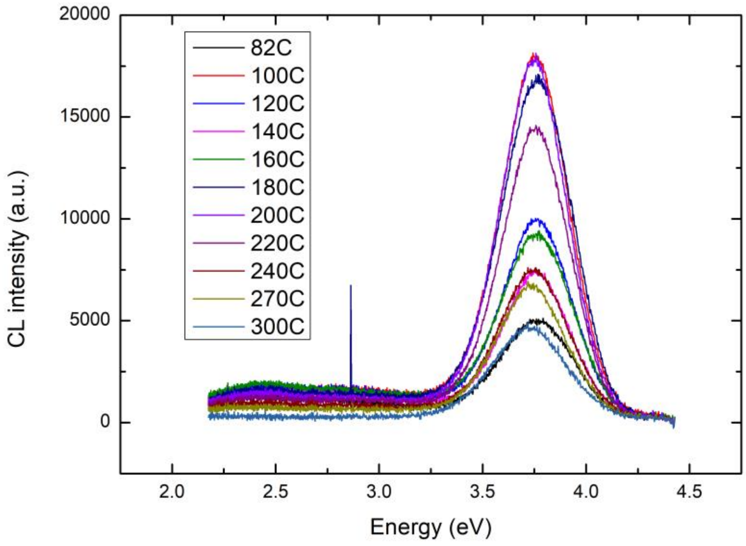

Fig. 5.2 Temperature-dependent CL spectra of a sapphire substrate film.

Table 5.1 resumes the main parameters of the all selected films studied and analyzed by cathodoluminescence investigation.

Samples and SiH_4 flow (sccm)	T(°C) P(mbar)	Carrier flux (sccm)	Carrier	Thickness (nm)	Time (min)	O/Ga ratio
#146/UD	650 - 100	200	He	500	15	205
#395/UD	610 - 60	1000	H_2	300	15	349
#341/UD	610 - 72	1000	N_2	250-350	120	242
#342/ 0.005	600 – 80	1000	N_2	450	120	218
#344/ 0.001	600 – 80	1000	N_2	350	120	218
#348/ 0.0125	610 – 75	1000	N_2	800	120	233
#425/UD	610 – 60	1000	H_2	6000	320	349
#426/ 0.005	610 – 60	1000	H_2	1000	60	349
#430/ 0.0125	610 – 60	1000	H_2	1000	60	349
#431/ 0.05	610 – 60	1000	H_2	900	60	349

Tab. 5.1 Principal growth parameters and properties of analyzed samples.

All the samples investigated at the temperature of 80K, both silicon doped and undoped, show very similar spectral distribution. A CL spectrum, recorded at 80K, of a thick ε-Ga_2O_3 film (5 μm), which is surely not affected by the substrate contribution, is presented in Fig. 5.3. The spectrum exhibits a broad band extended in a spectral range between 2 eV and 3.4 eV, which was very well approximated by four bands, obtained by Gaussian deconvolution, centered at 2.4 eV (517 nm), 2.75 eV (450 nm), 3.0 eV (413 nm) and 3.15 eV (394 nm). The choice to analyze the CL data taking into account four bands depends on the fact that all the investigated samples, also under different temperatures, can be well fitted by four Gaussians. The best fit was reached fixing only the peak position of 3.0 eV and 3.15 eV, in order to avoid any possible analysis artifacts. In addition, no band-to-band emission was detected.

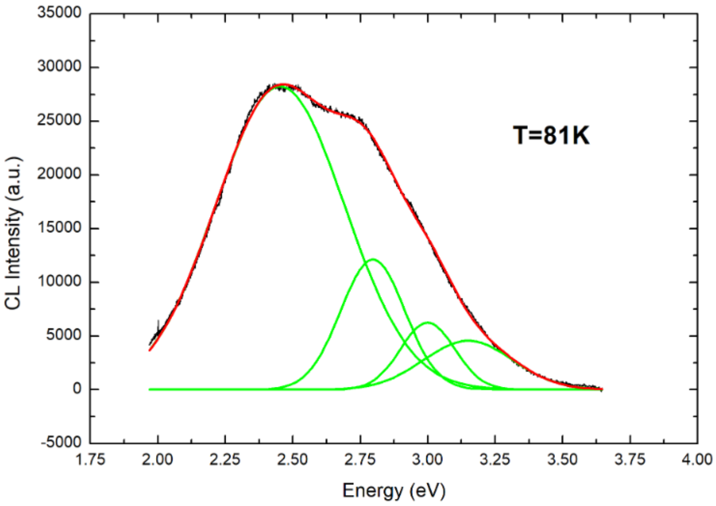

Fig. 5.3 Typical CL spectrum of an Undoped ε-Ga_2O_3 thick sample (5-6 μm) recorded at 80K. Four Gaussian bands are visible, related to deep levels inside the energy gap.

The temperature dependence of the CL spectra was studied on a thick unintentionally doped sample (5-6 μm). This film is characterized by a RT resistivity of about 10^4 Ωcm, i.e. three order of magnitude more conductive than typical undoped specimens (~10^7 Ωcm). The latter showed a deep donor state located at ~0.7 eV below the CB which pinned the Fermi level, while probably in the analyzed thick film the presence of non-intentional shallow donors caused this low resistivity. The spectra were acquired, using a temperature controller, in a range of 80-280K with an increasing step of 10K, in stationary conditions (see Fig. 5.4a).

The FWHM and the peak energy positions of the four broad emissions, obtained from band deconvolution, remained quite similar at each applied temperature. The temperature-dependent integrated intensities of the four CL peaks are plotted in Fig.5.4b. Surprisingly, from 80K to 100K, the emission intensities increased for all four peaks. This unusual behavior may be due to thermal excitation of electrons in CB from a shallow level, which then recombine in the deep levels. Above 100K, the emissions of all bands decreased monotonically. This trend could probably be related to the electron transition from the CB to acceptor states, in competition with non-radiative recombination via killer centers, as described by the Schön-Klasens effect for thermal quenching[157]. Furthermore, no self-trapped excitons were recognized and, for this reason, the recombination of thermal escaped holes in a killer center is attributed to the thermal quenching mechanism. Binet *et al.*[80] and Onuma *et al.*[81] proposed similar models for the temperature-dependent luminescence in β-polymorph.

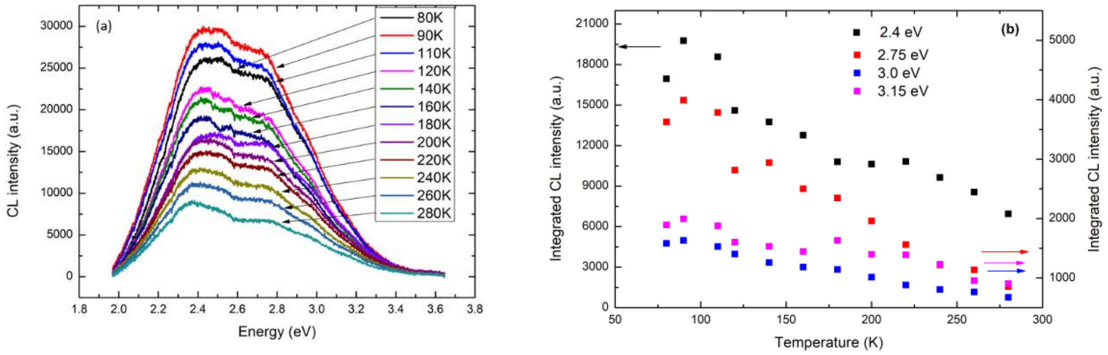

Fig. 5.4 Temperature dependent a) CL spectra and b) integrated emission intensities carried out in a range of 80-280K.

As presented in Fig. 5.1, a weak absorption is observable already between 2-2.5 eV, i.e. significantly below the band edge transition, indicating the onset of electron transition between in-gap states or from deep energy states and the conduction band. As the photocurrent signal also starts rising up at the same energies, it seems confirmed that the transitions actually occur from levels located into the energy gap to the CB. Additionally, an electron emission from deep levels, positioned at ~1.1 eV above the valence band maximum (VBM), was detected by ARPES measurements on similar samples, as reported by Mulazzi *et al.*[56]. Considering that no band bending resulted from this investigation, the deep states are probably associated to bulk defects, rather than to surface states. Combining these data together with the emission intensity behavior of CL spectra, a schematic model representative for the observed optical transitions could be introduced (see Fig. 5.5).

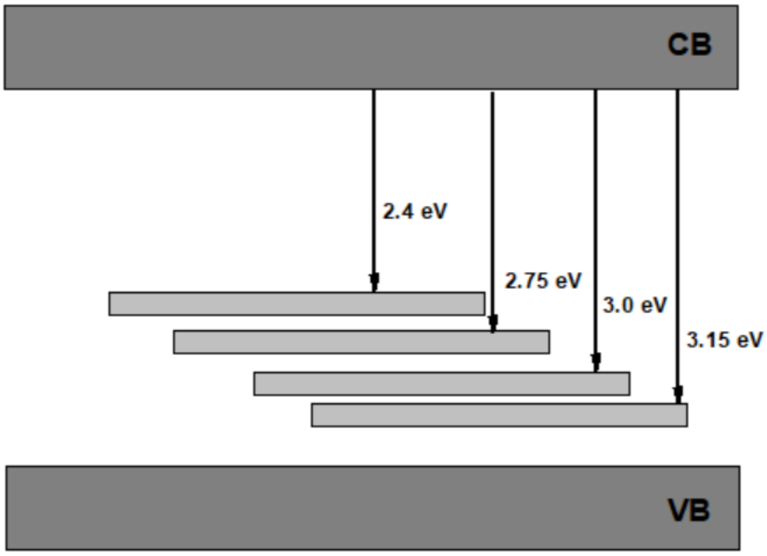

Fig. 5.5 Schematic band diagram with the four possible transitions between CB and the deep levels.

It is worth to note that, with respect to β-Ga_2O_3, no evidence of donor-acceptor pair (DAP) transitions was noticed in the investigated ε-phase films and, as observable in Fig. 5.5, the CL emissions may be related to transitions between the conduction band and four deep states. The origin of these deep levels has not yet been determined in ε-Ga_2O_3, but in analogy with the interpretation of the CL spectra in d β-polymorph (discussed above) they can be tentatively identified as Ga vacancies (V_{Ga}) or V_O-V_{Ga} complexes[80,154]. In Ref.154 defects were intentionally generated in β-Ga_2O_3 bandgap by different techniques in order to understand their nature, and a relation between 2.5 eV and 3.0 eV emissions and gallium vacancies was detected, while a 3.5 eV level was considered oxygen vacancy-related. Therefore, by comparison, the bands centered at 2.4 eV, 2.75 eV and 3 eV, detected in ε-phase samples, may be associated to V_{Ga} defects in the three differently coordinated Ga sites. In the β-polymorph, a 3.5 eV band was reported (Ref. 154) that was attributed to a transition involving V_O, however there is no evidence of this emission in the analyzed ε-films. A relation of the 3.15 eV band with oxygen vacancy-related defects does not seem likely, owing to the very low intensity of such a peak, which contrasts with the high probability of oxygen vacancy presence. It is more probable that these defects generate deep levels not involved in the CL emission.

Concerning the study of CL emission in n-type films, several samples with different Si concentration were investigated. The emission intensity behavior resulted strongly dependent on Si-doping, however, the energy position of the peaks remained unaltered for each dopant density.

The luminescence emission intensities showed in Fig 5.6a,b exhibit a decreasing trend with the increasing doping concentration for all studied samples. The typical broad CL emission, ascribed to four underlying bands, is seen in both series of samples, independently of the carrier type. The intensity decrease appeared to be similar both for films grown using hydrogen and nitrogen as carrier gas, although the CL emission intensities of samples with N_2 carrier were generally much less intense than in the films with H_2 carrier. Actually, even a little amount of silane is sufficient for an almost complete quenching of the 3.0 and 3.15 eV peaks in films grown with N_2 as carrier. The drop of the integrated CL intensities with silicon density is enhanced using nitrogen as carrier gas, which points to a compensating effect of nitrogen, i.e. pronounced non-radiative recombination. The decreasing of the blue luminescence was reported to be associated to a decrease of the resistivity[149], so the V_{Ga}-related defects density reduction consequent to Si incorporation might result in emission intensity reduction. Figs. 5.7a,b show the integrated emission intensity of both series of samples (with carrier H_2 and N_2) and, as evident, the 3.15 eV band results already weak at very moderate silane flows, suggesting that Si incorporation also alters the ratio between concentrations of different deep levels.

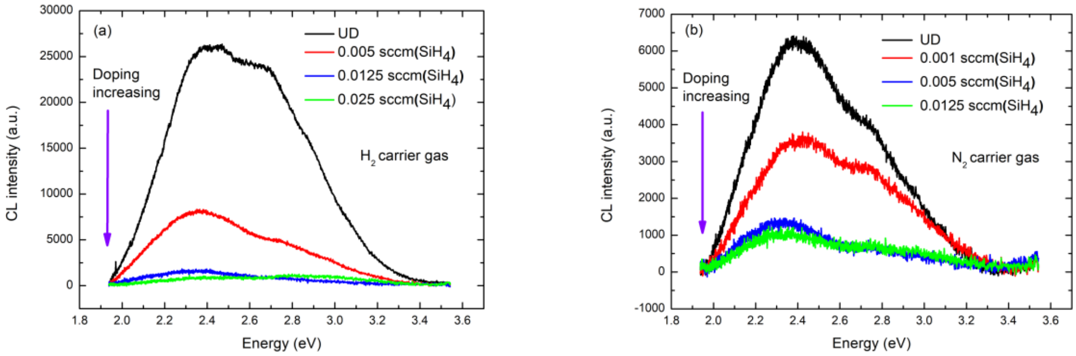

Fig. 5.6 CL spectra of two series of samples grown with different SiH_4 concentrations and using a) H_2 and b) N_2 as carrier gas.

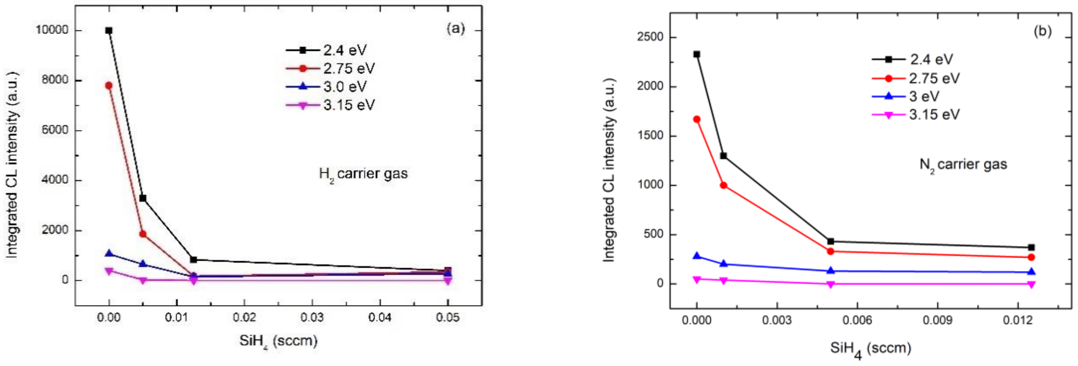

Fig. 5.7 Integrated CL intensity vs SiH4 flow of films grown with a) H_2 and b) N_2 carrier gas.

As seen in Fig. 5.6 b, nitrogen seems to enhance the band centered at 2.4 eV with respect to the other levels, indicating a probable action of N_2 in formation mechanisms of deep states. This is better understood by looking at Fig. 5.8 where the CL spectra of samples grown with different carrier gas are reported. The intensity of the peaks corresponding to different deep levels changes drastically with the used carrier gas. Additionally, it should be mentioned that electrical measurements previously carried out on Si-doped films deposited under different carrier gas demonstrated the dependence of electron density from the carrier used, which also corroborate the idea of a direct involvement of the ambient gas in the defect formation.

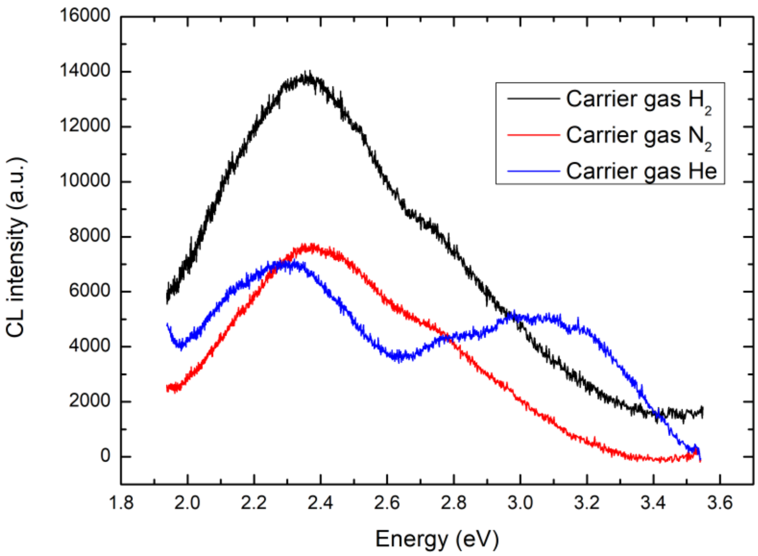

Fig. 5.8 CL spectra of films grown with different carrier gas. Emission intensity and ration of emissions for different peaks strongly depends on the involved carrier.

The SEM images of ε-Ga_2O_3 layers showed that often “hexagonal” islands nucleate on the surface, as also discussed in Ref.46, and expand laterally. In Fig. 5.9, one of such islands is reported along with the corresponding CL spectrum, compared to the spectrum taken outside the hexagon. The two CL spectra exhibit a significant difference in emission intensity of the peaks located at 2.75 eV and 3.0 eV (see Fig. 5.9b). These differences support the hypothesis of CL emissions associated to native point defects whose concentration depends on the local growth rate. Actually, the hexagonal regions quickly expand laterally while the flat film outside grows slowly vertically. As a result, the spectrum of the island is characterized by dominant 2.75 eV and 3.0 eV bands, which are much less intense in the outside flat layer.

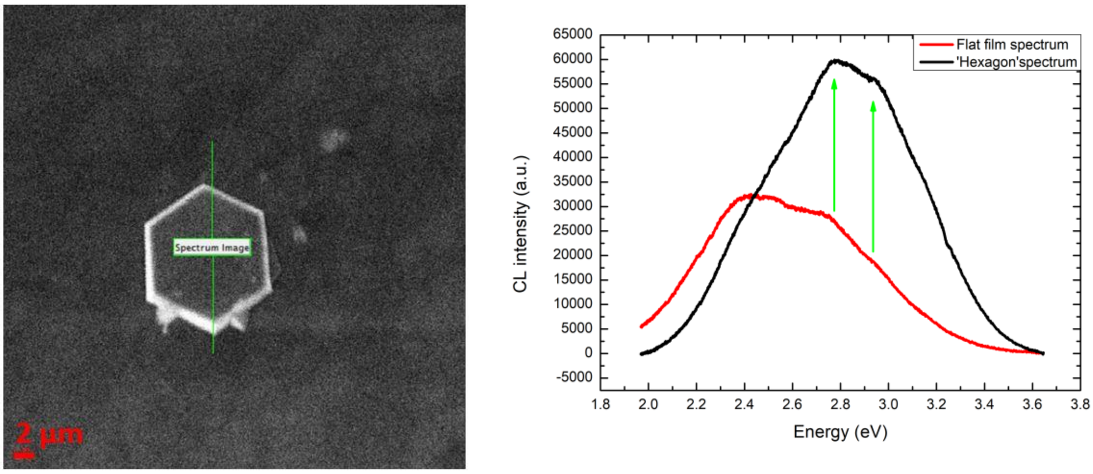

Fig. 5.9 a) “Hexagonal” surface structure. b) Comparison of CL spectra taken on floor layer and on the hexagon structure.

Conclusions

The multiple application fields, in which gallium oxide can be conveniently utilized, contributed to the scientific and technological interest towards this semiconductor. In fact, in the last decade the number of Ga_2O_3 publications increased exponentially, highlighting a rising attention by the semiconductor research community. Nevertheless, with regard to several fundamental aspects, Ga_2O_3 can still be considered a “new” material, especially concerning meta-stable phase properties. The research activity discussed in this work covered a wide range of topics, from the epitaxial crystal growth of ε-Ga_2O_3 thin films to the realization and characterization of very simple devices, passing through a series of different physical investigations, and provided new results and information on the ε-polymorph. The principal conclusions can be summarized as follows:

A good MOCVD growth reproducibility for undoped ε-Ga_2O_3, on *c*-Al_2O_3 substrates, was achieved, with the optimal growth parameters in the range between 600-650°C and 60-80 mbar for the temperature and the pressure, respectively. Samples prepared with these parameters exhibited high crystallinity and good morphological quality, checked through X-Ray diffraction and SEM analysis. Thermal stability of undoped ε-thin films were studied with the aim of understanding the actual ε-phase stability and the effective transition temperature to the thermodynamically stable β-polymorph. Some specimens of the same sample were separately annealed at stationary temperatures between 700°C and 900°C in two different atmospheres (N_2 and O_2). XRD measurements performed on these films revealed that the ε-polymorph crystal structure, observed in the as-grown layer, remained unchanged up to 700°C, where no evidence of β-phase was detected. At 800°C a structural degradation led to an “amorphization” stage, as noticed by the drop of the ε-reflection intensities. The absence of both ε- and β-phase suggests an intermediary disordered condition characterized by a loss of crystallinity. Then, diffraction patterns of specimens annealed at 900°C showed only reflections related to β-phase suggesting a completion for the phase transition. These results well compared with data provided by DSC analysis which described an initial re-organization of the crystal structure already at ~650°C and a total conversion to the stable phase, energetically favorable above 880°C-890°C. Furthermore, TEM measurements performed on selected samples treated at 1000°C and then cooled at different rates showed the formation of certain β-Ga_2O_3 grains with orientations dependent on the cooling rate.

Silicon doped ε-Ga_2O_3 films were also obtained, taking similar growth conditions as for undoped specimens, adding diluted silane into TMG precursor line and flowing both reactants together up to the growth chamber. Several samples were reproducibly grown with different silane concentrations that maintained acceptable morphological and crystalline quality. Samples doped with tin by high-temperature diffusion were also prepared. After contact deposition, electrical and photo-electrical characterizations were carried out on Si- and Sn-doped and undoped samples, respectively. Electrical investigations were performed through resistivity and Hall measurements, in dark and under illumination, in a temperature range between 10-600K using the van der Pauw method in order to find the material resistivity, the mobility and carrier concentration. Negative Hall coefficients were found, so it is possible to assume that a n-type doping is induced by Si and Sn impurities also in ε-Ga_2O_3 films. However, a continuous variable slope was observed in the Arrhenius plot of the resistivity data while a linear trend is shown when the values were plotted following to the Mott law, suggesting a transport mechanism based on the variable range hopping (VRH), i.e. a hopping conduction of the electrons between localized states. The two slopes, clearly identified in the plot of ln(ρ) vs $T^{-1/4}$, which follows the Mott law, could be related, at first sight, to two defects which participated to distinct hopping processes activated in two different temperature ranges. Comparing the resistivity results of all samples, it was found that lower slopes corresponded to lower resistivity films, self-consistently. Then, the density of sites estimated from the “Mott plot” (up to 10^{20} cm^{-3}), which identifies the concentration of the localized states taking part to the hopping process resulted higher than the RT Hall density (in the order of 10^{17}-10^{18} cm^{-3}). This is reasonable considering that the carrier concentration must to be lower than the available sites in order hopping to take place. ToF-SIMS, RBS and EPR investigations, performed by partner institutions, provided further confirmations in support of the described transport model and additional information regarding origin of the two different transport regimes, defect nature, impurity incorporation and compensation effects. Through ToF-SIMS, information about the incorporation profile of Si and Sn was obtained: a homogeneous Si incorporation was detected in the whole film thickness, as expected by the in-situ silane doping during the growth, while the Sn-doped film presented a typical exponential diffusion profile. Rutherford backscattering (RBS) measurements were carried out on Sn-doped samples to further demonstrate the tin penetration in the gallium oxide film. It was observed that the SnOx layer, deposited by RF sputtering, after thermal treatment exhibits a decreasing Sn content between the upper surface and the interface between the layer and the substrate, consistent with the Sn atom diffusion into Ga_2O_3. EPR spectroscopy allowed to determine the preferential position occupied by silicon atoms in ε-Ga_2O_3. Si impurities tend to occupy tetrahedral Ga sites in β-polymorph, which is characterized by only one octahedral and tetrahedral coordination, respectively. The more complex ε-Ga_2O_3 crystal structure presents three non-equivalent Ga sites, of which two are octahedrally coordinated and one has tetrahedral symmetry. The single paramagnetic defect revealed by EPR, however, indicated that Si preferentially takes the tetrahedral Ga sites. A spin concentration of 2.1×10^{18} cm^{-3} were obtained, which well compares with carrier concentration given by RT Hall effect measurements demonstrating a direct relation between paramagnetic defect detected by EPR and the donor giving n-type conductivity. The EPR signal intensity and linewidth exhibited a strong temperature dependence, and their different variation in distinct temperature ranges identified specific transport regimes. While localized electrons are detected for T<50K, above such a temperature, a VRH transport mechanism, related to impurity band conduction, is observable in two separate regimes, confirming the slopes obtained from the Mott plot of the resistivity data. However, for T>100K EPR investigation indicate an extended state transport into conduction band, in opposition to electrical data that again detects VRH transport. This difference suggested to interpret the double VRH in terms of dopant clustering with a donor-cluster formation. In this picture, the low-T VRH takes place between isolated Si impurities, whereas it is possible to suppose that, by increasing the temperature, electrons become delocalized into clusters, but the macroscopic conduction can only take place by hops between clusters, following the percolation theory.

Optical and photo-electrical measurements were also performed using the Transfer Length Method (TLM) through which it was possible to extract sheet and specific contact resistance analyzing the measured *current-voltage* characteristics and to achieve an activation energy value involving temperature dependent investigations. This extrapolated energy value of ~0.63 eV may be related to thermal ionization of a level positioned at about 0.7 eV below the CB, which caused a pinning of the Fermi level. Typically, undoped samples exhibited resistivity values in dark conditions of 10^7-10^8 Ωcm. The photo-generated current detected when the films were illuminated under UV radiation (265nm) resulted of at least two order of magnitude higher than the value obtained by dark measurements. The photo-generated signal showed good stability over long periods (hundred seconds) and relatively short on/off switching time (~10s). The significant responsivity to deep UV proved that ε-Ga_2O_3 can be applied for UV solar-blind photo-detectors fabrication.

Responsivity investigations and absorption measurements, carried out on different samples, provided spectra characterized by an onset of the signal well below the band edge, suggesting the presence of deep bands into the energy gap. In many cases a non-negligible absorption started already at 2 eV, probably due also to defects at the surface or at the film/substrate interface. In order to fully understand the nature and behavior of these deep levels, cathodoluminescence measurements were performed on a large set of samples grown with different carrier gas. All investigated films presented CL spectra characterized by a broad band in the spectral range between 2 eV and 3.4 eV, which can be deconvoluted in four narrower bands centered at 2.4 eV (517 nm), 2.75 eV (450 nm), 3.0 eV (413 nm) and 3.15 eV (394 nm). The FWHM and energy positions of the four emissions remained quite similar also in temperature-dependent spectra. Temperature-dependent investigations showed two different trends of the emission intensities related to the deep bands: from 80K to 100K, the increased intensities for all four peaks are due to thermal excitation of electrons in CB from a shallow level, which then recombine in the deep levels, while above 100K, the monotone decreasing of all band emissions is probably connected with non-radiative recombination on killer centers which prevents the optical transition from the CB to acceptor states, as described by the Schön-Klasens effect for thermal quenching. Combining the results obtained by absorption and photocurrent measurements with the emission intensity behavior of CL spectra is possible to introduce a schematic model where transitions occur from the CB to levels (arranged in bands) positioned into the energy gap. The origin of these deep bands has not yet been established in ε-Ga_2O_3, but by comparison with the interpretation of the CL spectra in the β-polymorph they can be tentatively associated to Ga vacancies (V_{Ga}), considering the four coordination of Ga sites found in ε-Ga_2O_3. Furthermore, it was found that Si-doping strongly influence the emission intensity behavior, leaving unchanged the energy position of the peaks for each dopant density. A decreasing intensity for increasing doping concentration is observed for all studied samples. In β- Ga_2O_3 the blue luminescence decrease was reported to be associated to a decrease of the resistivity, so the V_{Ga}-related defects density reduction consequent to Si incorporation might be the reason for the observed emission intensity reduction. Furthermore, the 3.15 eV band is already weak at very low silane concentration, suggesting that Si incorporation also influences the ratio between concentrations of different deep levels. It was also observed, in another set of samples, that the intensity of the four emission peaks strongly depended by the used carrier gas. This resulted consistent with the electrical measurements previously carried out on Si-doped films, which demonstrated a lower electron density in samples deposited with N_2 carrier gas with respect to those with H_2, for same silane fluxes, which supports the idea of the carrier gas active in determining the electrical properties. Whether this occurs via formation of compensating defects or sweeping of incorporated donors is still matter of investigation.

Appendix A – Additional information about thickness measurements

The ε-Ga2O3 refractive index n was estimated measuring several films by ellipsometry, which provided spectra in the region of the photon energy below the energy gap. These ellipsometric spectra were detected at different incidence angles leading to the fit of the refractive index n through a Cauchy dispersion model[158]. Therefore, the refractive index depends on the three Cauchy parameters A, B and C and may be written as a function of the wavelength λ, which varies slowly:

$$n(\lambda) = A + \frac{B}{\lambda^2} + \frac{C}{\lambda^4}$$

where A = 1.9508, B = 0.010398, and C = 0.00061257, for the studied ε-Ga2O3 samples. The resulting $n(\lambda)$ behavior is reported in the next Fig. A.

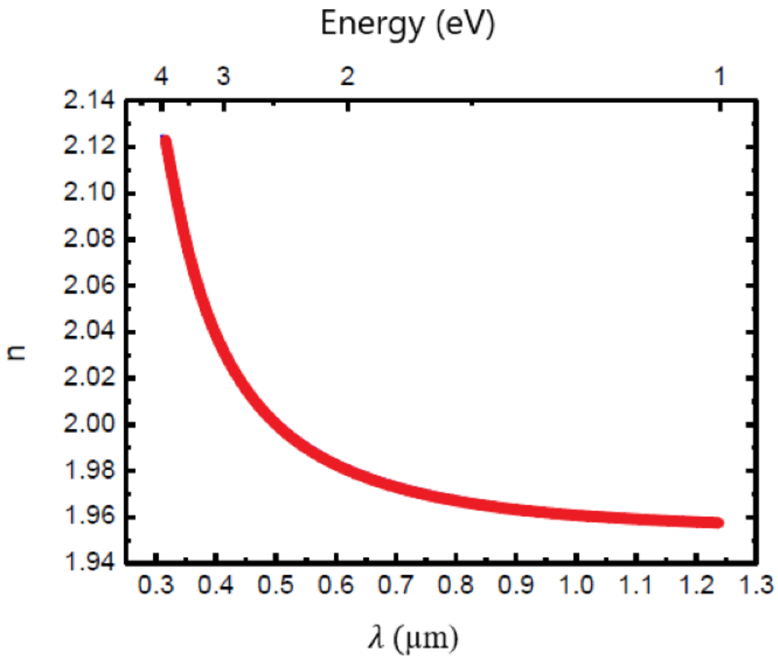

Fig. A Refractive index $n(\lambda)$ of ε-Ga2O3 obtained by ellipsometry measurements.

Concerning the refractive index of the ε phase no literature data were available. For this reason, Fig. A was employed as a reference curve of $n(\lambda)$ in order to determine the ε-films thickness using the interference fringes measured by reflectometry.

Appendix B – Publications

- M. Pavesi, V. Montedoro, F. Mezzadri, D. Klimm, I. Cora, A. Parisini, A. Baraldi, F. Boschi, M. Bosi, C. Ferrari, E. Gombia, and R. Fornari, *“Thermal stability and phase transition of ε-Ga_2O_3 polymorph”*, Acta Materialia 140 (2017) 411-416.

- Parisini V. Montedoro, A. Gorreri, M. Bosi, G. Garulli, S. Vantaggio and R.Fornari, *“n-type doping of ε-Ga_2O_3 layers”*, APL Materials 7 (2018) 031114.

- S. Leone, R. Fornari, M. Bosi, V. Montedoro, L. Kirste, P. Doering, F. Benkhelifa, M. Prescher; C. Manz, V. Polyakov, O. Ambacher, *“Epitaxial Growth of GaN/Ga_2O_3 and Ga_2O_3/GaN Heterostructures”*, Journal of Crystal Growth (2019), under submission.

- V. Montedoro, J. Jimenez, A. Torres, A. Parisini, M. Bosi, and R.Fornari, *“Cathodoluminescence of undoped and n-type doped ε-Ga_2O_3 films”*, to be submitted.

Appendix C – Conference Contributions

- 2nd International Workshop on Ga_2O_3 and Related Materials, *Thermal stability of* ε-Ga_2O_3 *polymorph*, V. Montedoro, M. Pavesi, F. Mezzadri, D. Klimm, I. Cora, A. Parisini, A. Baraldi, F. Boschi, M. Bosi, C. Ferrari, E. Gombia and R. Fornari, 12-15 September 2017, Parma, Italy.

- MATERIALS2018, *Growth and characterization of n-type* ε-Ga_2O_3 *doped films,* V. Montedoro, A. Parisini, A. Bosio, , M. Bosi, A. Gorreri, F. Mezzadri, G. Garulli, S. Vantaggio, E. Gombia, M. Pavesi, A. Baraldi and R. Fornari, 22-26 October 2018, Area della ricerca CNR, Bologna, Italy.

- MATERIALS2018, *Low resistance ohmic contacts on n-type Sn-doped* ε-Ga_2O_3 *thin films,* A. Bosio, A. Parisini, M. Pavesi, M. Bosi, V. Montedoro, A. Gorreri, G. Garulli, S. Vantaggio and R. Fornari, 22-26 October 2018, Area della ricerca CNR, Bologna, Italy.

- ECCG6 (Sixth European Conference on Crystal Growth), *Thin films of* ε-Ga_2O_3 *polymorph: doping, properties and applications*, A. Bosio, A. Parisini, M. Pavesi, G. Garulli, A. Gorreri, V. Montedoro, A. Baraldi, M. Bosi, F. Mezzadri, G. Calestani, and R. Fornari, 16–20 September 2018, Riviera Holiday Club, Varna, Bulgaria.

- CIMTEC 2018 (14th International Conference on Modern Materials and Technologies, 8th Forum on New Materials) – Symposium FJ, *Growth and properties of* Ga_2O_3 *thin films*, R. Fornari, A. Baraldi, V. Montedoro, A. Parisini, M. Pavesi, M. Bosi, C. Ferrari, E. Gombia D. Klimm, F. Mezzadri, G. Calestani, I. Cora, B. Pécz, 10-14 June2018 Perugia, Itay.

- SPIE 2018 (Oxide-based Materials and Devices IX, part of SPIE OPTO) ε-Ga_2O_3 *polymorph: epitaxial growth, properties and possible applications*, M. Bosi, M. Pavesi, V. Montedoro, D. Klimm, F. Mezzadri, G. Calestani, I. Cora, B. Pécz, F. Boschi, A. Parisini, A. Baraldi, C. Ferrari, E. Gombia, and R. Fornari. January 27th - February 1st, 2018, Moscone Convention Center, San Francisco, CA, United States.

- ICPS 2018 (International Conference on the Physics of Semiconductor), ε-Ga_2O_3 *epilayers and their application to solar-blind UV detectors*, A.Parisini, M.Pavesi, A.Baraldi, M.Bosi, E.Gombia, C.Ferrari, V.Montedoro, S.Vantaggio, D.Klimm, F.Mezzadri, I.Cora, B.Pecz, R.Fornari, July 29th – August 3rd , 2018, Montpellier, Canada.

- ICCGE 2019 (International Conference of Crystal Growth and Epitaxy) *Silicon and Tin doping of* ε -Ga_2O_3 *epilayers grown by MOVPE,* R. Fornari, A. Bosio, M.

Bosi, A. Parisini, Z. Zolnai, A. Lamperti, V. Montedoro, C. Borelli, M. Pavesi, July 22th – August 2nd, 2019, Keystone, Colorado, United States.

- ICCGE 2019 (International Conference of Crystal Growth and Epitaxy) *Epitaxial growth of GaN/*Ga_2O_3 *and* Ga_2O_3*/III-N Heterostructures*, R. Fornari, S. Leone, M. Bosi, V. Montedoro, L. K. Kirste, V. Polyakov, O. Ambacher, July 22th – August 2nd, 2019, Keystone, Colorado, United States.

Bibliography

1. de Boisbaudran, L. "On the chemical and spectroscopic characters of a new metal (gallium)". *London, Edinburgh, Dublin Philos. Mag. J. Sci.* **50**, 414–416 (1875).
2. Zheng, B., Hua, W., Yue, Y. & Gao, Z. "Dehydrogenation of propane to propene over different polymorphs of gallium oxide". *J. Catal.* **232**, 143–151 (2005).
3. Hou, Y. *et al.* "Photocatalytic performance of α-, β-, and γ-Ga_2O_3 for the destruction of volatile aromatic pollutants in air". *J. Catal.* **250**, 12–18 (2007).
4. Chang, S. J. *et al.* "Ga_2O_3 films for photoelectrochemical hydrogen generation". *J. Electrochem. Soc.* **161**, 508–511 (2014).
5. Fleischer, M., Giber, J. & Meixner, H. "H_2-induced changes in electrical conductance of β-Ga_2O_3 thin-film systems". *Appl. Phys. A Solids Surfaces* **54**, 560–566 (1992).
6. Fleischer, M., Höllbauer, L., Born, E. & Meixner, H. "Evidence for a Phase Transition of β-Gallium Oxide at Very Low Oxygen Pressures". *J. Am. Ceram. Soc.* **80**, 2121–2125 (2005).
7. Nakagomi, S., Sai, T. & Kokubun, Y. "Hydrogen gas sensor with self temperature compensation based on β-Ga_2O_3 thin film". *Sensors Actuators, B Chem.* **187**, 413–419 (2013).
8. Orita, M., Ohta, H., Hirano, M. & Hosono, H. "Deep-ultraviolet transparent conductive ß-Ga_2O_3 thin films". *Appl. Phys. Lett.* **77**, 4166–4168 (2000).
9. Zhang, J. *et al.* "Growth and characterization of new transparent conductive oxides single crystals β-Ga_2O_3: Sn". *J. Phys. Chem. Solids* **67**, 1656–1659 (2006).
10. Aida, H. *et al.* "Growth of β-Ga_2O_3 single crystals by the edge-defined, film fed growth method". *Jpn. J. Appl. Phys.* **47**, 8506–8509 (2008).
11. Galazka, Z. *et al.* "Czochralski growth and characterization of β-Ga_2O_3 single crystals". *Cryst. Res. Technol.* **1236**, 1229–1236 (2010).
12. Oshima, T., Arai, N., Suzuki, N., Ohira, S. & Fujita, S. "Surface morphology of homoepitaxial β-Ga_2O_3thin films grown by molecular beam epitaxy". *Thin Solid Films* **516**, 5768–5771 (2008).
13. Wagner, G. *et al.* "Homoepitaxial growth of β-Ga_2O_3 layers by metal-organic vapor phase epitaxy". *Phys. Status Solidi Appl. Mater. Sci.* **211**, 27–33 (2014).
14. Sasaki, K., Higashiwaki, M., Kuramata, A. & Masui, T. "MBE grown Ga_2O_3 and its power device applications". *J. Cryst. Growth* **378**, 591–595 (2013).
15. Kaneko, K., Ito, H., Lee, S. & Fujita, S. "Oriented growth of beta gallium oxide thin

films on yttrium-stabilized zirconia substrates". *Phys. Status Solidi C* **1599**, 1596–1599 (2013).

16. Víllora, E. G., Shimamura, K., Yoshikawa, Y., Ujiie, T. & Aoki, K. "Electrical conductivity and carrier concentration control in β-Ga_2O_3 by Si doping". *Appl. Phys. Lett.* **92**, (2008).
17. Varley, J. B., Weber, J. R., Janotti, A. & Van De Walle, C. G. "Oxygen vacancies and donor impurities in β-Ga_2O_3". *Appl. Phys. Lett.* **97**, 97–100 (2010).
18. Irmscher, K., Galazka, Z., Pietsch, M., Uecker, R. & Fornari, R. "Electrical properties of β- Ga_2O_3 single crystals grown by the Czochralski method". *J. Appl. Phys.* **110**, (2011).
19. Higashiwaki, M., Sasaki, K., Kuramata, A., Masui, T. & Yamakoshi, S. "Development of gallium oxide power devices". *Phys. Status Solidi Appl. Mater. Sci.* **211**, 21–26 (2014).
20. Guo, D. *et al.* "Fabrication of β-Ga_2O_3 thin films and solar-blind photodetectors by laser MBE technology". *Opt. Mater. Express* **4**, 1067 (2014).
21. Pavesi, M. *et al.* "ε-Ga_2O_3 epilayers as a material for solar-blind UV photodetectors". *Mater. Chem. Phys.* **205**, 502–507 (2018).
22. Matsumoto, T., Aoki, M., Kinoshita, A. & Aono, T. "Absorption and reflection of vapor grown single crystal platelets of β-Ga_2O_3". *Jpn. J. Appl. Phys.* **13**, 1578–1582 (1974).
23. Oshima, Y., Matsushita, Y., Yamamoto, S. & Shimamura, K. "Epitaxial growth of phase-pure ε-Ga_2O_3 by halide vapor phase epitaxy". **085301**, (2016).
24. Hudgins, J. L. *et al.* "An Assessment of Wide Bandgap Semiconductors for Power Devices". *IEEE Trans. POWER Electron.* **18**, 907–914 (2003).
25. Baliga, B. J. "Power Semiconductor Device Figure of Merit for High-Frequency Applications". *IEEE ELECTRON DEVICE Lett.* **10**, 455–457 (1989).
26. Roy, R., Hill, V. G. & Osborn, E. F. "Polymorphism of Ga_2O_3 and the System Ga_2O_3−H_2O". *J. Am. Chem. Soc.* **74**, 719–722 (1952).
27. Maccioni, M. B. & Fiorentini, V. "Phase diagram and polarization of stable phases of $(Ga_{1-x}In_x)_2O_3$ ". *Appl. Phys. Express* **9**, 041102 (2016).
28. Pearton, S. J. *et al.* "A review of Ga_2O_3 materials, processing, and devices". *Appl. Phys. Rev.* **5**, (2018).
29. Shinohara, D. & Fujita, S. "Heteroepitaxy of corundum-structured α-Ga_2O_3 thin films on α-Al_2O_3 substrates by ultrasonic mist chemical vapor deposition". *Jpn. J. Appl.*

Phys. **47**, 7311–7313 (2008).

30. GV Chaplyngin, S. S. "Preparation, structure and electrical properties of epitaxial films of gallium oxide on sapphire substrates". **32**, 321–324 (1976).
31. Stepanov, S. I., Nikolaev, V. I., Bougrov, V. E. & Romanov, A. E. "Gallium oxide: Properties and applications - A review". *Rev. Adv. Mater. Sci.* **44**, 63–86 (2016).
32. Oshima, T., Nakazono, T., Mukai, A. & Ohtomo, A. "Epitaxial growth of γ-Ga_2O_3 films by mist chemical vapor deposition". *J. Cryst. Growth* **359**, 60–63 (2012).
33. Cora, I. *et al.* "The real structure of ε-Ga_2O_3 and its relation to κ-phase". *CrystEngComm* **19**, 1509–1516 (2017).
34. Playford, H. Y., Hannon, A. C., Barney, E. R. & Walton, R. I. "Structures of uncharacterised polymorphs of gallium oxide from total neutron diffraction". *Chem. - A Eur. J.* **19**, 2803–2813 (2013).
35. He, H. *et al.* "First-principles study of the structural, electronic, and optical properties of Ga_2O_3 in its monoclinic and hexagonal phases". *Phys. Rev. B - Condens. Matter Mater. Phys.* **74**, 1–8 (2006).
36. Yoshioka, S. *et al.* "Structures and energetics of Ga_2O_3 polymorphs". *J. Phys. Condens. Matter* **19**, (2007).
37. Kroll, P., Dronskowski, R. & Martin, M. "Formation of spinel-type gallium oxynitrides: A density-functional study of binary and ternary phases in the system Ga-O-N". *J. Mater. Chem.* **15**, 3296–3302 (2005).
38. Mezzadri, F. *et al.* "Crystal structure and ferroelectric properties of ε-Ga_2O_3 films grown on (0001)-sapphire". *Inorg. Chem.* **55**, 12079–12084 (2016).
39. Galazka, Z. *et al.* "Scaling-Up of Bulk β-Ga_2O_3 Single Crystals by the Czochralski Method". *ECS J. Solid State Sci. Technol.* **6**, Q3007–Q3011 (2017).
40. Koshi, K. *et al.* "High-quality β-Ga_2O_3 single crystals grown by edge-defined film-fed growth". *Jpn. J. Appl. Phys.* **55**, 1202A2 (2016).
41. Nikolaev, V. I. *et al.* "Growth and characterization of β-Ga_2O_3 crystals". *J. Cryst. Growth* **457**, 132–136 (2017).
42. Ueda, N., Hosono, H., Waseda, R. & Kawazoe, H. "Anisotropy of electrical and optical properties in β-Ga_2O_3 single crystals". *Appl. Phys. Lett.* **71**, 933–935 (1997).
43. Akazawa, H. "Formation of various phases of gallium oxide films depending on substrate planes and deposition gases". *Vacuum* **123**, 8–16 (2016).
44. Sun, H. *et al.* "HCl Flow-Induced Phase Change of α-, β-, and ε-Ga_2O_3 Films Grown by MOCVD". *Cryst. Growth Des.* **18**, 2370–2376 (2018).

45. Tronc, E., Chane, C. & Jolivet, J. P. "Structural and Magnetic Characterization of ε-Fe_2O_3". *J. Solid State Chem.* **139**, 93–104 (1998).
46. Boschi, F. *et al.* "Hetero-epitaxy of ε-Ga_2O_3 layers by MOCVD and ALD". *J. Cryst. Growth* **443**, 25–30 (2016).
47. Yao, Y. *et al.* "Growth and characterization of α-, β-, and ε-phases of Ga_2O_3 using MOCVD and HVPE techniques". *Mater. Res. Lett.* **6**, 268–275 (2018).
48. Matsuzaki, K. *et al.* "Field-induced current modulation in epitaxial film of deep-ultraviolet transparent oxide semiconductor Ga_2O_3". *Appl. Phys. Lett.* **88**, 1–4 (2006).
49. Kracht, M. *et al.* "Tin-Assisted Synthesis of ε-Ga_2O_3 by Molecular Beam Epitaxy". **054002**, 1–8 (2017).
50. Kim, J., Tahara, D., Miura, Y. & Kim, B. G. "First-principle calculations of electronic structures and polar properties of (κ,ε)-Ga_2O_3". *Appl. Phys. Express* **11**, 061101 (2018).
51. Perdew, J. P. *et al.* "Restoring the density-gradient expansion for exchange in solids and surfaces". **136406**, 1–4 (2007).
52. Kresse, G. & Furthmüller, J. "Efficient iterative schemes for ab initio total-energy calculations using a plane-wave basis set". *Phys. Rev. B - Condens. Matter Mater. Phys.* **54**, 11169–11186 (1996).
53. Kresse, G. & Joubert, D. Kresse, Joubert "From ultrasoft pseudopotentials to the projector augmented-wave method". **59**, 11–19 (1999).
54. Furthmüller, J. & Bechstedt, F. "Quasiparticle bands and spectra of Ga_2O_3 polymorphs". *Phys. Rev. B* **93**, 1–16 (2016).
55. Stephens, P. J., Devlin, F. J., Chabalowski, C. F. & Frisch, M. J. "Ab Initio calculation of vibrational absorption and circular dichroism spectra using density functional force fields". *J. Phys. Chem.* **98**, 11623–11627 (1994).
56. Mulazzi, M. *et al.* "The electronic structure of ε-Ga_2O_3". *APL Mater.* **7**, 1–7 (2019).
57. Heyd, J., Scuseria, G. E. & Ernzerhof, M. "Hybrid functionals based on a screened Coulomb potential". *J. Chem. Phys.* **118**, 8207–8215 (2003).
58. Ricci, F. *et al.* "Theoretical and experimental investigation of optical absorption anisotropy in β-Ga_2O_3". *J. Phys. Condens. Matter* **28**, (2016).
59. Vanderbilt, D. King-Smith "Theory of polarization of crystalline solids". **47**, 1651–1654 (1993).
60. Rafique, S., Han, L. & Zhao, H. "Synthesis of wide bandgap Ga_2O_3 (Eg ~ 4.6-4.7 eV) thin films on sapphire by low pressure chemical vapor deposition". *Phys. Status Solidi Appl. Mater. Sci.* **213**, 1002–1009 (2016).

61. Zhang, Z., Farzana, E., Arehart, A. R. & Ringel, S. A. "Deep level defects throughout the bandgap of (010) β-Ga_2O_3 detected by optically and thermally stimulated defect spectroscopy". *Appl. Phys. Lett.* **108**, 2–7 (2016).
62. Liu, Z., Jing, X. & Wang, L. "Effects of O_2 Partial Pressure and Ga Atmosphere on the Luminescence of Native Defects in β–Ga_2O_3 Phosphor". *J. Electrochem. Soc.* **154**, H440 (2007).
63. Machon, D., McMillan, P. F., Xu, B. & Dong, J. "High-pressure study of the β -to- α transition in Ga_2O_3". *Phys. Rev. B - Condens. Matter Mater. Phys.* **73**, 1–9 (2006).
64. Dohy, D., Lucazeau, G. & Revcolevschi, A. "Raman spectra and valence force field of single-crystalline β-Ga_2O_3". *J. Solid State Chem.* **45**, 180–192 (1982).
65. Seshadri, H., Cheralathan, M. & Sinha, P. K. "Photocatalytic performance of combustion-synthesized β and γ-Ga_2O_3 in the degradation of 1,4-dioxane in aqueous solution". *Res. Chem. Intermed.* **39**, 991–1001 (2013).
66. Oshima, Y., Víllora, E. G. & Shimamura, K. "Halide vapor phase epitaxy of twin-free α-Ga_2O_3 on sapphire (0001) substrates". *Appl. Phys. Express* **8**, (2015).
67. Murakami, H. *et al.* "Homoepitaxial growth of β-Ga_2O_3 layers by halide vapor phase epitaxy". *Appl. Phys. Express* **8**, 015503 (2015).
68. Xia, X. *et al.* "Hexagonal phase-pure wide band gap ε-Ga_2O_3 films grown on 6H-SiC substrates by metal organic chemical vapor deposition". *Appl. Phys. Lett.* **108**, 1–6 (2016).
69. Zhuo, Y. *et al.* "β-Ga_2O_3 versus ε-Ga_2O_3 : Control of the crystal phase composition of gallium oxide thin film prepared by metal-organic chemical vapor deposition". *Appl. Surf. Sci.* **420**, 802–807 (2017).
70. Geller, S. "Crystal structure of β-Ga_2O_3". *J. Chem. Phys.* **33**, 676–684 (1960).
71. J. Kohn, G. K. and J. D. B. "Characterization of β-Ga_2O_3 and its Alumina isomorph, θ-Al_2O_3". *American Mineralogist* **42,** 398-407 (1956).
72. Yamaguchi, K. "First principles study on electronic structure of β-Ga_2O_3". *Solid State Commun.* **131**, 739–744 (2004).
73. Peelaers, H. & Van de Walle, C. G. "Brillouin zone and band structure of β-Ga_2O_3". *Phys. Status Solidi Basic Res.* **252**, 828–832 (2015).
74. Janowitz, C. *et al.* "Experimental electronic structure of In_2O_3 and Ga_2O_3". *New J. Phys.* **13**, (2011).
75. Handwerg, M., Mitdank, R., Galazka, Z. & Fischer, S. F. "Temperature-dependent thermal conductivity and diffusivity of a Mg-doped insulating β-Ga_2O_3 single crystal

along [100], [010] and [001]". *Semicond. Sci. Technol.* **31**, (2016).

76. Schubert, M. *et al.* "Anisotropy, phonon modes, and free charge carrier parameters in monoclinic β-gallium oxide single crystals". *Phys. Rev. B* **93**, 1–18 (2016).
77. Ma, Y. M. *et al.* "High-pressure and high-temperature behaviour of gallium oxide". *Chinese Phys. Lett.* **25**, 1603–1605 (2008).
78. Galazka, Z. *et al.* "On the bulk β-Ga_2O_3 single crystals grown by the Czochralski method". *J. Cryst. Growth* **404**, 184–191 (2014).
79. Víllora, E. G. *et al.* "Cathodoluminescence of undoped β-Ga_2O_3 single crystals". *Solid State Commun.* **120**, 455–458 (2001).
80. Binet, L. & Gourier, D. "Origin of the blue luminescence of β-Ga_2O_3". *J. Phys. Chem. Solids* **59**, 1241–1249 (1998).
81. Onuma, T. *et al.* "Modeling and interpretation of UV and blue luminescence intensity in β-Ga_2O_3 by silicon and nitrogen doping". *J. Appl. Phys.* **124**, (2018).
82. Harwig, T., Kellendonk, F. & Slappendel, S. "The ultraviolet luminescence of β-galliumsesquioxide". *J. Phys. Chem. Solids* **39**, 675–680 (1978).
83. Harwig, T. & Kellendonk, F. "Some observations on the photoluminescence of doped β-galliumsesquioxide". *J. Solid State Chem.* **24**, 255–263 (1978).
84. Onuma, T. *et al.* "Polarized Raman spectra in β-Ga_2O_3 single crystals". *J. Cryst. Growth* **401**, 330–333 (2014).
85. Higashiwaki, M., Sasaki, K., Kuramata, A., Masui, T. & Yamakoshi, S. "Gallium oxide (Ga_2O_3) metal-semiconductor field-effect transistors on single-crystal β-Ga_2O_3 (010) substrates". *Appl. Phys. Lett.* **100**, 1–4 (2012).
86. Sasaki, K. *et al.* "Device-quality β-Ga_2O_3 epitaxial films fabricated by ozone molecular beam epitaxy". *Appl. Phys. Express* **5**, 16–19 (2012).
87. Jessen, G. *et al.* "Toward realization of Ga_2O_3 for power electronics applications". *Device Res. Conf. - Conf. Dig. DRC* **25**, 2016–2017 (2017).
88. Herman, M. A., Richter, W., Sitter, H. *Epitaxy - Physical Principles and Technical Implementation - Springer Series in Materials Science* (2001).
89. Frey, H. & Khan, H. R. *Handbook of Thin-Film Technology*. *Springer Series* (2015).
90. Pierson, H. O. *HANDBOOK OF CHEMICAL VAPOR DEPOSITION (CVD)- Principles, Technology and Applications. Library of Congress Cataloging-in-Publication Data*. (1999).
91. Carlsson, J. O. & Martin, P. M. *Chemical Vapor Deposition*. *Handbook of Deposition Technologies for Films and Coatings* (Elsevier Ltd., 2010).

92. Baldini, M., Albrecht, M., Fiedler, A., Irmscher, K. & Fiedler, A. "Semiconducting Sn-doped β-Ga_2O_3 homoepitaxial layers grown by metal organic vapour-phase epitaxy" *J. Mater Sci.* **51**, 3650–3656 (2016).
93. Long, L. H. & Sackman, J. F. "The heat of formation and physical properties of gallium trimethyl". *Trans. Faraday Soc.* **54**, 1797–1803 (1958).
94. Yang, C. T. & Wang, L. K. *Handbook of Environmental Engineering 14 Advances in Water Resources Management*. (2015). doi:10.1007/978-3-319-22924-9
95. Umicore. TMGa. *https://pmc.umicore.com/storage/pmc/14-35-051-tdb-tmga-203x290mm.pdf*
96. Lee, P. W., Omstead, T. R., McKenna, D. R. & Jensen, K. F. "In situ mass spectroscopy and thermogravimetric studies of GaAs MOCVD gas phase and surface reactions". *J. Cryst. Growth* **85**, 165–174 (1987).
97. Li, S. H., Larsen, C. A. & Stringfellow, G. B. "Decomposition mechanisms of trimethylarsine". *J. Cryst. Growth* **102**, 117–125 (1990).
98. Jacko, M. G. & Price, S. J. W. "The Pyrolysis of TrimethylGallium". *Can. J. Chem.* **41**, 1560–1567 (1963).
99. Newman, C. G., O'neal, H. E., Ring, M. A., Leska, F. & Shipley, N. "Kinetics and mechanism of the silane decomposition". *Int. J. Chem. Kinet.* **11**, 1167–1182 (1979).
100. Fornari, R. *et al.* "Thermal stability of ε-Ga_2O_3 polymorph". *Acta Mater.* **140**, 411–416 (2017).
101. Yamaga, M., Víllora, E., Shimamura, K., Ichinose, N. & Honda, M. "Donor structure and electric transport mechanism in β-Ga_2O_3". *Phys. Rev. B - Condens. Matter Mater. Phys.* **68**, 1–9 (2003).
102. Ueda, N., Hosono, H., Waseda, R. & Kawazoe, H. "Synthesis and control of conductivity of ultraviolet transmitting β-Ga_2O_3 single crystals". *Appl. Phys. Lett.* **70**, 3561–3563 (1997).
103. Lany, S. "Defect phase diagram for doping of Ga_2O_3". *APL Mater.* **6**, (2018).
104. Son, N. T. *et al.* "Electronic properties of the residual donor in unintentionally doped β-Ga_2O_3". *J. Appl. Phys.* **120**, (2016).
105. Baldini, M. *et al.* "Si- and Sn-doped homoepitaxial β-Ga_2O_3 layers grown by MOVPE on (010)-oriented substrates". *ECS J. Solid State Sci. Technol.* **6**, Q3040–Q3044 (2017).
106. Suzuki, N. *et al.* "Fabrication and characterization of transparent conductive Sn-doped β-Ga_2O_3 single crystal". *Phys. Status Solidi Curr. Top. Solid State Phys.* **4**, 2310–2313

(2007).

107. Sasaki, K., Higashiwaki, M., Kuramata, A., Masui, T. & Yamakoshi, S. "Si-Ion implantation doping in β-Ga_2O_3 and its application to fabrication of low-resistance ohmic contacts". *Appl. Phys. Express* **6**, 2–6 (2013).

108. Chikoidze, E. *et al.* "Electrical, optical, and magnetic properties of Sn doped α-Ga_2O_3 thin films". *J. Appl. Phys.* **120**, (2016).

109. Varley, J. B., Janotti, A., Franchini, C. & Van De Walle, C. G. "Role of self-trapping in luminescence and p-type conductivity of wide-band-gap oxides". *Phys. Rev. B - Condens. Matter Mater. Phys.* **85**, 2–5 (2012).

110. Xiao, W. Z., Wang, L. L., Xu, L., Wan, Q. & Pan, A. L. "Electronic structure and magnetic properties in Nitrogen-doped β-Ga_2O_3 from density functional calculations". *Solid State Commun.* **150**, 852–856 (2010).

111. Dong, L., Jia, R., Li, C., Xin, B. & Zhang, Y. "Ab initio study of N-doped β-Ga_2O_3 with intrinsic defects: the structural, electronic and optical properties". *J. Alloys Compd.* **712**, 379–385 (2017).

112. Kyrtsos, A., Matsubara, M. & Bellotti, E. "On the feasibility of p-type Ga_2O_3". *Appl. Phys. Lett.* **112**, (2018).

113. Liu, L. L. *et al.* "Fabrication and characteristics of N-doped β-Ga_2O_3 nanowires". *Appl. Phys. A Mater. Sci. Process.* **98**, 831–835 (2010).

114. Chikoidze, E. *et al.* "P-type β-gallium oxide: A new perspective for power and optoelectronic devices". *Mater. Today Phys.* **3**, 118–126 (2017).

115. Zhang, L. Y., Yan, J. L., Zhang, Y. J., Li, T. & Ding, X. W. "First-principles study on electronic structure and optical properties of N-doped P-type β-Ga_2O_3". *Sci. China Physics, Mech. Astron.* **55**, 19–24 (2012).

116. Lyons, J. L. "Electronic Properties of Ga_2O_3 Polymorphs". *ECS J. Solid State Sci. Technol.* **8**, Q3226–Q3228 (2019).

117. Greco, G., Iucolano, F. & Roccaforte, F. "Ohmic contacts to Gallium Nitride materials". *Appl. Surf. Sci.* **383**, 324–345 (2016).

118. Zywietz, T. K., Neugebauer, J. & Scheffler, M. "The adsorption of oxygen at GaN surfaces". *Appl. Phys. Lett.* **74**, 1695–1697 (1999).

119. Oh, S. *et al.* "Development of solar-blind photodetectors based on Si-implanted β-Ga_2O_3". *Opt. Express* **23**, 28300 (2015).

120. Zhou, H. *et al.* "High-Performance Depletion/Enhancement-ode \β-Ga_2O_3 on Insulator (GOOI) Field-Effect Transistors with Record Drain Currents of 600/450 mA/mm".

IEEE Electron Device Lett. **38**, 103–106 (2017).

121. Zeng, K. *et al.* "Ga_2O_3 MOSFETs using spin-on-glass source/drain doping technology". *IEEE Electron Device Lett.* **38**, 513–516 (2017).

122. Wong, M. H., Nakata, Y., Kuramata, A., Yamakoshi, S. & Higashiwaki, M. "Enhancement-mode Ga_2O_3 MOSFETs with Si-ion-implanted source and drain". *Appl. Phys. Express* **10**, 3–6 (2017).

123. Si, M., Yang, L., Zhou, H. & Ye, P. D. "β-Ga_2O_3 nanomembrane negative capacitance field-effect transistors with steep subthreshold slope for wide band gap logic applications". *ACS Omega* **2**, 7136–7140 (2017).

124. Guo, D. Y. *et al.* "Oxygen vacancy tuned Ohmic-Schottky conversion for enhanced performance in β-Ga_2O_3 solar-blind ultraviolet photodetectors". *Appl. Phys. Lett.* **105**, (2014).

125. van der Pauw, L. J. "A method of measuring specific resistivity and Hall effect of discs of arbitrary shapes". *Philips Research Report* **13**, 1–9 (1958).

126. Ramadan, A. A., Gould, R. D. & Ashour, A. "On the Van der Pauw method of resistivity measurements". *Thin Solid Films* **239**, 272–275 (1994).

127. van der Pauw, L. J. "A method of measuring the resistivity and Hall coefficient of lamellae of arbitrary shape". *Philips Tech. Rev.* 220–224 (1958).

128. Chandra, A., Wood, C. E. C., Woodard, D. W. & Eastman, L. F. "Surface and interface depletion corrections to free carrier-density determinations by hall measurements". *Solid State Electron.* **22**, 645–650 (1979).

129. Chwang, R. *et al.* "Contact size effects on the van der Pauw method for resistivity and hall coefficient measurement". *Solid-State Elect.* **17**, 12 1217-1227 (1974).

130. Shklovskii, B. & Efros, A. "*Electronic properties of doped semiconductors". Solid state science (Springer Verlag)* **45**, (1984).

131. Parisini, A., Parisini, A. & Nipoti, R. "Size effect on high temperature variable range hopping in Al+ implanted 4H-SiC". *J. Phys. Condens. Matter* **29**, (2017).

132. Parisini, A. *et al.* "Si and Sn doping of ε-Ga_2O_3 layers". *APL Mater.* **7**, (2019).

133. von Bardeleben, H. J., Cantin, J. L., Parisini, A., Bosio, A. & Fornari, R. Conduction mechanism and shallow donor properties in silicon-doped ε-Ga_2O_3 thin films: A paramagnetic resonance study". *Phys. Rev. Mater.* **3**, 084601 (2019).

134. Lamperti, A. *et al.* "Thermal stability of high-κ oxides on SiO_2/Si or Si_xN_y/SiO_2/Si for charge-trapping nonvolatile memories". *Surf. Interface Anal.* **45**, 390–393 (2013).

135. Savchenko, D. V., Kalabukhova, E. N., Pöppl, A., Mokhov, E. N. & Shanina, B. D.

"EPR study of conduction electrons in heavily doped n-type 4H SiC". *Phys. Status Solidi Basic Res.* **248**, 2950–2956 (2011).

136. Altermatt, P. P., Schenk, A. & Heiser, G. "A simulation model for the density of states and for incomplete ionization in crystalline silicon. I. Establishing the model in Si:P". *J. Appl. Phys.* **100**, (2006).

137. K. A. Chao, R. R. "Concentration-fluctuation model of a doped semiconductor in the nonmetallic regime: Pseudocluster investigation". *J. Chem. Inf. Model.* **53**, 1689–1699 (2019).

138. D. K. Schroder. *Material and device - Semiconductor material and device. Third Edition*. *Physics Today* **44**, (2006).

139. Reeves, G. B. "Obtaining the specific contact resistance from Transmission Line Model measurements". *IEEE ELECTRON DEVICE Lett.* **3**, *5* 111–113 (1982).

140. Berger, H. H. "Models for contacts to planar devices". *Solid State Electron.* **15**, 145–158 (1972).

141. Janoch, R., Gabor, A. M., Anselmo, A. & Dube, C. E. "Contact resistance measurement - Observations on technique and test parameters". *2015 IEEE 42nd Photovolt. Spec. Conf. PVSC 2015* 1–6 (2015).

142. W. Shockley. "Research and investigation of inverse epitaxial UHF power transistors". *ep. No. AFAL-TDR-64-207, Air Force Avion. Lab., Wright-Patterson Air Force Base, OH* (1964).

143. Oishi, T., Koga, Y., Harada, K. & Kasu, M. "High-mobility β-Ga_2O_3 (201) single crystals grown by edge-defined film-fed growth method and their Schottky barrier diodes with Ni contact". *Appl. Phys. Express* **8**, 8–10 (2015).

144. Mohamed, M. *et al.* "Schottky barrier height of Au on the transparent semiconducting oxide β-Ga_2O_3". *Appl. Phys. Lett.* **101**, 26–31 (2012).

145. Neal, A. T. *et al.* "Incomplete ionization of a 110 MeV unintentional donor in β-Ga_2O_3 and its effect on power devices". *Sci. Rep.* **7**, 13218(2017).

146. Zhang, N. Q. "Effects of surface traps on breakdown voltage and switching speed of GaN power switching HEMTs". *IEDM. Tech. Dig.*, 25.5.1-25.5.4 (2001).

147. Korotchenkov, G., Pearton, S., Ren, F., Mastro, M. *Metal oxides series- Gallium oxide: Technology, Devices and Applications*. *Elsevier* (2018).

148. Rafique, S., Han, L. & Zhao, H. "Thermal annealing effect on β-Ga_2O_3 thin film solar blind photodetector heteroepitaxially grown on sapphire substrate". *Phys. Status Solidi A*, **214,** 1700063, (2017).

149. Onuma, T. *et al.* "Correlation between blue luminescence intensity and resistivity in β-Ga_2O_3 single crystals". *Appl. Phys. Lett.* **103**, 3–6 (2013).

150. Shimamura, K., Víllora, E. G., Ujiie, T. & Aoki, K. "Excitation and photoluminescence of pure and Si-doped β-Ga_2O_3 single crystals". *Appl. Phys. Lett.* **92**, 27–30 (2008).

151. Ravadgar, P. *et al.* "Effects of crystallinity and point defects on optoelectronic applications of β-Ga_2O_3 epilayers". *Opt. Express* **21**, 24599–24610 (2013).

152. Lee, J. *et al.* "Optical Signature of the Electron Injection in Ga_2O_3". *ECS J. Solid State Sci. Technol.* **6**, Q3049–Q3051 (2017).

153. Farzana, E., Chaiken, M. F., Blue, T. E., Arehart, A. R. & Ringel, S. A. "Impact of deep level defects induced by high energy neutron radiation in β-Ga_2O_3". *APL Mater.* **7**, 022502 (2019).

154. Gao, H. *et al.* "Optical signatures of deep level defects in Ga_2O_3". *Appl. Phys. Lett.* **112**, 1–6 (2018).

155. Neal, A. T. *et al.* "Donors and deep acceptors in β-Ga_2O_3". *Appl. Phys. Lett.* **113**, 1–6 (2018).

156. Varley, J. B., Peelaers, H., Janotti, A. & Walle, C. G. Van De. "Hydrogenated cation vacancies in semiconducting oxides". *J. Phys. Cond. Matter* **23**, 334212 (2011).

157. Reshchikov, M. A. "Temperature dependence of defect-related photoluminescence in III-V and II-VI semiconductors". *J. Appl. Phys.* **115**, (2014).

158. Rebien, M., Henrion, W., Hong, M., Mannaerts, J. P. & Fleischer, M. "Optical properties of gallium oxide thin films". *Appl. Phys. Lett.* **81**, 250–252 (2002).

Acknowledgements

The work reported in this thesis has been carried out also with the collaboration of many people who supported and helped me during this doctoral period and that I would like to thank. First of all, I would like to deeply thank my supervisor Prof. Roberto Fornari, and Prof. Antonella Parisini who constantly support me, guiding and enlightening me during this PhD period. With their experience and widespread knowledge of semiconductor physics they introduced me to this exciting research field. A special thanks to Dr. Matteo Bosi, for leading me into the world of MOCVD. I would like to express my deepest gratitude to all members of my research group for the fundamental teaching and always constructive discussions: Prof. Alessio Bosio, Prof. Maura Pavesi, Prof. Andrea Baraldi, Sig. Salvatore Vantaggio who shared with me their deep expertise and knowledge about the sputtering processes, contact depositions, electrical and optical characterizations. Thanks also to many kind people who helped me at IMEM-CNR institute: Dr. Enos Gombia, for his patience and kindness in showing me the basis of metal contact deposition through thermal evaporation technique, Dr. Claudio Ferrari for XRD measurement support and to Dr. Davide Calestani for his help with wet etching procedures. Many thanks to Dr. Francesco Mezzadri, who shared with me his wide knowledge of XRD and for introducing me into the crystallography field, making me more interested in these topics. A deep thank goes to Prof. Juan Jimenez and Alfredo Torres, who kindly hosted me in Valladolid, and taught me the basics about cathodoluminescence and deep levels investigations and who have always been available for questions and discussions. Many thanks to Dr. Ildikó Cora, Dr. Bela Pécz and Dr. Zsolt Zolnai from MFA Institute in Budapest, for performing TEM and RBS analysis on our films. Thanks to Dr. Detlef Klimm, from IKZ Institute in Berlin, for providing the useful results of DSC analysis, necessary to fully understand the thermal stability of ε-Ga_2O_3. Thanks to Dr. Alessio Lamperti, from IMM-CNR institute in Agrate Brianza, for ToF-SIMS analysis on our ε-phase films, which proved the effective Si- and Sn- impurity incorporation. Many thanks also to Dr. Jurgen von Bardeleben and his group, for EPR investigations, fundamental to better understand the transport mechanism and the doping of our samples. I would finally like to thank all the professors and employees of the Physics department of Parma University, with which I collaborated in different occasions, and especially Prof. Stefano Carretta and Prof. Cristiano Viappiani, coordinators of the PhD board, for their availability.

Last but not least, I would like to thank all my friends, colleagues and relatives, who differently accompanied me during these three years.